A study on modelling and simulation on reacting flow included in thermochemical conversion process of coal

李, 成義

https://doi.org/10.15017/1544005

A study on modelling and simulation on reacting flow included in thermochemical conversion process of coal

A thesis submitted to the Interdisciplinary Graduate School of Engineering Sciences in fulfillment of the requirements for the degree of Doctor of Philosophy

by

Cheng-Yi LI

Department of Applied Science for Electronics and Materials

Interdisciplinary Graduate School of Engineering Sciences

Kyushu University, Japan

August, 2015

CONTENTS

ACKNOWLEDGEMENTS

This thesis would not be completed without the supports and contributions from many people who are gratefully acknowledged here.

I would like to express my sincere appreciation and thanks to my supervisor Prof. Koyo Norinaga. Without his intelligent guidance, diligent endeavor and great patience, it would be impossible to complete this work. What's more, thanks for his help and friendship, I enjoyed my learning time at Kyushu University. I learned a lot from him, not only on how to do the research works, but also on how to do in my life.

At the same time, I would like to thank the committee members, Professors Seong-Ho Yoon, Hiroaki Watanabe and Jun-ichiro Hayashi for their review, brilliant comments and suggestions of both the doctoral thesis and oral presentation of the doctoral defense.

Here, sincere thanks are given to Prof. Jun-ichiro Hayashi and Assistant Prof. Shinji Kudo, for their precious guidance, patient help, and kind care in both of my study and daily life. Also, I would like to thank every member of our excellent team (Hayashi/Norinaga laboratory). They give me so much useful help and happy memories in my experiments and daily life. In addition to this, I would also like to thank Prof. Hsiu-Po Kuo and Doc. An-Ni Huang (Chang Gung University, Taiwan) for their help and contributions during my long-term international internship.

I would like to acknowledge the Global COE program, Kyushu University, Japan. Also, I express many thanks to the China Scholarship Council (CSC scholarship program) for financial supports during my doctoral study at Kyushu University.

Finally and most of all, I express my deep indebtedness to all my family particularly my parents (Xianyou Li and Fenghua Wang), my elder sister (Chengxiang Li) and brother-in-law (Kai Tian), my fiancée (Ruize Wang), and the people that I loved and beloved for the constant encouragement, help and sacrifice which permitted me to complete this study. There is no way I can thank them enough, but I hope I can do better in the future.

Chikushi Campus

2015. 08. 18

Chapter 1

General introduction

1.1 Background

Energy is essential to economic development, social wellbeing, national security and also improved quality of life in all countries [1–3]. Fossil fuels–such as petroleum, coal and natural gas which contain high percentages of carbon and are called as non-renewable resources–play an important role of world energy consumption at present and in the near future, although renewable energy resources have been attracted more attentions in recent years [4]. Coal continues to be an important energy source in many parts of the world, especially in China and India [5]. It becomes more and more important for clean utilization of coal with high efficiency.

Gasification is an old but continuously evolving technology. It can be described as the "conversion of any carbon-based feedstock into a gaseous product with a useful chemical heating value". Gasification is particularly suitable for the utilization of low-rank fuels, such as brown coal, due to the high gasification reactivity of these coals.

1.2 Coal Gasification

Gasification is a thermochemical way or process to convert carbonaceous solid fuel, such as coal and biomass, into gases, including H_2, CO, and CH_4, for power generation or chemical production.

1.2.1 Overview of Thermochemical Reactions of Gasification

Coal conversion in a gasifier are typically considered by using two processes: coal pyrolysis and char gasification, as shown in **Fig. 1.1**. When a coal particle is heated up, the initial thermochemical reactions of coal occur in the coal intra-particle, which are in general summarized as primary pyrolysis. And it results in the formation of volatile matter and char. The volatile matter released from primary pyrolysis is sometimes also called primary volatiles consisting of light gases (such as H_2, CO, CO_2, H_2O, CH_4 and other low hydrocarbons) and heavier products termed tar (also called primary tar). The tar is usually defined as the products heavier than C_6 compounds, such as benzene or otherwise as the products that can be condensed at ambient temperature [6]. The primary tar is a major component of primary volatiles. After that, the primary volatiles released from the particle further undergo thermal cracking in the extra-particle gas phase at elevated temperatures and/or elevated pressures, which is called the secondary pyrolysis. During the secondary pyrolysis, the primary volatiles can be converted into light gases and carbonaceous solid termed soot or coke. Similar secondary thermal cracking reactions also take place inside the solid char particles. Considering oxidizing agents in carrier gas, the char, soot and volatiles undergo reactions with oxidizing agents, which are termed as gasification of char and soot, and reforming of volatiles, respectively. In addition to those, volatiles and char particles interact continuously as the volatiles are reformed and char particles are gasified when considering the chemical interaction between volatiles and char (VCI) [7].

1.2.2 Low Temperature Gasification

Low temperature gasification process is the gasification of fossil fuels, such as lignite and biomass, occurred at temperatures well below 1000 °C. Low temperature gasification potentially realizes a loss of chemical energy smaller than 10%, compared with an IGCC [8], but also meets difficulty in fast and/or complete solid-to-gas conversion in conventional reactor systems, such as refractory tar problem and incomplete char gasification.

Refractory tarry compounds have been considered to be one of the key and hot issues in the gasification process, which not only inhibits the gasification process [9] but also at the same time causes serious problems in the operate downstream facilities. Lots of technologies and methods [10] have been proposed and employed for reducing or eliminating tar, such as liquid scrubbing and catalytic reforming. Current liquid scrubbing method can cool product gas to a target temperature to convert or condense tar from the gas phase to the liquid phase, but it causes an undesirable loss of overall thermal efficiency. For catalytic reforming method, lots of catalysts including natural (dolomite and olivine) and synthetic (nickel and alkali metals, etc.) have been extensively studied. However, it suffered severely from catalyst poisoning by Cl/S-containing species and deactivation by coking, attrition and/or sintering.

1.3 Models for Reactions in Coal Conversion

In the coal conversion process, lots of kinetic models were proposed and employed to explain the key thermochemical phenomena, such as coal pyrolysis, volatiles reforming, char gasification and volatiles-char interaction, as shown in **Fig. 1.2**.

1.3.1 Pyrolysis

Chemical kinetic modelling of coal pyrolysis has been studied and introduced, starting from a simple global model [11] to some complicated models incorporating the process of the recent understanding of coal structure. The models include single reaction model, parallel first order reactions of finite number model, distributed activation energy model and models based on new understanding of coal structure. Here some new coal pyrolysis models are introduced, which were proposed based on recent new understanding of coal structure.

a) FG-DVC Model

The FG-DVC model included two models: DVC model and FG model. The process of coal pyrolysis was demonstrated by Solomon and co-workers [12–14]. DVC model represents depolymerisation, vaporization and cross-linking (DVC) in the pyrolysis (a “tar formation model”). The DVC subroutine is employed to determine the yield of tar and the molecular weight distribution of the tar and char. The second one is Functional Group (FG) model that represents the decomposition of functional groups (a “species evolution/functional group model”). The FG subroutine is used to describe the gas evolution and the elemental and functional group compositions of the tar and char. This model is reported to represent pyrolysis behavior well under various conditions.

b) FASHCHAIN Model

The FASHCHAIN model was proposed by Niksa and co-workers [15–22] and assumed that

coal is modeled as a mixture of chain fragments ranging in size from a monomer to the nominally infinite chain. It means that coal consists of elemental units (monomers) containing aromatic nucleus. Chain fragments consists of identical aromatic nuclei interconnected pairwise by two different types of chemical linkages, with peripheral groups on some of the fragment ends. Aromatic nuclei, labile bridges, char links, and peripheral groups are main components of chemical fragments. Nuclei are interconnected by two types of linkages, labile bridges or char links. Neither linkage is a chemical bond. Labile bridges are groups of several aliphatic, alicyclic, and heteroatomic functionalities. Char links are much lighter, without any heteroatoms, and completely aromatic.

c) CPD Model

Chemical percolation devolatilization model (CPD model) was presented by Grant and co-workers [23–26]. In this model, coal is visualized as macromolecular arrays of fused aromatic rings of various sizes and types, including heteroaromatic systems with both nitrogen and oxygen atoms. The basic concept of this model is rather close to that of the FLASHCHAIN model, but this model is treating the change in cluster size sophisticatedly during pyrolysis and needs less number of parameters to calculate product yields.

1.3.2 Volatiles Reforming

Volatile matter released from coal includes light gases and tar. Light gases include H_2, CO, CO_2, H_2O, CH_4 and other low hydrocarbons. Tar consists of light tar and heavy tar. It is noted that volatiles reforming and/or cracking are assumed generally as the homogeneous (gas phase) reactions without the mechanisms of soot formation and carbon deposition.

A detailed chemical kinetic approach to develop a reaction mechanism consisting of hundreds or thousands of elementary-like reaction steps is a promising method for elucidating an accurate description of the phenomena that occurred in the gas phase. Numerical simulations with detailed chemical kinetic models have been performed to predict the chemistry and kinetics of combustion, as well as the pyrolysis of hydrocarbons [27–32]. However, gases released from coal or called coal-based gases (light gases and tar) consists of hundreds of components and thus its reaction mechanism has high complexity when combustion or reforming by oxidizing agent. In recent years, Norinaga and co-workers proposed and employed the detailed chemical kinetic model (DCKM) to understand the chemistry and kinetics, at the molecular level, of coal/biomass- based gases at different processes, such as secondary pyrolysis of coal/biomass [30,33,34] and reforming of coke oven gas [35–37].

1.3.3 Char Gasification

In the char gasification process, char reacts with gasifying agents to produce a combustible gas. It includes the gas-solid two-phase reactions. There are lots of models to describe and explain the reaction phenomena of noncatalytic gas solid reactions considering the structure of solid particles, such as general model, homogeneous model (also called volumetric model), grain model, pore model and shrinking core model. The rate of pyrolysis is so rapid that the gas-solid reaction of char is regarded as the rate-determining process. There are many kinetic models of reactions with the structure of solid particles to describe char gasification process.

a) Volumetric Model

The volumetric model (VM) or called homogeneous model is the simplest model, assuming that a uniform gas diffusion within the entire particle and, in consequence, simplifies that the char-gas reactions occur at active sites which are uniformly distributed throughout the whole particle. As the reaction progresses, the particle size remains constant while density decreases. The overall rate of gasification is independent of particle size.

b) Modified Volumetric Model

The modified volumetric model (MVM) was first introduced by Kasaoka et al. [38–40] as a modification of the volumetric model (VM). However, it assumes that the rate constant is changing with conversion of solid as the reaction proceeds. The equation (1.1) was applied to the isothermal gasification curve of fractional gasification f against time t (min) to evaluate the reactivity of char in steam gasification:

$$f = 1 - \exp(-at^b) \tag{1.1}$$

The parameters a and b in Equation (1.1) can be easily determined by applying the method of least squares to the linearized form of Equation (1.1), to give the specific rate of gasification k in units of g g^{-1} (daf) min^{-1} as follows:

$$k = (df/dt)/(1-f) = a^{(1/b)}b[-\ln(1-f)]^{(b-1)/b} \tag{1.2}$$

Equation (1.2) can be used to calculate the gasification rate df/dt or the specific rate k at any points on the $f-t$ curve.

c) Random Pore Model

A random pore model was proposed by Bhatia and Perlmutter [41,42] in fluid-solid reaction. During gasification process, the weight of sample changes with respect with time, and at the same time the pore structure also changes with time. As gasification proceeds, the pores become larger. Initially, the pore surface area becomes larger. With further gasification, pores merge and the walls dividing them disappear, which leads to a loss of surface area. The random pore model implied that surface reactivity is directly proportional to surface area, a common assumption of gas-solid reactions.

d) Shrinking Core Model

At very high reaction rates, the overall reaction rate is limited by the rate of mass transfer to and from the exterior of the char particle, not by the surface reaction rate or the rate of diffusion in the char pores. The shrinking core model, an alternative to the random pore model, is better to be employed for describing how the rate of reaction changes with extent of reaction.

In the shrinking core model, the porosity of particle is constant. The particle diameter decreases until the particle is gone, compared with the random pore model. For the shrinking core model, some assumptions are established when considering the dependence of reaction rate on extent of reaction. The particle is assumed spherical and the mass is proportional to the particle

volume and the reaction rate is proportional to the particle external surface area.

e) Langmuir-Hinshelwood Model

Langmuir-Hinshelwood (LH) kinetics [43] have modelled successfully the surface reaction rates, especially the effect of gas partial pressures on surface reaction rates. The LH model does not consider the effects of surface diffusion. For a more complete discussion of LH models, please see a textbook on heterogeneous catalytic processes.

1.3.4 Volatiles-char Interaction

When fresh fuel particles such as coal and biomass are continuously fed into the gasifier and therefore volatiles are continuously generated, the gasifying char particles will be surrounded by the volatiles. The volatiles are continuously being reformed with gasifying agents such as steam and O_2. The volatiles surrounding the particles also contain radials as intermediates of the reforming reactions. In other words, volatiles and char particles will interact continuously as the volatiles are reformed and char particles are gasified. Therefore, the volatiles-char interaction (VCI) is an important phenomenon in coal conversion process and has been reported in lots of literatures [7]. Unfortunately, almost all of reports are from laboratory scale experimental studies alone. Until now little literatures [44] are reported using kinetic model to understand some key phenomena in the presence of the volatiles-char interaction in coal conversion process.

1.4 CFD Approach for Simulating Coal Conversion Process

In recent years, computational fluid dynamics (CFD) has been used as a powerful tool to develop 2D or even three-dimensional (3D) models for gas-solid flow with or without reactions in coal conversion. CFD approach is a branch of fluid mechanics that uses numerical methods and algorithms to solve and analyze problems that involve fluid flows. One of the advantages is their capacity to analyze different working conditions and to estimate the field values inside the entire domain, including places where it is complicated to take measurements in experimental tests without affecting the working condition of the system. Therefore, theoretical modelling and experimental data can be combined to perform detailed studies of coal conversion process through computational fluid dynamics simulations, which enable the analysis of a considerable number of variables of the coal conversion process.

There are several methods to couple the chemistry with the turbulence (‘turbulence–chemistry interactions’) in the CFD modeling. Chen et al. [45–47] reported that a comprehensive 3D simulation model coupled with the multi solids process variables method was developed successfully for a 200 tons-per-day two-stage air blown entrained flow coal gasifier. The influence of turbulence on gas properties was taken into account by the pdf model with a clipped Gaussian distribution function.

The eddy dissipation/finite rate (ED/FR) model and the eddy dissipation concept (EDC) also are considered in the turbulence–chemistry interactions. Parente et al. [48] investigated and simulated a $CH_4/CH_4–H_2$ burner in a “moderate or intense low-oxygen dilution” (MILD) combustion regime using EDC. The EDC with detailed chemistry provided results showing a more uniform distribution of temperature as well as the extension of the reaction zone to a large

proportion of the available volume in the burner, as would be expected in a MILD combustion regime. Stefanidis et al. [49] also reported that EDC coupled with detailed reaction kinetics can successfully reproduce flow, temperature, and concentration fields in the radiation sections of industrial-scale steam-cracking units. However, no reported study has examined reforming characteristics of multi-component coal-based gases such as hot coke oven gas (HCOG) using EDC coupled with a detailed chemical kinetic model in CFD modelling.

In addition, computational fluid dynamics (CFD) has been employed as a powerful tool for obtaining a deeper understanding of the gas-solid mixed flows. Ropelato et al. [50] proposed an Eulerian-Eulerian approach for predicting fluid dynamics in the downer reactor with good agreement between experimental data and model predictions. However, no established CFD approach has been coupled with a kinetic model that accounts for the volatiles-char interaction on coal conversion process.

1.5 Objective of This Study

Coal is a major energy resource in the world. Gasification is an old yet still continuously evolving technology, and particularly suitable for the utilization of low-rank coals, such as Victorian brown coal, due to the high gasification reactivity of these coals. Chemical reactions in coal conversion are numerous and complex. Lots of kinetic models are published to describe the mechanism and history of chemical reactions in the processes of coal pyrolysis and char gasification. Some models of volatiles reforming have been proposed and there are still some limitations about them, for example, there are a few reforming models of tar-containing coal gas. It has proven that the volatiles-char interaction can affect every aspect of the gasification, for example, the decomposition of tar by intensified volatiles-char interaction. Unfortunately, almost all of reports are from laboratory scale experimental studies alone. The further development of the kinetic models of coal conversion still is an interesting but challenging task, especially coupled with computational simulation. Therefore, the objective of this study focuses on developing model approaches to understand the reforming of tar-containing gases for designing and scaling up future coal gasification technologies, especially future low temperature coal gasification technologies. In this work, the model approaches for different processes of coal gasification, such as the processes of coal conversion in the presence of volatiles-char interaction (**Chapter 2**) and tar-containing volatiles reforming (**Chapter 3 and Chapter 4**), are proposed and developed.

1.6 Outline of This Study

Five chapters, including the detailed works and a general summary, are included in the thesis (See **Fig. 1.3**) as follows:

Chapter 1 of this thesis are comprehensively reviewed the existing studies on the importance of low temperature gasification, and the published models of chemical kinetics in coal conversion, especially coupled with computational simulation. The chapter also includes the main objectives of the doctoral studies.

Chapter 2 describes coal conversion including reforming of nascent tar over the char surface in a drop tube reactor (DTR) in both experiments and numerical simulation. Victorian brown

coal and char was prepared form the same coal were co-fed into an atmospheric DTR. The effects of reaction temperature, solid hold-up, residence time, and steam partial pressure on the conversion characteristics were investigated. The lumping model approach was employed in this study in order to estimate kinetic parameters in coal conversion. The CFD approach coupled with lumped kinetic model was employed to develop a model of gas/solid flow and reaction in coal conversion by using an Eulerian-Eulerian approach. Finally, the CFD results for product distribution during coal conversion in the DTR were compared with the experimental data.

Chapter 3 describes the prediction of chemically reacting flow in conversion of coal gas using detailed chemistry and a one-dimensional flow model. Hot coke oven gas (HCOG), one of representative complex coal gas mixtures, was employed to investigate its reforming process. A detailed chemical kinetic model was used to predict the chemistries of hot coke oven gas reforming and was coupled with a plug model and one-dimensional flow with axial diffusion model. The gas temperature profiles were investigated by considering the energy balance equation accounting for the heat change induced by chemical reactions and heat losses to the surroundings. The approach also was evaluated critically by comparing the computed results with experimental data for exit major products, in addition to the total exit gas flow rate.

Chapter 4 describes a CFD approach coupled with reduced chemical kinetic model to simulate reacting flow of coal gas in bench scale reformer. The reforming of hot coke oven gas (HCOG), as one of complex coal gas mixtures, in turbulent flow was simulated numerically by considering both chemical reactions and fluid dynamics. A reduced detailed chemical kinetic model from the detailed chemical kinetic model was employed for realizing a kinetic model of finite rate reactions with k-ε turbulent model. The calculation was carried out using the eddy dissipation concept (EDC) coupled with the kinetic model, and accelerated using the in situ adaptive tabulation (ISAT) algorithm.

Chapter 5 summarizes the general conclusions of this work and some perspectives are proposed to improve these studies.

1.7 References

[1] Li C-Z. Special issue—Gasification: A route to clean energy. Process Saf Environ Prot 2006;84:407–8.

[2] Hayashi JI, Kudo S, Kim HS, Norinaga K, Matsuoka K, Hosokai S. Low-temperature gasification of biomass and lignite: Consideration of key thermochemical phenomena, rearrangement of reactions, and reactor configuration. Energy and Fuels 2014;28:4–21.

[3] IEA. World energy outlook 2014. Int Energy Agency 2014.

[4] Wikipedia. Fossil fuel. Http://en.wikipedia.org/wiki/fossil_fuel

[5] Zhang LX. Study on the decomposition characteristics of tar derived from low temperature gasification of brown coal over coexisting char by Kyushu Univeristy, 2013.

[6] Li C-Z. Advances in the science of Victorian brown coal. Elsevier; 2004.

[7] Li CZ. Importance of volatile-char interactions during the pyrolysis and gasification of low-rank fuels−A review. Fuel 2013;112:609–23.

[8] Tsutsumi A, Furutani H, Koda E, Fujimori T, Harada M, Akimoto A. Advanced IGCC/IGFC with exergy recovery technology. Proc. Energy Eng. Symp. Div Energ Eng 4, Soc. Chem. Eng. 2005;P.41–4.

[9] Bayarsaikhan B, Sonoyama N, Hosokai S, Shimada T, Hayashi JI, Li CZ, et al. Inhibition of steam gasification of char by volatiles in a fluidized bed under continuous feeding of a brown coal. Fuel 2006;85:340–9.

[10] Devi L, Ptasinski KJ, Janssen FJJG. A review of the primary measures for tar elimination in biomass gasification processes. Biomass and Bioenergy 2002;24:125–40.

[11] Maffei T, Frassoldati A, Cuoci A, Ranzi E, Faravelli T. Predictive one step kinetic model of coal pyrolysis for CFD applications. Proc Combust Inst 2013;34:2401–10.

[12] Solomon PR, Hamblen DG, Carangelo RM, Serio M A, Deshpande G V. General model of coal devolatilization. ACS Div. Fuel Chem. Prepr. 1987;32:83–98.

[13] Solomon PR, Fletcher TH, Pugmire RJ. Progress in coal pyrolysis. Fuel 1993;72:587–97.

[14] Solomon PR, Hamblen DG, Serio M A., Yu Z, Charpenay S. A characterization method and model for predicting coal conversion behaviour. Fuel 1993;72:469–88.

[15] Niksa S. FLASHCHAIN theory for rapid coal devolatilisation kinetics. 2. Impact of operation conditions. Energy & Fuels 1991;5:665–73.

[16] Niksa S. FLASHCHAIN theory for rapid coal devolatilisation kinetics. 3. Modeling the behavior of various coals. Energy & Fuels 1991;5:673–83.

[17] Niksa S. FLASHCHAIN theory for rapid coal devolatilization kinetics. 4. Predicting ultimate yields from ultimate analyses alone. Energy & Fuels 1994;8:659–70.

[18] Niksa S. FLASHCHAIN theory for rapid coal devolatilization kinetics. 5. Interpreting rates of devolatilization for various coal types and operating conditions. Energy & Fuels 1994;8:671–9.

[19] Niksa S, Hurt RH, Tominaga H, Ando T. Development of an evaluational prediction tool for coal combustion histories. Journal Japan Inst Energy 2003;82:849–55.

[20] Niksa S, Kerstein AR. Predicting the transient devolatilization of various coals with FLASHCHAIN. The 24th Int. Symp. Combust., Sydney (Australia): 1991,P.410–6.

[21] Niksa S, Kerstein AR. FLASHCHAIN theory for rapid coal devolatilization kinetics. 1. Formulation. Energy & Fuels 1991;5:647–65.

[22] Niksa S, Kerstein AR. Modeling devolatilization rates and yields from various coals with FLASHCHAIN. Symp. Ash Chem. Foss. Fuel Process., Chicago: 1993, P.1346–50.

[23] Genetti DB. An advanced model of coal devolatilization based on chemical structure. Brigham Young University, 1999.

[24] Fletcher TH, Kerstein AR, Pugmire RJ, Grant DM. A chemical percolation model for devolatilization: Temperature and heating rate effects. Amer Chem Soc, Div Fuel Chem 1989;34:1272–9.

[25] Fletcher TH, Kerstein AR, Pugmire RJ, Grant DM. Chemical percolation model for devolatilization. 2. Temperature and heating rate effects on product yields. Energy & Fuels 1990;4:54–60.

[26] Fletcher TH, Kerstein AR, Pugmire RJ, Solum MS, Grant DM. Chemical percolation model for devolatilization. 3. Direct use of 13C NMR data to predict effects of coal type. Energy & Fuels 1992;6:414–31.

[27] Ziegler I, Fournet R, Marquaire PM. Pyrolysis of propane for CVI of pyrocarbon: Part I. Experimental and modeling study of the formation of toluene and aliphatic species. J Anal Appl Pyrolysis 2005;73:212–30.

[28] Ziegler I, Fournet R, Marquaire PM. Pyrolysis of propane for CVI of pyrocarbon: Part II. Experimental and modeling study of polyaromatic species. J Anal Appl Pyrolysis 2005;73:231–47.

[29] Sheng CY, Dean AM. Importance of gas-phase kinetics within the anode channel of a solid-oxide fuel cell. J Phys Chem A 2004;108:3772–83.

[30] Norinaga K, Deutschmann O. Detailed kinetic modeling of gas-phase reactions in the chemical vapor deposition of carbon from light hydrocarbons. Ind Eng Chem Res 2007;46:3547–57.

[31] Dean A. Detailed kinetic modeling of autocatalysis in methane pyrolysis. J Phys Chem 1990;145:16–37.

[32] Descamps C, Vignoles GL, Féron O, Langlais F, Lavenac J. Correlation between homogeneous propane pyrolysis and pyrocarbon deposition. J Electrochem Soc 2001;148:C695.

[33] Norinaga K, Janardhanan VM, Deutschmann O. Detailed chemical kinetic modeling of pyrolysis of ethylene, acetylene, and propylene at 1073-1373 K with a plug-flow reactor model. Int J Chem Kinet 2008;40:199–208.

[34] Norinaga K, Shoji T, Kudo S, Hayashi JI. Detailed chemical kinetic modelling of vapour-phase cracking of multi-component molecular mixtures derived from the fast pyrolysis of cellulose. Fuel 2013;103:141–50.

[35] Appari S, Tanaka R, Li C, Kudo S, Hayashi J, Janardhanan VM, et al. Predicting the temperature and reactant concentration profiles of reacting flow in the partial oxidation of hot coke oven gas using detailed chemistry and a one-dimensional flow model. Chem Eng J 2015;266:82−90.

[36] Norinaga K, Yatabe H, Matsuoka M, Hayashi JI. Application of an existing detailed chemical kinetic model to a practical system of hot coke oven gas reforming by noncatalytic partial oxidation. Ind. Eng. Chem. Res. 2010;49:P.10565–71.

[37] Norinaga K, Hayashi J. Numerical simulation of the partial oxidation of hot coke oven gas with a detailed chemical kinetic model. Energy & Fuels 2010;24:165–72.

[38] Roberts DG, Harris DJ. A kinetic analysis of coal char gasification reactions at high pressures. Energy & Fuels 2006;20:2314–20.

[39] Kasaoka S, Sakata Y, Kayano S. Dvelopment of catalytic gasification process for coal char-catalytic effect and rate scheme of barium compounds. Chem Soc Japan 1982;8:51–8.

[40] Kasaoka S, Sakata Y, Shimada M. Effects of coal carbonization conditions on rate of steam gasification of char. Fuel 1987;66:697–701.

[41] Bhatia SK, Perlmutter DD. A random pore model for fluid-solid reactions: I. Isothermal, kinetic control. Aiche J 1980;26:379–86.

[42] Bhatia SK, Perlmutter DD. A random pore model for fluid-solid reactions: II. Diffusion and transport effect. Aiche J 1981;27:247–54.

[43] Kumar KV, Porkodi K, Rocha F. Langmuir-Hinshelwood kinetics−A theoretical study. Catal Commun 2008;9:82–4.

[44] Kajitani S, Tay HL, Zhang S, Li CZ. Mechanisms and kinetic modelling of steam gasification of brown coal in the presence of volatile-char interactions. Fuel 2013;103:7–13.

[45] Chen C, Horio M, Kojima T. Numerical simulation of entrained flow coal gasifiers. Part I: Modeling of coal gasification in an entrained flow gasifier. Chem Eng Sci 2000;55:3861–74.

[46] Chen C, Horio M, Kojima T. Use of numerical modeling in the design and scale-up of entrained flow coal gasifiers. Fuel 2001;80:1513–23.

[47] Chen C, Horio M, Kojima T. Numerical simulation of entrained flow coal gasifiers. Part II: Effects of operating conditions on gasifier performance. Chem Eng Sci 2000;55:3875–83.

[48] Parente A, Galletti C, Tognotti L. Effect of the combustion model and kinetic mechanism on the MILD combustion in an industrial burner fed with hydrogen enriched fuels. Int J Hydrogen Energy 2008;33:7553–64.

[49] Stefanidis GD, Merci B, Heynderickx GJ, Marin GB. CFD simulations of steam cracking furnaces using detailed combustion mechanisms. Comput Chem Eng 2006;30:635–49.

[50] Ropelato K, Meier HF, Cremasco M A. CFD study of gas-solid behavior in downer reactors: An Eulerian-Eulerian approach. Powder Technol 2005;154:179–84.

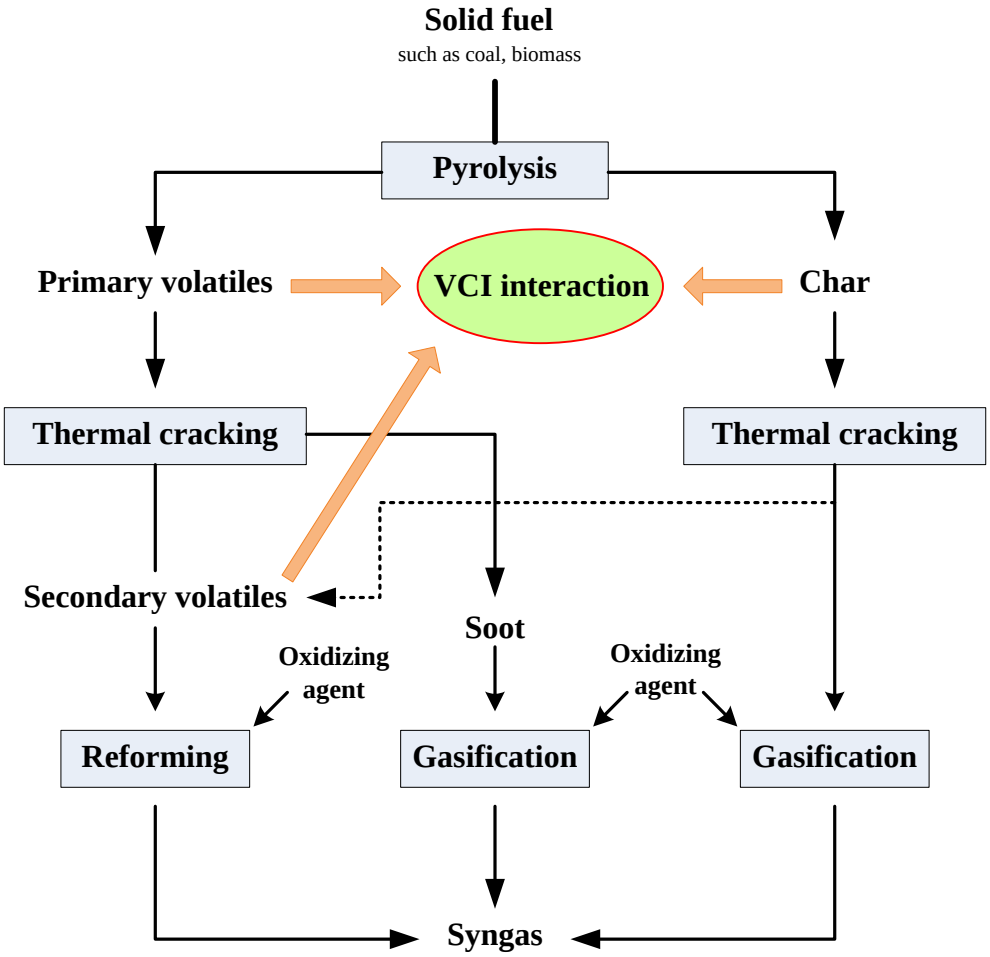

Fig. 1.1. Thermochemical reactions and intermediates involved in coal conversion.

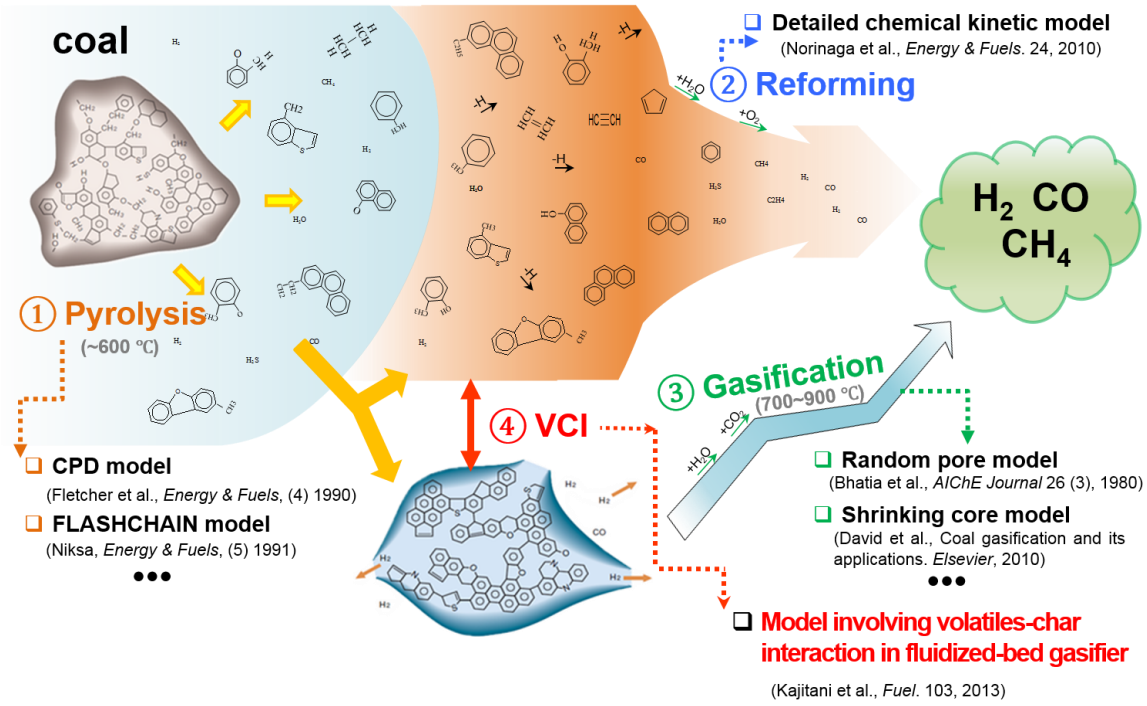

Fig. 1.2. Kinetic models for thermochemical reactions and intermediates involved in coal conversion.

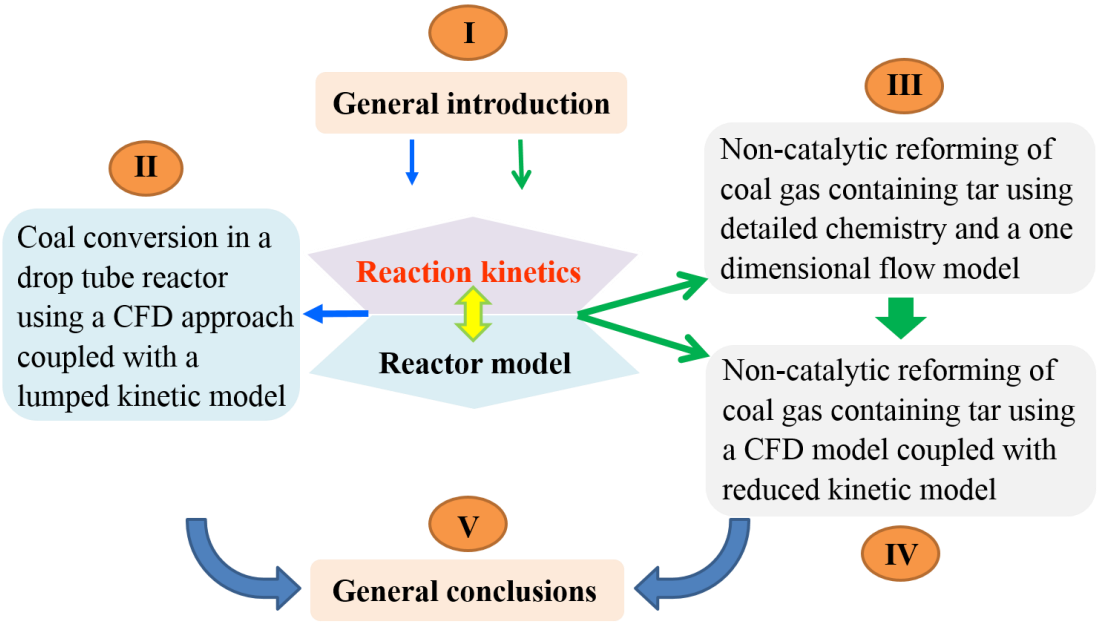

Fig. 1.3. Schematic diagram of the doctoral thesis structure.

Chapter 2

Coal conversion in a drop-tube reactor using a CFD approach coupled with a lumped kinetic model

2.1. Introduction

Gasification is an efficient and environmentally attractive process for coal utilization [1,2]. A major challenge in coal gasification is dealing with the refractory aromatic compounds that constitute the tar formed during gasification. This problem is especially severe in low temperature coal gasification processes, which are designed to have improved cold gas efficiency (CGE) [3]. Tar is an undesirable product of gasification because of various problems associated with condensation, formation of tar aerosols, and polymerization to form more complex structures, which can impede and damage the process equipment, as well as the engines and turbines used in product gas consumption [4]. Also, other volatile materials generated during coal gasification, such as light hydrocarbon gases and hydrogen may strongly inhibit char gasification [5–7]. Therefore, the development of technologies and methods for the reduction or removal of tar has received substantial attention in recent years [4,8,9]. Current liquid scrubbing techniques and catalytic reforming methods suffer from undesirable overall thermal efficiency loss and/or catalyst deactivation because of the deposition of chlorine/sulfur compounds and carbon [4,8,9]. Thus, it is necessary to develop a tar reforming system with high thermal efficiency and without catalyst poisoning or deactivation.

Recently, a triple-bed combined circulating fluidized-bed reactor system (TBCFB), consisting of a downer (pyrolyzer), a bubbling fluidized bed (BFB, gasifier), and a riser (combustor), was proposed [10–13]. This reactor system was designed to decompose tar through extensive interaction between the volatiles and char in the downer [10–13]. In this system, tar is decomposed inside the downer, which reduces the thermal efficiency loss associated with liquid scrubbing, and char is employed as a catalyst and/or promoter for tar decomposition. If the char is deactivated by interaction with the volatiles [1,14], it can be burned in the combustor to supply the heat required for the process.

In a recent study, we demonstrated the potential of the downer for decomposing tar in the TBCFB reactor system [15]. In that study, a drop-tube reactor (DTR) was used to investigate tar reforming over the char surface under reaction conditions similar to those expected for a downer reactor, wherein coal, char particles, and gas flow co-currently. It was demonstrated that nascent tar from rapid pyrolysis of Loy Yang (LY) brown coal was significantly decomposed by the volatiles-char interaction. However, that study concentrated on the laboratory-based experimental investigation without considering the establishment of a mathematic model based on the experimental results for coal conversion in the DTR.

Coal conversion incorporating the volatiles-char interaction proceeds *via* a number of complex parallel reactions, and produces a wide range of products, such as char, soot, light hydrocarbons, and both single and polycyclic aromatic hydrocarbons. An approach in which complex mixtures with large numbers of compounds are lumped into smaller groups of pseudo

components has been widely employed to provide a tractable number of kinetic equations and estimate kinetic parameters [16–18]. However, lumped component models have, to date, been mainly applied to hydrogenation or catalytic cracking of heavy oil and other residues [19–21].

Computational fluid dynamics (CFD) has been employed as a powerful tool for obtaining a deeper understanding of the gas-solid mixed flows employed in downer reactors [22–24]. Ropelato *et al.* [22] proposed an Eulerian-Eulerian approach for predicting fluid dynamics in the downer reactor with good agreement between experimental data and model predictions. The published works [10,22–24] include numerical simulation of gas-solid flow in downer reactor for coal conversion without considering chemical reactions. Some works [25,26] include numerical simulations of gas-solid flow combined with chemical reactions only in the riser-type fluid catalytic cracking (FCC) reactors. However, little reports are available on the CFD simulation for gas-solid flow combined with chemical kinetic model for coal conversion accounting the volatile-char interaction in the downer reactor.

Therefore, in this study, we have attempted to develop a CFD model coupled with a lumping kinetic model for coal conversion that accounts the volatiles-char interaction. The effects of residence time, reaction temperature, solid hold-up, and steam partial pressure on the conversion characteristics of coal in the DTR are investigated. The kinetic parameters are estimated under different operating conditions, and the mathematical model between the kinetic parameters and operating conditions is established based on the experimental results. A practical combined CFD and lumped kinetic model is likely to be an effective tool for facilitating to develop coal gasification in a TBCFB.

2.2. Experimental

2.2.1. Preparation of Coal and Char Samples

Dried Victorian Loy Yang brown coal (LY) with particle sizes ranging from 0.50 to 0.71 mm was used. Gasified LY Char (GLYC) sample was prepared by gasifying LY at 900 ℃ for 20 min in a steam/N_2 flow using a fluidized-bed reactor. The details of this preparation are reported elsewhere [15]. The elemental compositions of LY, and GLYC are listed in **Table 2.1**. All samples used in this study were prepared by blending the LY and GLYC at a fixed ratio (LY:GLYC = 3:7 on a carbon-mole basis).

2.2.2. Drop Tube Reactor Coal Conversion Experiments

In this study, a quartz tube of 2.550 m length with an isothermal zone of 2.100 m length and an inner diameter (i.d.) of 8 or 15 mm was heated by eight independently controlled electric furnaces. A nitrogen/steam gas mix preheated to 250 ℃ was supplied to the DTR, and the steam partial pressure was varied over the range of 0–0.05 MPa. The gas flow rate was carefully adjusted to maintain a constant gas residence time in the isothermal zone under the different experimental conditions. Detailed descriptions of the experimental setup and procedure are given elsewhere [15,27,28]. The experimental conditions used to investigate the effects of residence time, reaction temperature, steam partial pressure, and solid hold-up on the conversion characteristics of the coal samples in the DTR are provided in **Table 2.2**.

The variation of residence time was achieved by heating only a section of the quartz tube. In the cases of the quarter-length and half-length experiment, hereafter referred to as QL and HL, respectively, only the bottom two and four furnaces were heated to the desired temperature. All other experiments were carried out with the full length of the tube being heated, hereafter denoted as FL. In the FL case, the residence time of gas was about 4.6 s in the isothermal zone of drop-tube reactor, and that of coal particles was around 0.78 s. These values were estimated from the length of the isothermal zone and the terminal velocity of the particles [29]. Consequently, the residence times of the gas and particles were approximately halved in the HL experiments, although the length of the isothermal zone in the HL experiments was not exactly half that used in the FL experiments. The QL experiments were conducted in an analogous fashion.

The solid hold-up, defined as the ratio of total volume of solid particles to that of the isothermal zone of the DTR, was changed by varying the feeding rate and the internal diameter of the quartz tube. In the experiment where the solid was fed at 0.176 g/min, a quartz tube with an i.d. of 15 mm, instead of the 8 mm i.d. tube used in the other experiments, was employed. Feeding rates of 0.176, 0.5, and 1.5 g/min correspond to solid hold-up values of 8.31×10^{-6}, 8.31×10^{-5} and 2.50×10^{-4}, respectively. Thus, the solid hold-up is investigated at 1, 10, and 30 orders of magnitude in these experiments. The solid holdup can be one of the important factors influencing the effective heating rate of the particles and the effective residence time of the volatiles. The former can affect the primary pyrolysis characteristics, whereas the latter can affect the chemistry and kinetics of the subsequent secondary reactions. Therefore there are possibilities of further improvements in the modeling approach by taking other effects given by the solid holdup into account.

2.2.3. Pyrolysis in Two-stage Tubular Reactor

A rapid pyrolysis of LY at 650 ℃, high enough to complete pyrolysis in terms of tar evolution, was performed in a two-stage tubular reactor (TS-TR) to obtain information on the composition of primary pyrolysis products. Details of the TS-TR experiment are presented elsewhere [30,31]. The primary purpose of the TS-TR was to minimize the interaction between char and volatiles, thus preserving the properties of the nascent volatiles. These volatiles, such as CO, CO_2, and light C_1-C_4 hydrocarbons, were analyzed by a gas chromatograph, which was connected in series to the TS-TR. This carbon-containing gas mixture is hereon referred to as ‘carbon gases’. The char yield was obtained by weighing the residue recovered from the tube. The tar yield was determined by difference.

2.3. Kinetic Modeling

2.3.1. Lumping Concept

A number of complex reactions occur during *in situ* tar reforming over char in the DTR, and the products consist of a number of compounds resulting from concurrent pyrolysis, gas phase thermal cracking, steam reformation, and char gasification. The lumping model approach is widely employed traditionally to describe such complex mixtures by lumping large numbers of chemical compounds into smaller groups of pseudo-components in order to estimate kinetic parameters for the numerous and complex reactions, for example, the catalytic cracking of

petroleum fractions [25,26].

Previous studies [32,33] found that the evolution of tar, in terms of primary pyrolysis, is completed during heating before the coal particle temperature reaches at 600 °C, even at a heating rate of 1000 °C/s. Moreover, an important purpose of the DTR is to provide a very high heating rate to the sample. So, under our conditions, it is assumed that the coal sample has already been converted into tar, carbon gases, char, and soot by primary pyrolysis at the top of the DTR, where the temperature is 500–900 °C, before entering the isothermal zone, where the temperature is 900 °C. Therefore, in our model the feedstock is lumped into tar, carbon gases, char, and soot derived from the primary pyrolysis. Carbon oxides gases and hydrocarbon gases were lumped into one pseudo-compound as carbon gases for simplification of the kinetic model, although the carbon oxides gases and hydrocarbon gases have different roles in reactions. A reaction network among lumps in the DTR is proposed as shown in **Fig. 2.1**. The possible main reactions in the DTR were considered to be thermal cracking/steam reforming of volatiles, gasification, and the volatiles-char interaction.

The results obtained from the TS-TR experiment were used to estimate the initial amount of tar, carbon gases, char, and soot at the DTR inlet. It should be noted that there is a possibility that the product yields from TS-TR are different from the ones in DTR as the solid holdup (feeding rate) can affect heating rate of particles and the local volatile concentrations around particles, and thus induce some changes in primary pyrolysis characteristics. The amounts of these species were derived from the primary pyrolysis of LY combined with the amount of co-fed GLYC normalized on a carbon-mole basis. These normalized amounts of tar, carbon gases, char, and soot were defined as the initial amount of each lump fed into the isothermal zone of the DTR. The initial amounts of tar, carbon gases, and char were 7.4, 3.9, and 88.7 mol-C/100-mol-C-(LY+GLYC), respectively. The yield of the products will be indicated in the unit of mol-C per 100-mol-C of the sample (or mol-C/100-mol-C-(LY+GLYC)).

2.3.2. Reaction Network

A mathematic model for the proposed lumped model is established and expressed as;

$$\frac{dC_1}{dt} = -(k_{12} + k_{13} + k_{14})C_1 + k_{21}C_2 \tag{2.1}$$

$$\frac{dC_2}{dt} = -k_{12}C_2 + k_{12}C_1 + k_{32}C_3 + k_{42}C_4 \tag{2.2}$$

$$\frac{dC_3}{dt} = -k_{32}C_3 + k_{13}C_1 \tag{2.3}$$

$$\frac{dC_4}{dt} = -k_{42}C_4 + k_{14}C_1 \tag{2.4}$$

where C_i represents the concentration of each lump (i = 1–4); $k_{i,j}$ refers to the apparent rate constant for the reaction of lump i to lump j; and t is the residence time. The numerical solutions for these differential equations (2.1)–(2.4) were obtained using a fourth-order Runge–Kutta

method. The set of apparent rate constants $k_{i,j}$ in the proposed lump model was estimated so that the sum of squared residuals between the predicted values and the corresponding experimental values were minimized.

2.4. CFD Simulation

2.4.1. Mathematical Model

The presented CFD approach includes a kinetic model for chemical reactions included in coal conversion in the DTR of which parameters were all estimated empirically based on the experimental results by numerical fitting. The empirically justified kinetic model was then combined with the CFD model to visualize chemically reacting gas-solid flow in the laboratory scale DTR. This approach should have a potential to be extended to predict/estimate the gas-solid two-phase reacting flow of larger scale downer reactor simply by changing the boundary conditions since the theoretical basis developed in this work will be principally valid.

The multiphase Eulerian-Eulerian approach is widely used to predict the fluid dynamics in downers [22,34]. In this study, an Eulerian-Eulerian model was applied to simulate the fluid dynamics in the DTR. Eulerian-Eulerian model is a powerful model can all handle this type of problem correctly, even in the very low loading of the particles [35]. In this two-fluid model, the particles are treated as a continuum, similar to the gas phase. Thus, there are two interpenetrating phases, *i.e.* gas and solid, where each phase is characterized by its own conservation of motion equations. A summary of the governing equations and constitutive relationships is provided in **Table 2.3**.

For this gas-solid mixed flow in the DTR, a laminar model was employed for the gas phase. Under typical conditions, the Reynolds number $Re = DU_g\rho_g / \mu_g$, where D is the diameter of the DTR (8 mm), U_g is the superficial gas velocity (3 m/s), ρ_g and μ_g are the density and viscosity of the gas (0.22 kg/m^3 and 4.40×10^{-5} Pa·s at 900 °C, respectively), was about 124, meaning that the flow is laminar.

2.4.2. Simulation Layout

An axial illustration of the isothermal zone of the DTR is provided in **Fig. 2.2**. The LY and the char were fed into the isothermal zone with steam and N_2. The elemental composition of the char was determined by elemental analysis, and the average molecular mass of the carbon gases was calculated based on the results of the GC measurement. Soot was assumed to be pure carbon whereas element composition of solid char was assumed based on reported literatures [36–38]. In addition, molecular weight of tar was not easy to determine and, in this study, was also assumed from the literature [39]. The compositional formulae of the four lumps were found to be $C_{1.12}H_{1.83}O_{0.86}$ (carbon gases), $C_{38.57}H_{56.80}O_{17.52}$ (tar), $CH_{0.07}O_{0.04}$ (char), and C (soot).

The DTR is an axisymmetric cylinder. In order to save iteration time and improve convergence efficiency, a simplified geometry for the simulation was used, as illustrated in **Fig. 2.2**. There is a gas phase and a solid phase in our experiments. The gas phase is comprised of carbon gases, tar, steam, H_2 and N_2. The solid phase is comprised of char and soot. Six global chemical

reactions were considered in the simulation. Two homogeneous reactions (2.5–2.6) and four heterogeneous reactions (2.7–2.10) were considered according to the developed lumped kinetic model, as follows:

$$1\ [Tar] + 12.083\ [H_2O] \rightarrow 34.381\ [Carbon\text{-}gases] + 9.023\ [H_2] \quad (2.5)$$

$$1\ [Carbon\text{-}gases] + 0.262\ [H_2] \rightarrow 0.029\ [Tar] + 0.351\ [H_2O] \quad (2.6)$$

$$1\ [Tar] \rightarrow 38.575\ [Char] + 16.147\ [H_2O] + 10.856\ [H_2] \quad (2.7)$$

$$1\ [Tar] \rightarrow 38.575\ [Soot] + 17.519\ [H_2O] + 10.880\ [H_2] \quad (2.8)$$

$$1\ [Char] + 0.732\ [H_2O] \rightarrow 0.891\ [Carbon\text{-}gases] + 0.048\ [H_2] \quad (2.9)$$

$$1\ [Soot] + 0.732\ [H_2O] \rightarrow 0.891\ [Carbon\text{-}gases] + 0.048\ [H_2] \quad (2.10)$$

The boundary conditions for the numerical simulation are shown in **Table 2.4**. The Phase Coupled SIMPLE algorithm is used for pressure-velocity coupling. Convective fluxes in all transport equations were discretized with a first-order upwind and momentum with a first-order scheme. In addition, the convergence criteria are set in a transient fashion with a time step of 0.001 s and residuals for continuity less than 10^{-4}, energy less than 10^{-6}, and all species less than 10^{-6}. Typically, 350,000 iterations were required. The ANSYS FLUENT 14.0 (ANSYS Inc.; USA) was used for the CFD computations.

2.5. Results and Discussion

2.5.1. Effect of Residence Time

Fig. 2.3 shows the variation of product yields with residence time and their calculated results by the four-lump model. The residence times for the experimental values in the Fig. 2 were derived based on some conventional methods [40]. The methods to obtain them are described in **Table 2.5**. We found that the tar yield decreases sharply within very short residence time, while the yields of char, gases, and soot increase significantly. According to the predicted results, the sharp variation for each lump is completed at around 0.3 s, and then the variation levels off.

Initially, within a very short time, extensive tar deposition likely occurs over the char surface due to volatile-char interaction [1], which is induced by coexistence of high concentrations of tar and nascent char providing active sites for tar decomposition. It is believed that the decomposition takes place in micro- and nano- pores of char, depositing carbon onto the pore surfaces [1]. After 0.3 s, the decomposition rate of tar slows down presumably owing to the reduction of the amount of active sites that is induced by carbon deposition, though the chemical nature of the active sites is undefined yet. Char gasification becomes dominant in downstream and contributes further increase in the yield of carbon gases.

2.5.2. Effect of Temperature

The product distribution from coal conversion during *in situ* tar reforming in the DTR at different temperatures is shown in **Table 2.2** (runs 1–3). The tar, char, and soot yields decrease with increasing temperature, while the carbon gases yield increases. Similar results and

possible reasons were reported in our previous paper [15]. Higher temperature led to the higher gasification rate of char. the gasification of char formed micro-pores as active sites for coking over char, and so the high gasification rate of char was favorable for maintaining/enhancing the coking activity of char. Tar is decomposed by coking over char simultaneously when steam gasification of char occurred. So the tar, char and soot yields decrease with increasing temperature. In addition, the thermal cracking process was enhanced at higher temperatures. Those result in an increase of the yield of carbon gases.

In this work, we found that the reaction rate for *in situ* tar reforming in the DTR is strongly related to reaction temperature. The apparent rate constants of the four-lump model are estimated based on these experimental data and given in **Table 2.6**.

According to the Arrhenius equation, the apparent rate constant can be formulated as a function of the reaction temperature as below:

$$k = Ae^{-E_a/RT} \tag{2.11}$$

where A represents the pre-exponential factor of each reaction lump and E_a refers to the apparent activation energy. The pre-exponential factors (A) and the apparent activation energies (E_a) are shown in **Table 2.7**.

2.5.3. Effect of Solid Hold-up

The effects of the feeding rate on the yield of each lump were investigated (runs 6–8 in **Table 2.2**). The change in the solid hold-up greatly influences the product yields. The tar and soot yields are reduced whereas the char yield is significantly increased.

As shown in **Fig. 2.4**, the apparent rate constant of the reaction between tar and char (k_{13}) shows significant dependence on the solid hold-up, whereas other apparent rate constants do not. This indicates that high solid hold-up enhances the tar and char interaction. Decomposition of tar occurs on the active sites of pore surface of the char particles. The increase of the local concentration of char particles with increasing solid holdup provides more surface area and thus increases the amount of active sites, contributing extensive decomposition of tar. Based on our lumped kinetic model proposed in this study, the obvious effect of the solid holdup on the kinetics is appeared only at the conversion of tar into char (k_{13}) as shown in **Fig 2.4**. In addition, it should be noted that the intensive volatiles-char interaction also results in changes in char structure [41] and enhancement of volatilisation of inorganic matters [14] in char matrix.

2.5.4. Effect of Steam Partial Pressure

The effects of steam partial pressure on the yield of each product were investigated in runs 7, 9 and 3 as shown in **Table 2.2**. The results indicate that the steam partial pressure slightly affects the product yield under the conditions used. However, it is apparent that addition of steam suppresses soot formation, which is consistent with results reported previously [42]. A slight increase in gas yield may be attributed to the improvement of gasification under higher steam partial pressure. A considerable amount of H_2O (12 mol per 100-mol-C in the coal) is produced during the pyrolysis of coal [42,43]. Therefore, it is likely that this amount of H_2O is sufficient to supply the steam required in these reactions under current experimental conditions,

and the addition of extra steam has little influence on the *in situ* tar reforming process. As shown in **Fig. 2.5**, the apparent rate constants k_{14} (Tar→Soot) and k_{42} (Soot→Gas) vary with the steam partial pressure whereas the other apparent rate constants seem independent of it.

2.5.5. CFD with the Eulerian-Eulerian Approach Coupled with Lumped Kinetic Model

2.5.5.1. Mass Flow rate of Different Lumps in the DTR

A CFD analysis coupled with the developed lumped kinetic model (Reaction equations from (2.5) to (2.10)) was conducted. The apparent rate constants such as k_{12}, k_{21}, k_{13}, k_{14}, k_{32}, and k_{42} that were empirically determined through the comparison with the experimental results, were used for reactions (2.5), (2.6), (2.7), (2.8), (2.9), and (2.10), respectively. **Fig. 2.6** illustrates the total mass flow rate of the four lumps along the distance from the entrance of the DTR (in run 4 in **Table 2.2**). A QL drop tube reactor was employed in run 4. As can be seen in the figure, in the carbon conversion process, reforming and cracking of tar over the char surface occurred, and thus, the mass flow rate of tar decreases gradually from inlet to outlet, whereas char, as a promoter of decomposition of tar during the *in situ* tar reforming process [1], undergoes strong coking when tar being reformed and its mass flow rate increases. After tar concentration decreases along the DTR due to the decomposition of tar over char surface, the second stage, in where char gasification will be main chemical reactions, take place in the DTR with time such as in the bottom of the HL and FL drop-tube reactor. The mass fraction of carbon gases shows a rapid increase along the drop tube reactor. From the kinetic model, carbon gases is consumed only by pyrolysis to yield tar, but can be produced in many pathways such as tar cracking and gasification of char and soot.

The effect of reaction temperature, solid hold-up, and steam partial pressure on tar consumption along the drop tube reactor is shown in **Fig. 2.7**. In **Fig. 2.7b**, the value of tar decomposition is used as vertical axis instead of tar concentration along the drop tube reactor, because the feeding rates of different cases are different and it causes that the initial values of tar concentration at different cases are not the same when compared. As can be seen in the figure, most of the tar (about 85%) is consumed rapidly near the entrance zone of the DTR. The higher the reaction temperature is, the more rapidly the tar is consumed (**Fig. 2.7a**), and the higher the solid hold-up is, the stronger the volatiles-char interaction is (**Fig. 2.7b**). However, the steam partial pressure has little effect on tar consumption (**Fig. 2.7c**).

2.5.5.2. Comparisons between Simulation Results and Experiments

Fig. 2.8 shows a comparison of the CFD results and experimental data under various conditions, and confirms that there is good agreement between the two. This means that the proposed CFD model gives acceptable prediction of product yields for carbon conversion during the *in situ* tar reforming process, and that the developed model adequately represents the processes that constitute coal conversion in the DTR.

2.6. Conclusions

Loy Yang brown coal was converted in a DTR under conditions similar to those typically used in a downer reactor, where coal, char particles, and gas flow co-currently. The effects of residence time (0−4.6 s for gas; 0−0.78 s for solid particles), reaction temperature (700-900 ℃),

solid hold-up ($8.31\times10\text{-}^{6}$–2.50×10^{-4}), and steam partial pressure (0−0.05 MPa) on the conversion characteristics were studied. The temperature showed a significant influence on the rate of every process, and the product yields varied significantly with temperature. The solid hold-up mainly affected the tar-char interaction and tar was decomposed more extensively with increasing solid hold-up. The steam partial pressure only slightly affected the yields of tar, char, and carbon gases, but suppressed soot formation. A kinetic model with four lumps (gases, tar, char, and soot) and six reactions constituting volatiles-char interaction was developed and successfully integrated with a CFD approach to simulate gas/particle flow in the DTR.

2.7. References

[1] J.I. Hayashi, S. Kudo, H.S. Kim, K. Norinaga, K. Matsuoka, S. Hosokai, Low-temperature gasification of biomass and lignite: Consideration of key thermochemical phenomena, rearrangement of reactions, and reactor configuration, Energy and Fuels. 28 (2014) 4–21.

[2] C.-Z. Li, Special issue—Gasification: A route to clean energy, Process Saf. Environ. Prot. 84 (2006) 407–408.

[3] J.-I. Hayashi, S. Hosokai, N. Sonoyama, Gasification of low-rank solid fuels with thermochemical energy recuperation for hydrogen production and power generation, Process Saf. Environ. Prot. 84 (2006) 409–419.

[4] L. Devi, K.J. Ptasinski, F.J.J.G. Janssen, A review of the primary measures for tar elimination in biomass gasification processes, Biomass and Bioenergy. 24 (2002) 125–140.

[5] M.G. Lussier, Z. Zhang, D.J. Miller, Characterizing rate inhibition in steam/hydrogen gasification via analysis of adsorbed hydrogen, Carbon N. Y. 36 (1998) 1361–1369.

[6] B. Bayarsaikhan, N. Sonoyama, S. Hosokai, T. Shimada, J.I. Hayashi, C.Z. Li, et al., Inhibition of steam gasification of char by volatiles in a fluidized bed under continuous feeding of a brown coal, Fuel. 85 (2006) 340–349.

[7] C. Fushimi, T. Wada, A. Tsutsumi, Inhibition of steam gasification of biomass char by hydrogen and tar, Biomass and Bioenergy. 35 (2011) 179–185.

[8] P. Simell, E. Kurkela, P. Stahlberg, J. Hepola, Catalytic hot gas cleaning of gasification gas, Catal. Today. 27 (1997) 3–68.

[9] Z. Abu El-Rub, E.A. Bramer, G. Brem, Review of catalysts for tar elimination in biomass gasification processes, Ind. Eng. Chem. Res. 43 (2004) 6911–6919.

[10] G. Guan, C. Fushimi, M. Ishizuka, Y. Nakamura, A. Tsutsumi, S. Matsuda, et al., Flow behaviors in the downer of a large-scale triple-bed combined circulating fluidized bed system with high solids mass fluxes, Chem. Eng. Sci. 66 (2011) 4212–4220.

[11] G. Guan, C. Fushimi, A. Tsutsumi, Prediction of flow behavior of the riser in a novel high solids flux circulating fluidized bed for steam gasification of coal or biomass, Chem. Eng. J. 164 (2010) 221–229.

[12] G. Guan, C. Fushimi, A. Tsutsumi, M. Ishizuka, S. Matsuda, H. Hatano, et al., High-density circulating fluidized bed gasifier for advanced IGCC/IGFC—Advantages and challenges, Particuology. 8 (2010) 602–606.

[13] T. Matsuhara, S. Hosokai, K. Norinaga, K. Matsuoka, C.Z. Li, J.I. Hayashi, In-situ reforming of tar from the rapid pyrolysis of a brown coal over char, Energy and Fuels. 24 (2010) 76–83.

[14] C.Z. Li, Importance of volatile-char interactions during the pyrolysis and gasification of low-rank fuels−A review, Fuel. 112 (2013) 609–623.

[15] L.X. Zhang, T. Matsuhara, S. Kudo, J.I. Hayashi, K. Norinaga, Rapid pyrolysis of brown coal in a drop-tube reactor with co-feeding of char as a promoter of in situ tar reforming, Fuel. 112 (2013) 681–686.

[16] P. Balasubramanian, S. Pushpavanam, Model discrimination in hydrocracking of vacuum gas oil using discrete lumped kinetics, Fuel. 87 (2008) 1660–1672.

[17] N.C. Dave, G.J. Duffy, P. Udaja, A four-lump kinetic model for the cracking/coking of recycled heavy oil, Fuel. 72 (1993) 1331–1334.

[18] D. Leckel, Catalytic hydroprocessing of coal-derived gasification residues to fuel blending stocks: Effect of reaction variables and catalyst on hydrodeoxygenation (HDO), hydrodenitrogenation (HDN), and hydrodesulfurization (HDS), Energy and Fuels. 20 (2006) 1761–1766.

[19] J.F. Mosby, R.D. Buttke, J.A. Cox, C. Nikolaides, Process characterization of expanded-bed reactors in series, Chem. Eng. Sci. 41 (1986) 989–995.

[20] I. Elizalde, M.A. Rodr ́guez, J. Ancheyta, Application of continuous kinetic lumping modeling to moderate hydrocracking of heavy oil, Appl. Catal. A Gen. 365 (2009) 237–242.

[21] S. Authayanun, W. Pothong, D. Saebea, Y. Patcharavorachot, A. Arpornwichanop, Modeling of an industrial fixed bed reactor based on lumped kinetic models for hydrogenation of pyrolysis gasoline, J. Ind. Eng. Chem. 14 (2008) 771–778.

[22] K. Ropelato, H.F. Meier, M.A. Cremasco, CFD study of gas-solid behavior in downer reactors: An Eulerian-Eulerian approach, Powder Technol. 154 (2005) 179–184.

[23] Y.N. Kim, C. Wu, Y. Cheng, CFD simulation of hydrodynamics of gas-solid multiphase flow in downer reactors: Revisited, Chem. Eng. Sci. 66 (2011) 5357–5365.

[24] Z. Shu, G. Peng, J. Wang, N. Zhang, S. Li, W. Lin, Comparative CFD analysis of heterogeneous gas-solid flow in a countercurrent downer reactor, Ind. Eng. Chem. Res. 53 (2014) 3378–3384.

[25] K.N. Theologos, N.C. Markatos, Advanced modeling of fluid catalytic cracking riser-type reactors, AIChE J. 39 (1993) 1007–1017.

[26] X. Lan, C. Xu, G. Wang, L. Wu, J. Gao, CFD modeling of gas-solid flow and cracking reaction in two-stage riser FCC reactors, Chem. Eng. Sci. 64 (2009) 3847–3858.

[27] L.X. Zhang, S. Kudo, N. Tsubouchi, J.I. Hayashi, Y. Ohtsuka, K. Norinaga, Catalytic effects of Na and Ca from inexpensive materials on in-situ steam gasification of char from rapid pyrolysis of low rank coal in a drop-tube reactor, Fuel Process. Technol. 113 (2013) 1–7.

[28] O. Mašek, S. Hosokai, K. Norinaga, C.Z. Li, J.I. Hayashi, Rapid gasification of nascent char in steam atmosphere during the pyrolysis of Na- and Ca- ion-exchanged brown coals in a drop-tube reactor, Energy and Fuels. 23 (2009) 4496–4501.

[29] J.G. Lee, J.H. Kim, H.J. Lee, T.J. Park, S.D. Kim, Characteristics of entrained flow coal gasification in a drop tube reactor, Fuel. 75 (1996) 1035–1042.

[30] K. Norinaga, H. Yang, R. Tanaka, S. Appari, K. Iwanaga, Y. Takashima, et al., A mechanistic study on the reaction pathways leading to benzene and naphthalene in cellulose vapor phase cracking, Biomass and Bioenergy. 69 (2014) 144–154.

[31] K. Norinaga, T. Shoji, S. Kudo, J.I. Hayashi, Detailed chemical kinetic modelling of vapour-phase cracking of multi-component molecular mixtures derived from the fast pyrolysis of cellulose, Fuel. 103 (2013) 141–150.

[32] C. Sathe, Y. Pang, C.Z. Li, Effects of heating rate and ion-exchangeable cations on the pyrolysis yields from a Victorian brown coal, Energy and Fuels. 13 (1999) 748–755.

[33] K. Jamil, J. Hayashi, C.-Z. Li, Pyrolysis of a Victorian brown coal and gasification of nascent char in CO_2 atmosphere in a wire-mesh reactor, Fuel. 83 (2004) 833–843.

[34] S. Vaishali, S. Roy, P.L. Mills, Hydrodynamic simulation of gas-solids downflow reactors, Chem. Eng. Sci. 63 (2008) 5107–5119.

[35] ANSYS FLUENT theory guide, ANSYS, InC, 2011.

[36] H.J. Jeong, D.K. Seo, J. Hwang, CFD modeling for coal size effect on coal gasification in a two-stage commercial entrained-bed gasifier with an improved char gasification model, Appl. Energy. 123 (2014) 29–36.

[37] M. Vascellari, R. Arora, C. Hasse, Simulation of entrained flow gasification with advanced coal conversion submodels. Part 2: Char conversion, Fuel. 118 (2014) 369–384.

[38] S.-P. Shi, S.E. Zitney, M. Shahnam, M. Syamlal, W. A. Rogers, Modelling coal gasification with CFD and discrete phase method, J. Energy Inst. 79 (2006) 217–221.

[39] P.E. Unger, E.M. Suuberg, Molecular weight distributions of tars produced by flash pyrolysis of coals, Fuel. 63 (1984) 606–611.

[40] H. Masuda, Ko Higashitani, Hideto Yoshida, Powder technology: Fundamentals of particles, powder beds, and particle generation, CSC Press, Taylor & Francis Group, New York, 2007.

[41] S. Zhang, Z. Min, H.-L. Tay, M. Asadullah, C.-Z. Li, Effects of volatile–char interactions on the evolution of char structure during the gasification of Victorian brown coal in steam, Fuel. 90 (2011) 1529–1535.

[42] J.I. Hayashi, M. Iwatsuki, K. Morishita, A. Tsutsumi, C.Z. Li, T. Chiba, Roles of inherent metallic species in secondary reactions of tar and char during rapid pyrolysis of brown coals in a drop-tube reactor, Fuel. 81 (2002) 1977–1987.

[43] J.I. Hayashi, H. Takahashi, M. Iwatsuki, K. Essaki, A. Tsutsumi, T. Chiba, Rapid conversion of tar and char from pyrolysis of a brown coal by reactions with steam in a drop-tube reactor, Fuel. 79 (2000) 439–447.

Table Captions:

Figure Captions:

Table 2.1. Ultimate analysis of Loy Yang coal (LY) and gasified LY char (GLYC).

	Ultimate analysis (daf [a] wt.%)			
	C	H	N	O [b]
LY	67.42	4.83	0.58	27.16
GLYC	94.56	0.57	0.39	4.48

[a] dry ash-free.

[b] by difference.

Table 2.2. Experimental conditions and product yields on carbon mole basis.

Run No.	1	2	3	4	5	6	7	8	9
Temperature (°C)	700	800	900	900	900	900	900	900	900
Residence time	FL	FL	FL	QL	HL	FL	FL	FL	FL
Feeding rate (g/min)	0.5	0.5	0.5	0.5	0.5	0.176[a]	0.5	1.5	0.5
Steam partial pressure (MPa)	0.05	0.05	0.05	0.05	0.05	0	0	0	0.03
Product yield, mol-C/100-mol-C-(LY+GLYC)									
Tar/Lump 1	1.5	1.1	1.1	1.9	1.2	1.4	1.2	0.9	1.0
Gases/Lump 2	4.9	6.8	7.9	5.0	7.3	6.7	6.7	6.2	7.7
Char/Lump 3	92.3	90.6	90.1	91.8	90.3	88.9	89.7	91.3	90.0
Soot/Lump 4	1.3	1.5	1.0	1.3	1.1	3.1	2.5	1.7	1.3

[a] A quartz tube with internal diameter of 15 mm was used.

Table 2.3. Governing equations for gas-solid flow and constitutive law.

Continuity equations for gas and solid phases

$$\frac{\partial}{\partial t}(\varepsilon_g \rho_g) + \nabla \cdot (\varepsilon_g \rho_g \vec{u}_g) = 0$$

$$\frac{\partial}{\partial t}(\varepsilon_s \rho_s) + \nabla \cdot (\varepsilon_s \rho_s \vec{u}_s) = 0$$

Momentum equations for gas and solid phases

$$\frac{\partial}{\partial t}(\varepsilon_g \rho_g \vec{u}_g) + \nabla \cdot (\varepsilon_g \rho_g \vec{u}_g \otimes \vec{u}_g) = -\varepsilon_g \nabla p + \nabla \cdot (\varepsilon_g \bar{\bar{\tau}}_g) + \varepsilon_g \rho_g \vec{g} + \beta(\vec{u}_s - \vec{u}_g)$$

$$\frac{\partial}{\partial t}(\varepsilon_s \rho_s \vec{u}_s) + \nabla \cdot (\varepsilon_s \rho_s \vec{u}_s \otimes \vec{u}_s) = -\varepsilon_s \nabla p - \nabla p_s + \nabla \cdot (\varepsilon_s \bar{\bar{\tau}}_s) + \varepsilon_s \rho_s \vec{g} + \beta(\vec{u}_g - \vec{u}_s)$$

Exchange coefficient of gas and solid phase

$$\beta = \begin{cases} \frac{3}{4} C_D \frac{\rho_g \varepsilon_g \varepsilon_s \left|\vec{u}_s - \vec{u}_g\right|}{d_s} \varepsilon_g^{-2.65} & \varepsilon_g \geq 0.8 \\ 150 \frac{\varepsilon_s^2 \mu_g}{\varepsilon_g d_s^2} + 1.75 \frac{\rho_g \varepsilon_s \left|\vec{u}_s - \vec{u}_g\right|}{d_s} & \varepsilon_g \leq 0.8 \end{cases}$$

$$C_D = \begin{cases} \frac{24}{Re_s}\left[1 + 0.15(\varepsilon_g Re_s)^{0.687}\right] & Re_s \leq 1000 \\ 0.44 & Re_s \geq 1000 \end{cases}$$

Symbols used

d_p particle diameter, m

$\vec{g}$ gravitational acceleration, m/s^2

g_0 radial distribution function

$\vec{u}_g$, $\vec{u}_s$ gas and solid velocity vectors, m/s

u_{pq} interphase velocity

C_D effective drag coefficient for a particle

Re_s Reynolds number of particle

Greek symbols

β gas-solid exchange coefficient for a control volume, kg/(m^3 · s)

ε_g gas volume fraction

ε_s solid volume fraction

μ_g, μ_s fluid and solid viscosity, Pa·s

ρ_g, ρ_s fluid density and solid density, kg/m^3

$\bar{\bar{\tau}}_p$ the p^{th} phase stress-strain tensor

Table 2.4. Boundary conditions of the numerical simulation.

Case No.	1	2	3	4	5	6	7	8	9
Inner diameter of the DTR, mm	8	8	8	8	8	15	8	8	8
Char feed rate, kg/h	0.024	0.024	0.024	0.024	0.024	0.008	0.024	0.071	0.024
Total gas flow rate, kg/h	0.026	0.026	0.026	0.026	0.026	0.087	0.030	0.043	0.028
Wall temperature, K	973	1073	1173	1173	1173	1173	1173	1173	1173
Solid inlet temperature, K	973	1073	1173	1173	1173	1173	1173	1173	1173
Gas inlet temperature, K	973	1073	1173	1173	1173	1173	1173	1173	1173
Species, wt%									
Carbon-gases	8.21	8.21	8.21	8.21	8.21	0.87	7.05	14.90	7.70
Tar	12.74	12.74	12.74	12.74	12.74	1.35	10.94	23.13	11.95
Hydrogen	0	0	0	0	0	0	0	0	0
Steam	33.04	33.04	33.04	33.04	33.04	0.37	2.97	6.27	19.90
Nitrogen	46.02	46.02	46.02	46.02	46.02	97.42	79.04	55.70	60.45

Table 2.5. The calculation of residence times of the gas and solid.

Run No.	Residence time of gas			Residence time of solid					
	L_{iso} (m)	u_g (m/s)	t_{gas} (s)	Re_s	ρ_g (kg/m^3)	μ_g (Pa*s)	Resistance coefficient (ζ)	Terminal velocity (u_t) (m/s)	t_{solid} (s)
1	2.100	0.378	5.55	13.6	0.28	3.813E-05	3.86	3.05	0.77
2	2.100	0.417	5.03	11.4	0.26	4.115E-05	4.29	3.03	0.79
3	2.100	0.457	4.60	9.5	0.22	4.405E-05	4.80	3.04	0.78
4	0.340	0.457	0.75	9.5	0.22	4.405E-05	4.80	3.04	0.13
5	0.927	0.457	2.03	9.5	0.22	4.405E-05	4.80	3.04	0.34
6	2.100	0.457	4.60	11.2	0.29	4.403E-05	4.34	2.86	0.78
7	2.100	0.457	4.60	11.2	0.29	4.403E-05	4.34	2.86	0.78
8	2.100	0.457	4.60	11.2	0.29	4.403E-05	4.34	2.86	0.78
9	2.100	0.457	4.60	10.2	0.25	4.404E-05	4.59	2.96	0.78

Note:

For the calculation of residence times of the gas/solid for the experimental data in **Fig. 2.3**, the following equation,

$$t_{gas/solid} = \frac{L_{isothermal\text{-}zone}}{u_{gas/solid}}$$

was used, where *t* represents the residence time of gas/solid, s; *L* refers to the length of isothermal zone of the drop tube reactor, m; and u is the rate of gas/solid, m/s.

For the residence times of the gas (t_{gas}), they were estimated based on the flow rate of both carrier gas (nitrogen) and steam supplied to the DTR (in **Table 2.5**), without considering the effect of volatile matters released from coal on the total gas flow rate.

For the residence times of the solid particle (t_{solid}), they were determined as the sum of the residence times of solid particles at the acceleration region ($u \le u_t$) and steady region ($u = u_t$). The terminal velocities of solid particles in the steady region were estimated based on a published empirical equation [40] below and were given in **Table 2.5**.

$$u_t = \sqrt{\frac{4\left(\rho_s - \rho_g\right) g d_s}{3\rho_g \zeta}} \qquad (2 < Re_s < 500)$$

$$\zeta = \frac{10}{\sqrt{Re_s}}$$

where the diameter (d_s) and density (ρ_s) of solid particle are 0.006 m and 1300 kg/m^3, respectively; The acceleration of gravity (g) is 9.8 m/s^2; ρ_g is the density of gas; ζ is the resistance coefficient; Re_s is the Reynolds number of solid particle. u_t is the terminal velocity of solid particle.

Table 2.6. Result of estimated apparent rate constants at different temperatures.

Apparent rate constant (s^{-1})	Temperature (°C)		
	700	800	900
K_{12}: Tar→Gases	0.30	0.90	2.60
K_{21}: Gases→Tar	0.30	0.73	1.50
K_{13}: Tar→Char	1.00	2.30	4.60
K_{14}: Tar→Soot	0.20	0.90	1.20
K_{32}: Char→Gases	0.013	0.040	0.078
K_{42}: Soot→Gases	0.10	0.30	0.95

Table 2.7. The pre-exponential factor (A) and apparent activation energy (E_a) for each apparent rate constant.

Apparent rate constant (s^{-1})	Pre-exponential factor (s^{-1})	Apparent activation energy (kJ/mol)
k_{12}: Tar→Gases	9.0E+04	102.2
k_{21}: Gases→Tar	3.8E+03	76.4
k_{13}: Tar→Char	7.7E+03	72.4
k_{14}: Tar→Soot	1.0E+04	86.5
k_{32}: Char→Gases	6.0E+02	86.6
k_{42}: Soot→Gases	5.0E+04	106.4

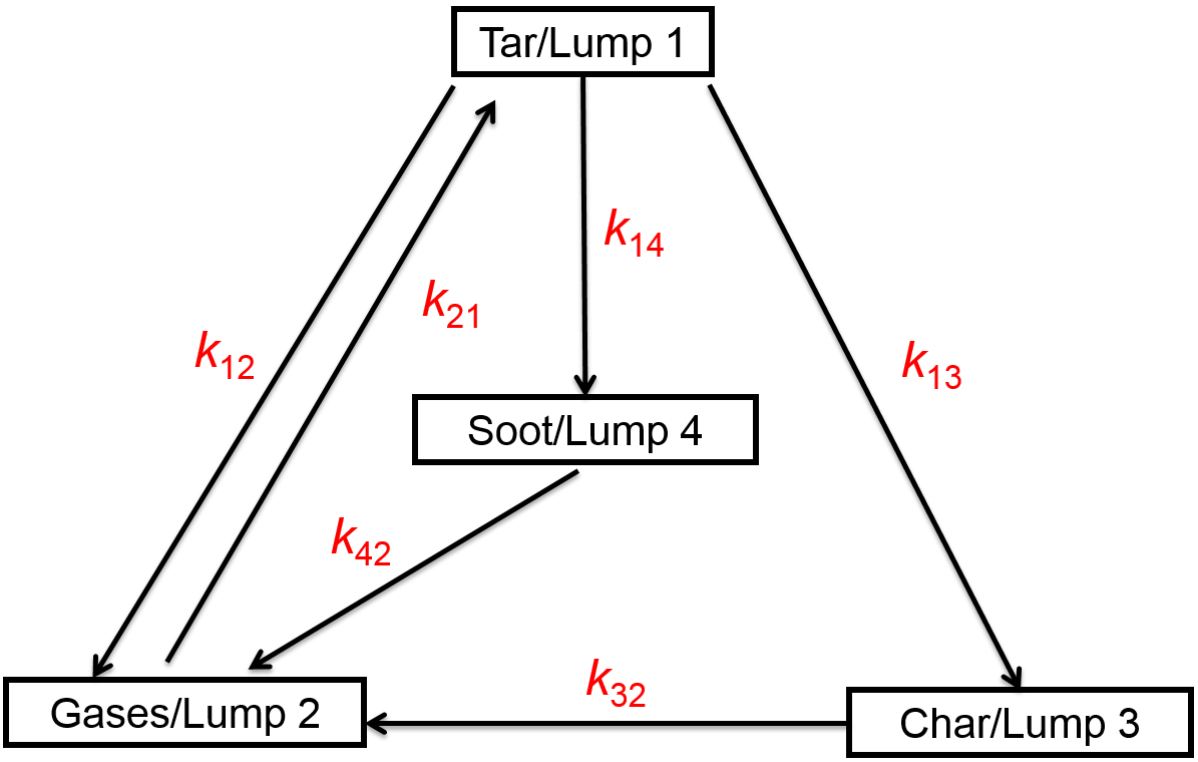

Fig. 2.1. Schematic diagram of the four-lump reaction network in the DTR coal conversion process accounting for the volatiles-char interaction.

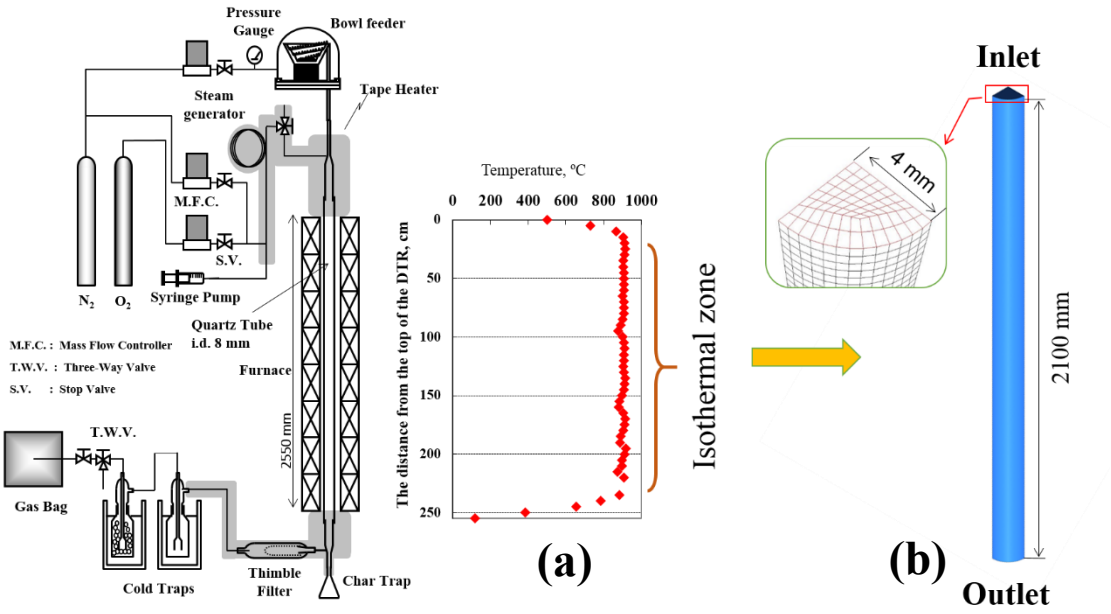

Fig. 2.2. The isothermal zone (a) and the simplified geometry used for the CFD simulation (b) of the drop tube reactor.

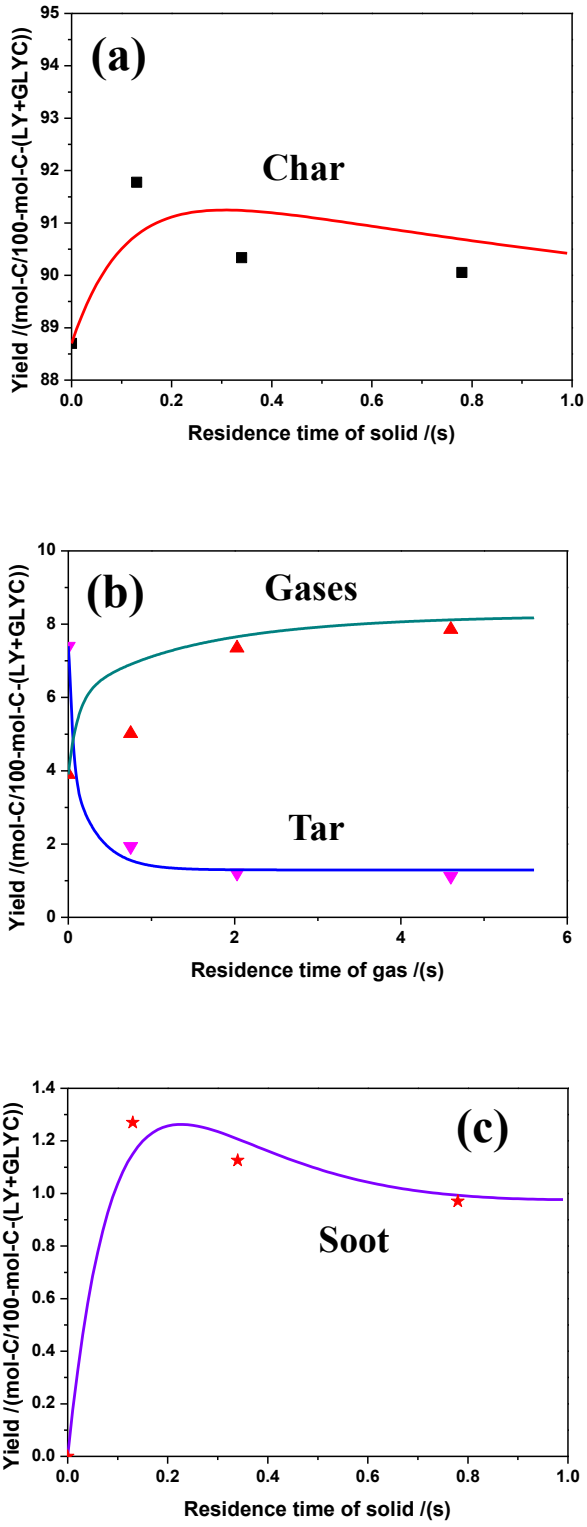

Fig. 2.3. Experiment yields and calculated yields *vs.* residence time. (at reaction temperature: 900 °C; steam partial pressure: 0.05 MPa; feeding rate: 0.5 g/min); (a) Char, (b) Tar and gases, (c) Soot. Symbols and solid lines represent the experimental results and model calculations, respectively.

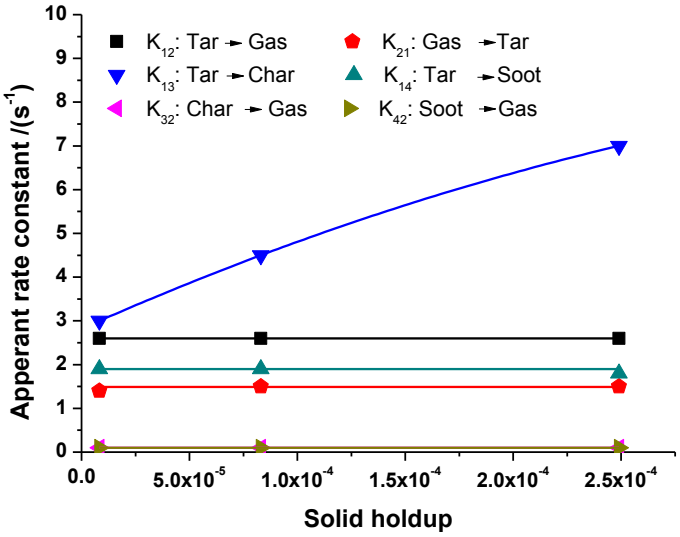

Fig. 2.4. The correlation between the estimated apparent rate constant and solid hold-up (at reaction temperature: 900 °C; residence time: 4.6 s for gas, 0.78 s for solid particle; steam partial pressure: 0 MPa).

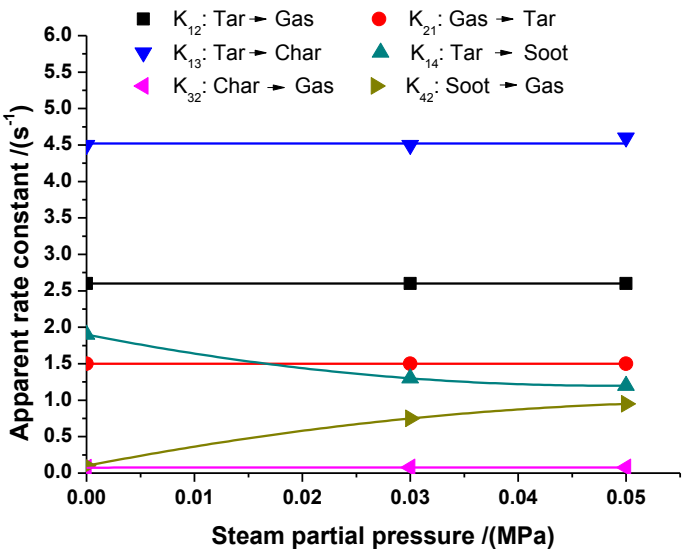

Fig. 2.5. The correlation between the estimated apparent rate constant and steam partial pressure (at reaction temperature: 900 °C; residence time: 4.6 s for gas, 0.78 s for solid particle; feeding rate: 0.5 g/min).

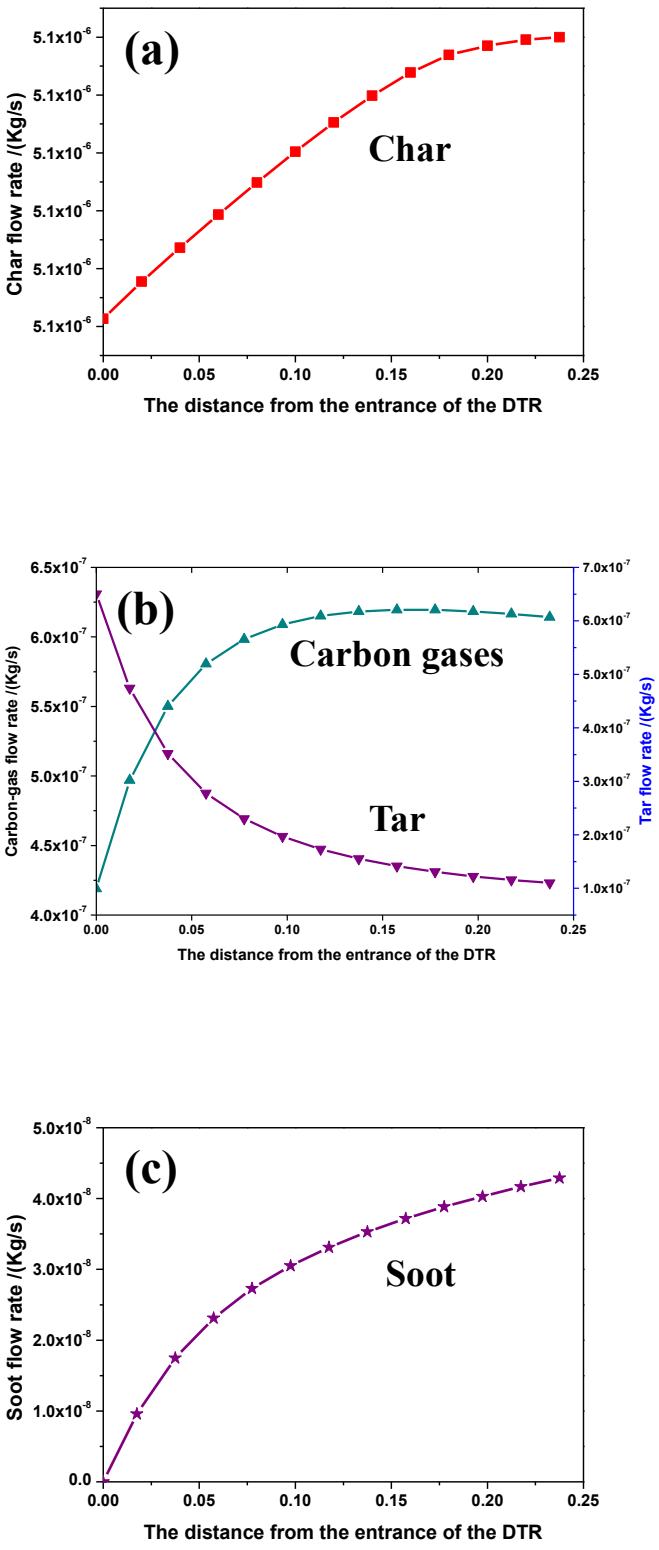

Fig. 2.6. The total mass flow rate (area-weighted average) of different lumps along the distance from the entrance of the DTR (in run 4, (a) Char; (b) Carbon gases and tar; (c) Soot).

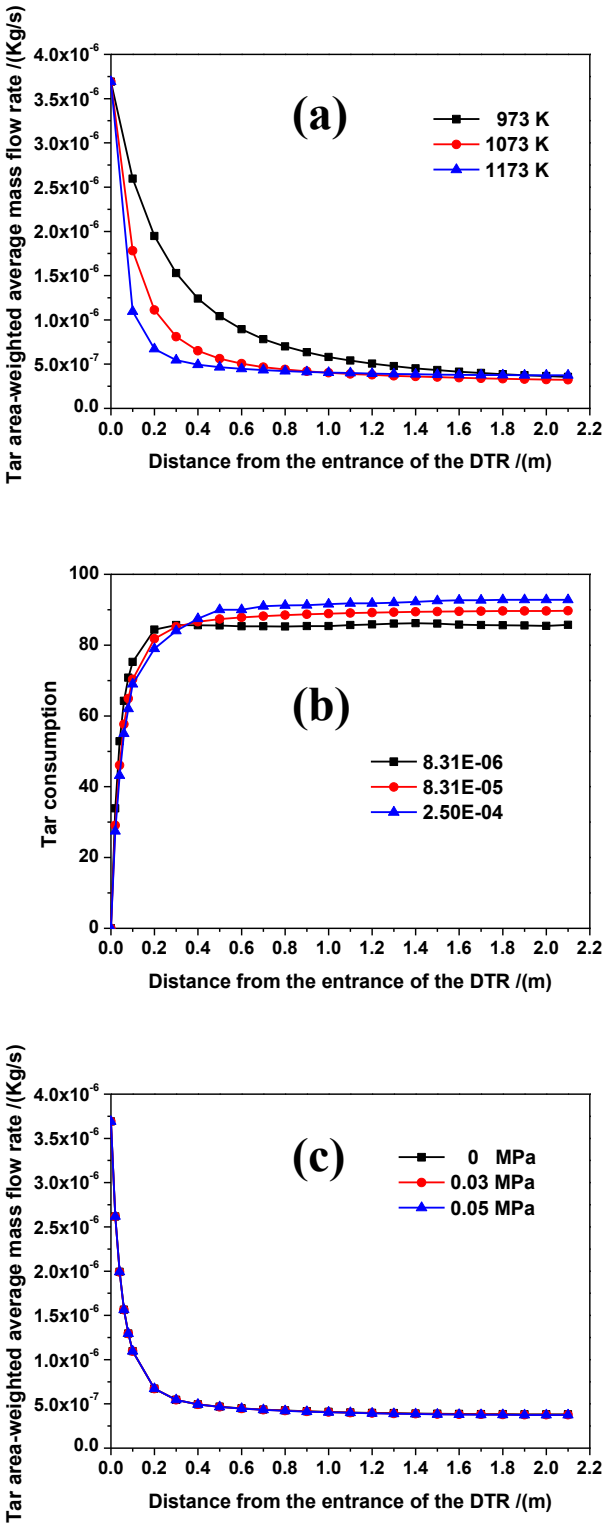

Fig. 2.7. The effect of reaction conditions (a. Temperature; b. Solid hold-up; c. Steam partial pressure) on tar consumption along the distance from the entrance of the DTR.

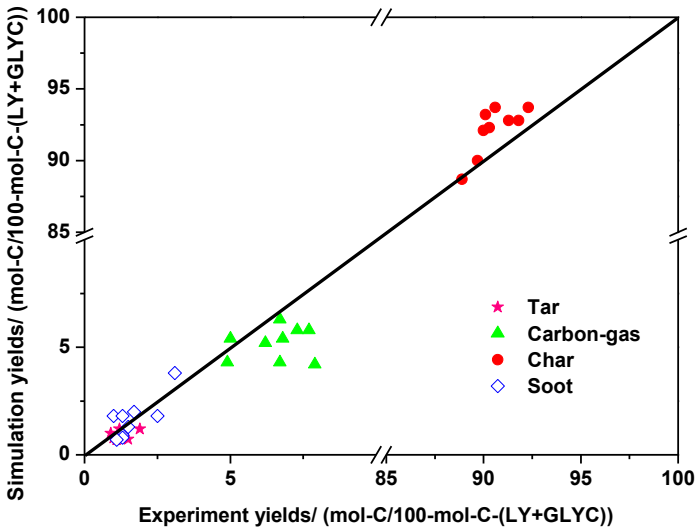

Fig. 2.8. Experimental yields *vs.* predicted yields for all experimental conditions used in this study.

Chapter 3

Non-catalytic reforming of coal gas containing tar using detailed chemistry and a one-dimensional flow model

3.1. Introduction

Efficient, cost-effective technologies to reform hydrocarbon fuels are needed to encourage future H_2 utilisation. One promising source of H_2 is coke oven gas (COG), which is a by-product in coke production, emitted at 300–350 Nm^3 per ton of coal [1]. The hot coke oven gas (HCOG) released from a coke oven is a multicomponent gas mixture, containing tarry compounds and steam in addition to H_2, CO, CO_2, and CH_4 [2–4]. The tar contains mono- and polycyclic aromatic hydrocarbons and comprises approximately 30 wt% of the HCOG [5]. In the conventional coke-making process, the HCOG is quenched to remove condensing components such as tar and water. The dry COG is used as fuel in steelworks and contains 54–59 mol.% H_2 and 24–28 mol.% CH_4 [6]. The amount of H_2 in dry COG can be amplified by catalytic [7,8] or non-catalytic [9,10] reforming by CO_2 or steam. Clean (tar-free) gas production by direct reforming of HCOG (without a cooling process) has been studied as an efficient process by utilising the HCOG heat [2,11,12]. The products from the partial oxidation of HCOG reforming are also suitable as feedstock for methanol production [13]. HCOG typically contains 0.3 wt% H_2S [11], which can deactivate the reforming catalysts. Catalytic deactivation by sulphur compounds [14,15] and coke [16–18] is unavoidable; these problems make non-catalytic reforming an attractive option for HCOG reforming.

Non-catalytic partial oxidation is conducted in a reactor by feeding HCOG and air in a sub-stoichiometric ratio, which results in temperature >1500K [11]. The high temperature and steam produced by the partial oxidation process are used to sustain the endothermic reforming reactions [19,20]. There are many commercial and technical benefits of applying the numerical simulations based on the reliable reactor models, which helps in designing the reactor and optimizing the process operation. Prediction of the axial temperature profile without using empirical information is important for the design and operation of an exothermic partial oxidation process. Many flow reactor simulations have been carried out based on pre-existing/empirical temperature profiles [13,21,22] or with assumptions such as isothermal and negligible axial diffusion. For example, hydrocarbon pyrolysis experiments have been simulated numerically with a detailed kinetic model [23] coupled with a plug flow reactor model [21], where empirical temperature profiles were used as input for plug flow simulations. Sheng *et al*. [22] emphasised the importance of gas-phase kinetics in anode channel solid oxide fuel cells and used a model with an empirical axial temperature profile. Previously, we approximated the experimental axial temperature profile of a HCOG reformer as an empirical polynomial, validating it based on an empirical temperature profile with the assumption of negligible axial diffusion [13]. These empirical temperature profiles were developed based on limited temperature measurements and might introduce uncertainty in model predictions. Axial diffusion causes a degree of mixing in the axial direction in real reactors, the plug flow reactor model is appropriate when this effect is sufficiently small that it can be ignored. Diffusion can

occur because of the concentration gradient in the axial direction. It is usually less important than bulk flow in most practical systems. However, the inclusion of axial diffusion in plug flow reactor models may give information about the deviation from ideality, which is generally present in real reactor systems [24].

The primary importance of this paper is that it estimates the axial temperature profiles for the partial oxidation of HCOG using a new numerical approach. The heat losses to the surroundings and non-ideality of the plug flow with axial diffusion are accounted for in numerical simulations. An existing kinetic model proposed by Richter and Howard [25] is used to simulate the pilot-scale HCOG reforming. The kinetic model consists of more than 2000 elementary steps, such as reactions, and is capable of accurately capturing phenomena that occur in the gas-phase reactions. The kinetic model is validated with experimental observations of the major components, such as H_2, CO, CO_2, and CH_4, and the total dry gas flow rate, in addition to the axial temperature profiles of 19 pilot-scale runs.

3.2. Pilot-scale Test of HCOG Reforming

A pilot-scale test plant for HCOG reforming with partial oxidation was installed on a platform of an operating coke oven at Kitakyushu city, Japan. The HCOG was collected from three coke chambers and introduced to the reformer at a temperature range of 625- 665 K together with O_2 at room temperature. The HCOG flow rate was adjusted by the dampers, which were placed at the top of the coke oven chambers.

HCOG was fed into a horizontal cylindrical section (0.6-m ID and 3.24 m long) at flow rates from 45 to 63.9 Nm^3/h and was partially oxidized by O_2 (from 14.2 to 19.4 Nm^3/h) from the four nozzles near the inlet. The reformer was operated at atmospheric pressure. Temperature profiles were measured with thermocouples inserted vertically at different positions inside the reformer. The gas compositions at the reformer inlet and outlet were measured using an online gas chromatography, and condensing products such as water and tar were sampled and analysed offline. The details of the pilot-scale test procedure have been reported elsewhere [13]. Pilot-scale measurements of 19 runs were used to validate the numerical approach.

The HCOG is a multicomponent gas mixture, particularly it contains around 30 wt.% tar compounds that include various mono and polycyclic aromatic compounds. Due to this nature, reforming of HCOG by partial oxidation is a complex process. Chemistry and kinetics are essential to understand the complex reforming process. HCOG contains large fractions of CH_4, and H_2, and these species are participating in combustion reactions with O_2, thereby accelerating the reforming of the tar by steam. The water produced from the CH_4 and H_2 oxidations, and reverse water- gas shift reaction, in addition to these water formation reactions, HCOG also contains some fraction of H_2O, may induce reforming reactions. Most likely, these exothermic oxidation reactions were dominating at the reactor entrance, and later endothermic reforming reactions are taking place.

3.3. Modelling Approach

A one-dimensional flow reactor model coupled with heat losses to the surroundings was used to simulate the HCOG reforming pilot-scale tests. The real reactor is shown schematically in

Figure 3.1. For the numerical simulations, the flow reactor was idealised as a 3.2-m-long tube reactor with a constant inside diameter of 0.6 m.

3.3.1 Plug Flow Model

A plug flow reactor model was implemented by assuming ideal gas behaviour and constant pressure. The total continuity equation is written as

$$\frac{d(\rho u A_c)}{dz} = 0 \tag{3.1}$$

The species transport in a reactor model is described as

$$\rho u A_c \frac{dY_k}{dz} = A_c \dot{\omega}_k W_k, \qquad k = 1,..., K_g \tag{3.2}$$

and the energy equation considering heat loss to the surroundings is written as

$$\rho u C_p \frac{dT}{dz} - \frac{d}{dz}\left(\lambda \frac{dT}{dz}\right) + \sum h_k \dot{\omega}_k W_k = U_{loss}(T - T_{amb}) \frac{A_s}{A_c}. \tag{3.3}$$

In these equations, ρ is the density in kg/m^3, u is the velocity in m/s, Y_k is the mass fraction of species k, λ is the thermal conductivity of the mixture in J/(m·s·K), h_k is the specific enthalpy in J/kg, ω_k is the molar production rate of species (mol/(m^3·s)), W_k is the molecular weight of species k in kg/mol, U_{loss} is the overall heat transfer coefficient relating the heat loss from the reactor to the atmosphere in J/(m^2·s·K), A_s is the surface area per unit length, A_c is the cross-sectional area, T is the gas phase temperature, and T_{amb} is the atmospheric temperature.

3.3.2 1D- Flow Model with Axial Diffusion

The total continuity equation was the same as above, and species transport in a reactor model with axial diffusional resistance is described as

$$\rho u \frac{dY_k}{dz} + \frac{dj_k}{dz} = \dot{\omega}_k W_k, \quad k = 1,..., K_g, \tag{3.4}$$

where j_k is the mass flux of species (kg/m^2·s) given by

$$j_k = -\rho D_{km} \frac{dY_k}{dz}. \tag{3.5}$$

The energy equation that considers the heat loss from the reactor wall to the atmosphere is represented as

$$\rho u C_p \frac{dT}{dz} - \frac{d}{dz}\left(\lambda \frac{dT}{dz}\right) + \frac{d}{dz}\sum_k j_k h_k + \sum_k h_k \dot{\omega}_k W_k = U_{loss}(T - T_{amb}) \frac{A_s}{A_c}, \tag{3.6}$$

and the density is calculated from the equation of the state

$$p \bar{w} = \rho R T. \tag{3.7}$$

The mass fluxes are calculated in such a way that the total flux is conserved, *i*.e.,

$$\sum_{k=1}^{K_g} j_k = 0. \tag{3.8}$$

The diffusion coefficient is calculated using

$$D_{km} = \frac{1 - Y_k}{\sum_{j \neq k}^{K_g} X_j / D_{jk}}. \tag{3.9}$$

Here, D_{km} is the diffusional coefficient of species k in the mixture, and X_j is the mole fraction of species j. The binary diffusion coefficient is calculated from Chapman–Enskog theory [26].

3.3.3 Detailed Kinetic Model

We used an existing detailed kinetic model [27] developed by Richter and Howard that consists of 2216 elementary irreversible reactions with 257 chemical species ranging in size from the smallest radical (the hydrogen radical) to the largest molecule (coronene). This mechanism was applied successfully to predict the aromatic hydrocarbon conversions in the presence of hydrogen and steam [28]. The thermodynamic data for the species involved in the mechanism and the rate constants were used without modification.

3.3.4 Numerical Simulations

A one-dimensional reactor model coupled with the detailed kinetic model was used for numerical simulations. A portion of the HCOG was sampled from the gas stream. Tarry constituents were condensed and weighed to determine the total tar concentration in HCOG, which was varied from 44 to 126 g/Nm^3. Tar was approximated to be a mixture of 31 aromatic hydrocarbons as done in our previous works [13,29] and the abundances of the compounds were estimated based on the quantitative analysis by Kirton et al [5]. **Table 3.1** shows the composition of the feed HCOG for numerical simulation (run 11), and those for all 19 runs are provided in the **Appendix A.I**. All of the runs of the HCOG partial oxidation experimental results were used to validate the model, not only with axial temperature profiles but also with major gas-phase species such as H_2, CO, CO_2, and CH_4. The implicit code LIMEX [30] for the plug flow model or CVODE [31] for the axial diffusion flow model was used to solve the coupled governing equations describing the numerical model. The DETCHEM^{PLUG} [32] was partially customized and used for the plug flow simulation. Global sensitivity analysis was carried out for the major gas-phase species to understand the dominant and important reactions in the mechanism.

3.4. Results and Discussion

3.4.1 Plug Flow Model

A temperature measurement along the axial position of the reactor indicated that the temperature was high near the reactor inlet and decreased towards the exit. The initial increase in temperature was due to the exothermic partial oxidation, and the decreasing trend was due

to the endothermic reforming. The initial simulations were performed with an ideal plug flow model [32] under adiabatic conditions, but these failed to predict the temperature profile (**Figure 3.2**). Because the reactor inlet temperature is lower than the ignition temperature of the mixture, the reaction mixture is force ignited in the numerical simulations. In this method, the reaction rates are calculated at a pre-defined ignition temperature, which results in a change in the enthalpy of the mixture so that eventually, the mixture temperature exceeds the pre-defined ignition temperature due to the exothermic reactions. Once the mixture temperature exceeds the pre-defined ignition temperature, the reaction rates are calculated using the actual mixture temperature.

Figure 3.2 shows the temperature profile (run 11) as a function of axial position under adiabatic conditions. When the pre-defined ignition temperature was too high, *e.g.*, 1000 K, the reaction rate was very high, and the gas phase temperature increased suddenly within a few centimetres of the reactor inlet; this was not captured the thermocouple measurement at near the reactor inlet, so the profile is flat. In another case, at a pre-defined ignition temperature of 850 K, the supplied energy was not able to ignite the fuel mixture, and the predicted temperature profile showed a constant temperature after ignition. At an ignition temperature of 900 K, the profile was sluggish and showed a sharp increase. This procedure optimised the ignition temperature and predicted the sharp increase and first thermocouple measurement at 950 K, although it failed to predict the complete trend. This might be because in the actual pilot-scale reactor, there is heat loss to the surroundings, and the numerical model neglects this loss.

To capture the complete profile, heat loss to the surroundings was also considered by introducing the overall heat transfer coefficient. A DETCHEM^{PLUG} code [32] was partially customized to implement the heat loss from the reactor wall to the surroundings. **Figure 3.3** shows the effect of heat losses to the surroundings at a fixed ignition temperature 950 K. When the overall heat transfer coefficient U_{loss} was zero, the predicted temperature was uniform throughout the reactor, *i.e.*, adiabatic conditions, and the predicted temperature profile far exceeded the experimental measurements. When U_{loss} was 10 W/m^2 K, more heat was lost from the reactor, and the predicted profile was far below the actual temperature profile. The predicted profile was just above the measured profile when U_{loss} was 2 W/m^2 K. The experimental temperature profile (run 11 of 19 runs) was captured accurately when the overall heat transfer coefficient was 4 W/m^2 K.

3.4.2 Critical Evaluation

Figure 3.4 shows the model predictions with axial temperature observations of the HCOG reformer for 19 runs. All of these predictions used an overall heat transfer coefficient of 4 W/m^2 K and an ignition temperature of 950 K. A large difference was observed between the predicted and measured temperature at the first thermocouple location, which was located at the reactor inlet. However, except at near the reactor inlet, the ratio between the predicted and measured temperature at different thermocouple locations varies from 0.95 to 1.13 and were generally within ±10% error. These ratios indicate that the model well predicts the axial temperatures at different locations of the reformer except at near the reactor inlet. The parity plot between the model predictions and measured temperatures along the axial position of the reformer was provided in **Figure 3.5**. The initial sharp rise in temperature near the reactor inlet was due

mainly to the exothermic partial oxidation reactions of light hydrocarbons and H_2 combustion.

Figure 3.6 compares the predicted dry gas mole fractions at the reactor outlet with pilot-scale reforming runs for major species such as H_2, CO, CO_2, and CH_4 for the 19 test runs. The range of ratios of the volume % predicted numerically to those measured were 0.96–1.02, 1.11–1.29, 0.65–0.9, and 0.09–0.94 for H_2, CO, CO_2, and CH_4, respectively. Overall, the predictions were in good agreement with the pilot-scale runs. Our kinetic model does not contain H_2-yielding gas-solid reactions, such as carbon deposition and soot-formation mechanisms. Many factors account for the over- and under-predictions, such as the accumulation of coke on the reactor wall. The deposition of carbon reduces the gas volume, but increases the H_2 concentration.

Figure 3.7 compares the numerically predicted dry gas flow rates at the rector outlet with measured flow rates in the HCOG reformer. The simulation tended to over-predict the outlet flow rate, mainly due to the over decomposition of hydrocarbons induced by over-predicted temperatures near the reactor entrance.

3.4.3 Sensitivity Analysis

In all the pilot-scale runs, H_2, CO_2, and CH_4 were under predicted, whereas CO was over-predicted. To understand these disagreements qualitatively, a global sensitivity analysis of major gas phase species was carried out with HOMREA [33], a software package designed for homogeneous reaction systems. High sensitivity coefficients have a substantial influence on the model predictions. A positive sensitivity coefficient indicates that the reaction enhances the species production rate or slows its consumption rate, whereas a negative sensitivity coefficient indicates the opposite. Although the kinetic model contains 2216 reactions, only a few reactions were found to be sensitive for the H_2, CO, CO_2, and CH_4 predictions. **Figure 3.8** shows the sensitivity analysis for the major gas species. Only four and 15 reactions were sensitive to the CO_2 and H_2 predictions, respectively, and 13 reactions to CO and CH_4 in a complex reaction network.

Figure 3.8a shows the sensitive coefficients (R1–R15) for H_2; reaction R2 was the most sensitive for the production of H_2, whereas the consumption of H_2 was more sensitive to reaction R1. Reaction R1 might be responsible for the under-prediction of H_2 in most of the runs. The sensitivity coefficients for CO are shown in **Fig. 3.8b**. Reactions R1 and R6 were more sensitive to the CO production rate, whereas the CO consumption was influenced mostly by reactions R2 and R5. The over-prediction of CO was due mainly to reactions R1 and R6.

Figure 3.8c shows the sensitivity coefficients for CO_2. Reactions R1 and R18 were more sensitive for CO_2 consumption, whereas the CO_2 production was influenced more by reactions R2 and R3. The plug flow model predicted CO_2 values lower than the experimental measurements due mainly to reactions R1 and R18. The sensitivity coefficients for CH_4 are shown in **Fig. 3.8d**. The consumption of CH_4 was more sensitive to reactions R8 and R11, which might be responsible for the under-prediction of CH_4 in all of the runs. Reaction R12 was sensitive to the production of CH_4. However, the activation energy of reaction R8 was very high (439 kJ/mol), which indicates that the reaction was the most temperature sensitive. The kinetic model predicted a higher temperature than the actual value at near the reactor inlet, which might cause greater consumption of CH_4 via partial oxidation, which is another reason

for the under-prediction of CH_4. Nevertheless, the under- and over-predictions of gas-phase species composition were due mainly to the over-predicted reaction temperatures and deviation from ideal behaviour. Overall, the under-prediction of H_2 and CO_2, and over-prediction of CO were greatly influenced by reaction R1, and reactions R8 and R11 were responsible for the under-prediction of CH_4.

3.4.4 Flow Model with Axial Diffusion

The ideal plug flow reactor models neglect axial diffusion. However, the presence of axial diffusion causes a distortion of the concentration profile, as commonly known as dispersion, in the axial direction of real reactors. Therefore, neglecting the axial diffusion term in a plug flow reactor model can lead to uncertainty in the model predictions. The predicted temperature rose suddenly near the reactor inlet in the absence of diffusion flow resistance (**Figure 3.2**). This behaviour results mainly from the exothermic H_2 combustion. The high diffusion coefficient of H_2 [34] might be responsible for a sharp rise in temperature, as it was present in significant amounts in the HCOG mixture. The addition of the diffusion term to the flow modelling provides considerable insight into the operation of a realistic reactor.

The model predictions of the major gas phase species mole fractions before and after the addition of diffusional flow as a function of axial position are presented in **Fig. 3.9**. The upper plots show the temperature profiles (left, plug flow; right, flow with axial diffusion), and the lower plots show the gas-phase species composition. A smooth profile is observed in the model with axial diffusion. These smooth profiles are due primarily to the complete HCOG mixing with oxygen and the axial diffusion of chemical species, particularly H_2, resulting in a reduction of the sharp rise in temperature near the reactor inlet. Sudden changes are observed in steam composition in both the plug flow model and axial diffusion flow model near the reactor inlet. This sudden rise in steam composition is due mainly to the two dominant exothermic reactions: H_2 combustion and partial oxidation of CH_4.

In both the cases, the injected O_2 was consumed completely by HCOG near the reactor inlet; as a result, the mole fractions of H_2O and CO_2 started increasing. The water concentration reached a maximum at a reactor length of 0.1 m and then decreased. Downstream from the reactor, the mole fractions of H_2O and CH_4 decreased, and the CO and H_2 mole fractions increased, indicating CH_4 reforming. The major gas phase species reached a steady state at 0.3 m from the reactor inlet. This indicates that the major reactions during the HCOG reforming by partial oxidation and steam reforming were nearly complete.

The pilot-scale measurements of run 11 were used to validate the diffusional flow model. Numerical simulations were performed with boundary and inlet conditions identical to those of run 11. The predictive capabilities of the plug flow and axial diffusion models are compared in **Figure 3.10**, where the predicted values were plotted against measured ones. Significant improvements were observed mainly in the CH_4 predictions, and slight improvements in the H_2, CO, and CO_2 mole fraction predictions at the reactor exit. For example, in one of the pilot scale runs, the CH_4 predictions by the axial diffusion model and plug flow model were 1.15 mol.% and 0.68 mol.%, respectively. The experimentally measured value was 1.33 mol.%. The

improvements in the prediction arose mainly from a reduction in the sharp rise in temperature at the reactor entrance caused by the axial diffusion of the species.

Figure 3.11 shows the comparison between plug flow and axial diffusion model predictions for the dry gas flow rate versus those measured at the reactor exit. The model predictions of an axial diffusion model were very closed to the pilot scale measurements. The disturbances in the model predictions needs further research to examine our assumptions. The reforming features of HCOG may be captured more precisely by using multi-dimensional simulations. Further study will include CFD model coupled with detailed chemical kinetic model.

3.5. Conclusions

This study offers a new numerical approach for predicting the axial temperature profile for HCOG reforming by partial oxidation. One-dimensional reactor models were developed that considered the heat loss from the reactor wall to the surroundings (plug flow) and axial diffusion, validated with pilot-scale HCOG reforming with partial oxidation measurements. In the plug flow simulations, an ignition temperature option was used initially to calculate the reaction rates, and then the reaction rates were calculated using the gas-phase temperature. The overall heat transfer coefficient for heat losses from the reactor was optimised empirically at 4 $W/m^2 \cdot K$; with this value, the experimental axial temperature profiles of the HCOG pilot-scale runs were reproduced well. In the numerical simulations, a sharp rise in temperature was observed; this behaviour was unrealistic in a real reactor. The model predictions were validated exhaustively with 19 pilot-scale runs of axial temperature profiles along with the composition of the major gas phase species (H_2, CO, CO_2 and CH_4) and total dry gas flow rates. With the plug flow model, the ratios of gas composition (vol.%) between predicted and measured values were ranged 0.96–1.02, 1.11–1.29, 0.65–0.9, and 0.09–0.94 for H_2, CO, CO_2, and CH_4, respectively. Marked deviation was observed between the CH_4 model predictions and pilot-scale tests. A global sensitivity analysis was used to identify the temperature-sensitive reactions. The reaction of H_2 with OH forming H_2O and H was the reaction most responsible for the under-prediction of H_2 and CO_2 and over-prediction of the CO mole fractions. The CH_4 decomposition reaction giving CH_3 and H was more temperature sensitive and was responsible for the CH_4 under-prediction. The addition of a diffusion flow term in the reactor model provides considerable insight into the operation of a realistic reactor. Improved predictions are obtained with a 1D flow model with axial diffusion. The improvements in the model predictions are due primarily to the improved temperature predictions by accounting for axial diffusion in the flow model.

3.6. References

[1] T. Aramaki, Status of the coke oven gas in Japan, J. Jpn. Inst. Energy. 85 (2006) 342–347.

[2] K. Miura, M. Kawase, H. Nakagawa, R. Ashida, T. Nakai, T. Ishikawa, Conversion of tar in hot coke oven gas by pyrolysis and steam reforming., J. Chem. Eng. Japan. 36 (2003) 735–741.

[3] A. Jess, Catalytic upgrading of tarry fuel gases: A kinetic study with model components, Chem. Eng. Process. Process Intensif. 35 (1996) 487–494.

[4] A. Jess, Mechanisms and kinetics of thermal reactions of aromatic hydrocarbons from pyrolysis of solid fuels, 75 (1996) 1441–1448.

[5] J. Kirton, T. Crisp, The analysis of organic oven emissions in coke, Fuel. 70 (1991) 1383–1389.

[6] Y. Zhang, Q. Li, P. Shen, Y. Liu, Z. Yang, W. Ding, et al., Hydrogen amplification of coke oven gas by reforming of methane in a ceramic membrane reactor, Int. J. Hydrogen Energy. 33 (2008) 3311–3319.

[7] M. Kong, Q. Yang, J. Fei, X. Zheng, Experimental study of Ni/MgO catalyst in carbon dioxide reforming of toluene, a model compound of tar from biomass gasification, Int. J. Hydrogen Energy. 37 (2012) 13355–13364.

[8] W. Tao, H. Cheng, W. Yao, X. Lu, Q. Zhu, G. Li, et al., Syngas production by CO_2 reforming of coke oven gas over $Ni/La_2O_3–ZrO_2$ catalysts, Int. J. Hydrogen Energy. (2014) 1–9.

[9] S.G. Shen, P.P. Chen, A.Q. Li, H.F. Qin, B.B. Li, Y.P. Ren, Effect of three processes on CO_2 and O_2 simultaneously reforming of coke oven gas to syngas, Chem. Eng. Process. Process Intensif. 75 (2014) 75–80.

[10] J. Zhang, X. Zhang, Z. Chen, L. Li, Thermodynamic and kinetic model of reforming coke-oven gas with steam, Energy. 35 (2010) 3103–3108.

[11] M. Onozaki, K. Watanabe, T. Hashimoto, H. Saegusa, Y. Katayama, Hydrogen production by the partial oxidation and steam reforming of tar from hot coke oven gas, Fuel. 85 (2006) 143–149.

[12] M. Hashimoto, T ; Onozaki, Reforming of hot coke oven gas, Jpn. Inst. Energy. 85 (2006) 364–370.

[13] K. Norinaga, H. Yatabe, M. Matsuoka, J. Hayashi, Application of an existing detailed chemical kinetic model to a practical system of hot coke oven gas reforming by noncatalytic partial oxidation, Ind. Eng. Chem. Res. 49 (2010) 10565–10571.

[14] J.N. Kuhn, N. Lakshminarayanan, U.S. Ozkan, Effect of hydrogen sulfide on the catalytic activity of Ni-YSZ cermets, J. Mol. Catal. 282 (2008) 9–21.

[15] S. Appari, V.M. Janardhanan, R. Bauri, S. Jayanti, Deactivation and regeneration of Ni catalyst during steam reforming of model biogas: An experimental investigation, Int. J. Hydrogen Energy. 39 (2014) 297–304.

[16] H.Y. Wang, A.C. Lua, Deactivation and kinetic studies of unsupported Ni and Ni–Co–Cu alloy catalysts used for hydrogen production by methane decomposition, Chem. Eng. J. 243 (2014) 79–91.

[17] M. Guisnet, P. Magnoux, Catalyst deactivation, Proceedings of the 6th International Symposium, Elsevier, 1994.

[18] M. Guisnet, P. Magnoux, Coking and deactivation of zeolites influence of the pore structure, Appl. Catal. 54 (1989) 1–27.

[19] M. Halabi, M. Decroon, J. Vanderschaaf, P. Cobden, J. Schouten, Modeling and analysis of autothermal reforming of methane to hydrogen in a fixed bed reformer, Chem. Eng. J. 137 (2008) 568–578.

[20] T.P. Tiemersma, T. Kolkman, J. a. M. Kuipers, M. van Sint Annaland, A novel autothermal reactor concept for thermal coupling of the exothermic oxidative coupling and endothermic steam reforming of methane, Chem. Eng. J. 203 (2012) 223–230.

[21] K. Norinaga, V.M. Janardhanan, O. Deutschmann, Modeling of pyrolysis of ethylene, acetylene, and propylene at 1073–1373 K with a plug-flow reactor model, Int. J. Chem. Kinet. 40 (2007) 199–208.

[22] C.Y. Sheng, A.M. Dean, Importance of gas-phase kinetics within the anode channel of a solid-oxide fuel cell, J. Phys. Chem. A. 108 (2004) 3772–3783.

[23] K. Norinaga, O. Deutschmann, Detailed kinetic modeling of gas-phase reactions in the chemical vapor deposition of carbon from light hydrocarbons, Ind. Eng. Chem. Res. 46 (2007) 3547–3557.

[24] A. Bittante, J. Garc á-Serna, P. Biasi, F. Sobr ón, T. Salmi, Residence time and axial dispersion of liquids in trickle bed reactors at laboratory scale, Chem. Eng. J. 250 (2014) 99–111.

[25] H. Richter, J.B. Howard, Formation and consumption of single-ring aromatic hydrocarbons and their precursors in premixed acetylene, ethylene and benzene flames, Phys. Chem. Chem. Phys. 4 (2002) 2038–2055.

[26] R.B. Bird, W.E. Stewart, E.N. Lightfoot, Transport phenomena, revised 2nd edition, John Wiley & Sons, Inc., 2006.

[27] H. Richter, J.B. Howard, Formation and consumption of single-ring aromatic hydrocarbons and their precursors in premixed acetylene, ethylene and benzene flames, Phys. Chem. Chem. Phys. 4 (2002) 2038–2055.

[28] K. Norinaga, Y. Sakurai, R. Sato, J. Hayashi, Numerical simulation of thermal conversion of aromatic hydrocarbons in the presence of hydrogen and steam using a detailed chemical kinetic model, Chem. Eng. J. 178 (2011) 282–290.

[29] K. Norinaga, J. Hayashi, Numerical simulation of the partial oxidation of hot coke oven gas with a detailed chemical kinetic model, Energy & Fuels. 24 (2010) 165–172.

[30] P. Deuflhard, E. Hairer, J. Zugck, Numerische Mathematik, One-step and extrapolation methods for differential-algebraic systems, Springer-Verlag, Germany, 1987.

[31] B. Hindmarsh, Grant, Lee, Serban, Shumaker, Woodward, SUNDIALS: Suite of nonlinear and differential/algebraic equation solvers, ACM Trans. Math. Softw. 31 (2005) 363–396.

[32] O. Deutschmann, S. Tischer, S. Kleditzsch, V. Janardhanan, C. Correa, D. Chatterjee, et al., DETCHEM software package, 2.4 ed., Germany, 2013. www.detchem.com.

[33] J. Warnatz and U. Maas and R. W. Dibble, Combustion, physical and chemical fundamentals, modeling and simulation, experiments, pollutant formation, 3rd ed., Springer-Verlag Berlin Heidelberg GmbH, 2001.

[34] O. Deutschmann, L.D. Schmidt, Modeling the partial oxidation of methane in a short-contact-time reactor, AIChE J. 44 (1998) 2465–2477.

Table Captions

Table 3.1. Composition of the feed HCOG for numerical simulations (run 11).

Figure Captions

Figure 3.1. Schematic representation of pilot scale HCOG reformer.

Figure 3.2. The effect of ignition temperature on temperature distribution along the axial length of reactor.

Figure 3.3. The effect of overall heat transfer coefficient (heat losses from the reactor) on temperature distribution along the axial length of the reactor.

Figure 3.4. Comparison between model predictions and experimental observations of temperatures along the axial length of the reactor.

Figure 3.5. The parity plot between model predictions and measured temperatures along the axial position of the reformer.

Figure 3.6. Major gas compositions at the reformer outlet predicted by the plug flow numerical simulations versus those measured by the pilot scale tests for HCOG reforming by non-catalytic partial oxidation.

Figure 3.7. Dry gas flow rates at the reformer outlet predicted by the plug flow numerical simulation versus those measured by the pilot scale tests for HCOG reforming with non-catalytic partial oxidation.

Figure 3.8. Sensitivity analysis for major gas phase species such as H_2, CO, CO_2, and CH_4.

Figure 3.9. Comparison between temperature (top) and mole fraction (bottom) profiles without (left) and with (right) diffusional flow along the reactor axis during the HCOG reforming with partial oxidation (run 11).

Figure 3.10. Comparison of the reformed gas compositions predicted by the plug flow model and one dimensional flow with axial diffusion model with those measured by the pilot-scale tests for HCOG reforming with non-catalytic partial oxidation.

Figure 3.11. Comparison of the reformed gas flow rates predicted by the plug flow model and one dimensional flow with axial diffusion model with those measured by the pilot scale tests of HCOG reforming with non-catalytic partial oxidation.

Table 3.1. Composition of the feed HCOG for numerical simulation (run 11).

Compounds	Mole fraction
H_2	4.413E−01
CH_4	1.439E−01
C_2H_4	7.261E−03
C_2H_6	2.602E−03
CO	3.374E−02
CO_2	8.276E−03
N_2	2.279E−02
O_2	1.855E−01
H_2O	1.461E−01
Benzene	3.362E−03
Toluene	4.034E−04
Xylene	0.000E+00
Styrene	1.468E−04
Phenol	3.211E−04
Indene	4.221E−04
Naphthalene	2.346E−03
2-Methylnaphthalene	2.052E−04
1-Methylnaphthalene	9.145E−05
Acenaphthylene	1.616E−04
Acenaphthene	3.305E−05
Fluorine	1.015E−04
Phenanthrene	3.293E−04
Anthracene	8.282E−05
Cyclopenta[def]phenanthrene	1.293E−05
2-Phenylnaphthalene	6.022E−06
Fluoranthene	1.329E−04
Acephenanthrylene	5.213E−06
Aceanthrylene	4.344E−06
Pyrene	9.122E−05
Benzo[a]fluorine	7.312E−06
Cyclopenta[cd]pyrene	2.330E−06
Benz[a]anthracene	3.618E−05
Chrysene	3.848E−05
Benzo[b]fluoranthene	2.925E−05
Benzo[e]pyrene	2.228E−05
Benzo[a]pyrene	2.368E−05
Perylene	6.268E−06
Benzo[ghi]perylene	9.538E−06
Anthanthrene	3.815E−06
Coronene	1.170E−06

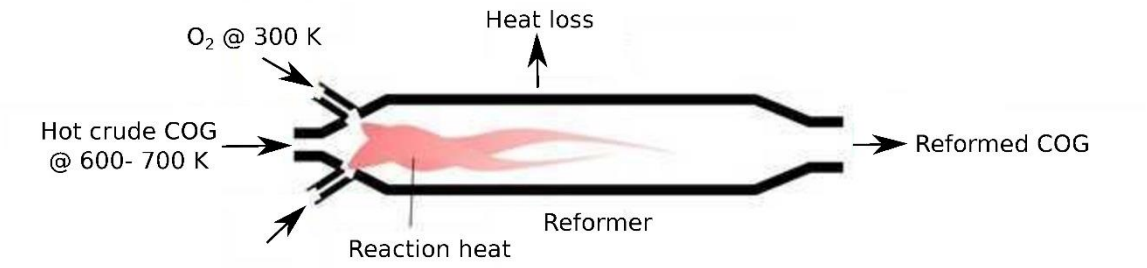

Fig. 3.1. Schematic representation of the pilot-scale HCOG reformer.

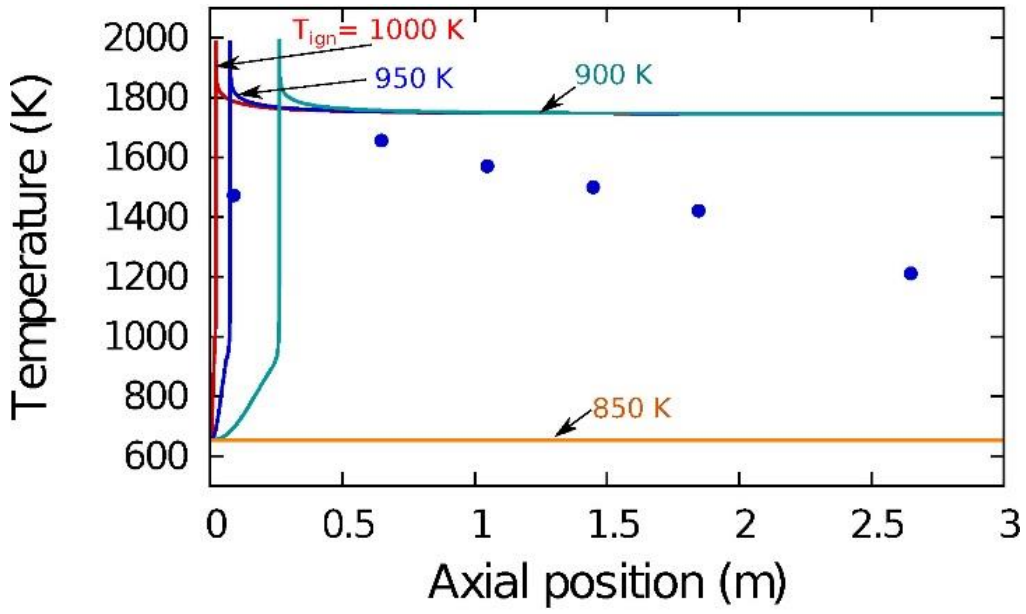

Fig. 3.2. The effect of ignition temperature on the temperature distribution along the axial length of reactor. The symbols indicate experimentally measured values, and the solid lines represent model predictions.

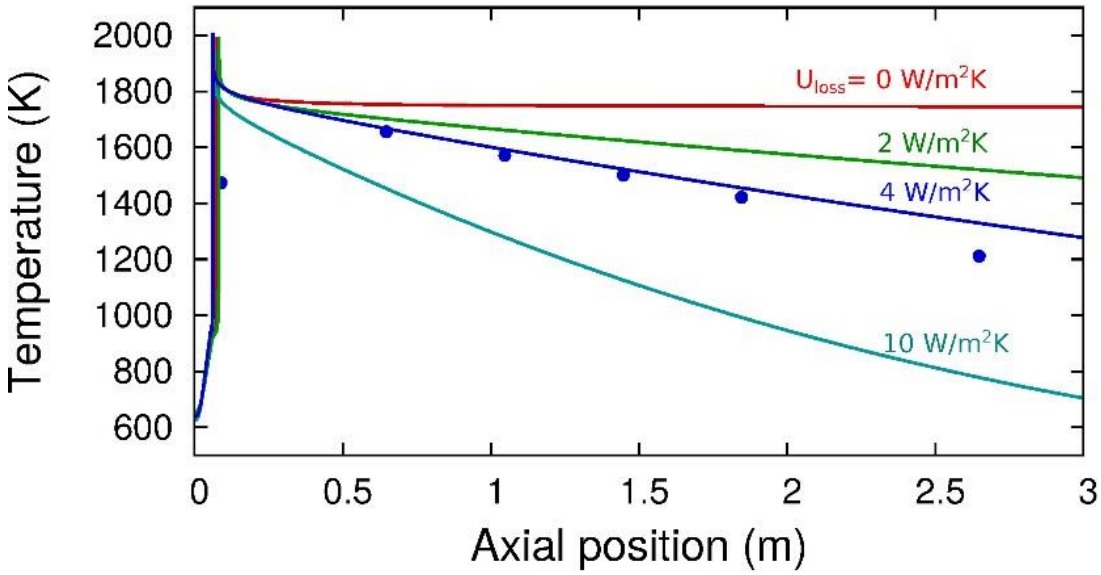

Fig. 3.3. The effect of the overall heat coefficient (heat losses from the reactor) on the temperature distribution along the axial length of the reactor. These plots were made with ignition at 950 K. The symbols indicate experimentally measured values, and the solid lines represent model predictions.

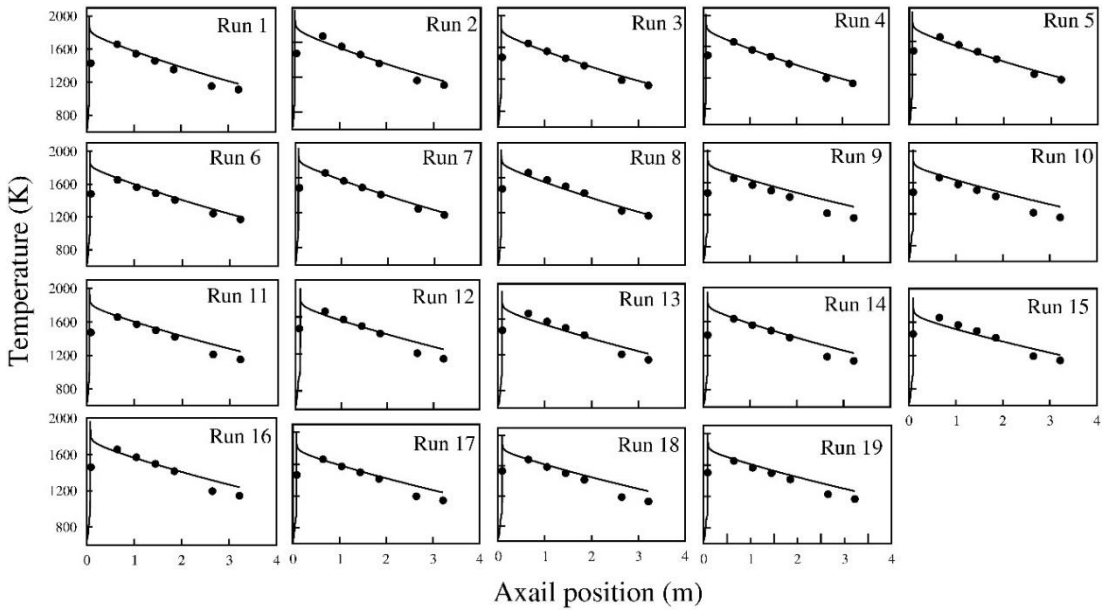

Fig. 3.4. Comparison of the model predictions and experimental observations of temperatures along the axial length of the reactor. The symbols indicate experimentally measured values, and the solid lines represent model predictions.

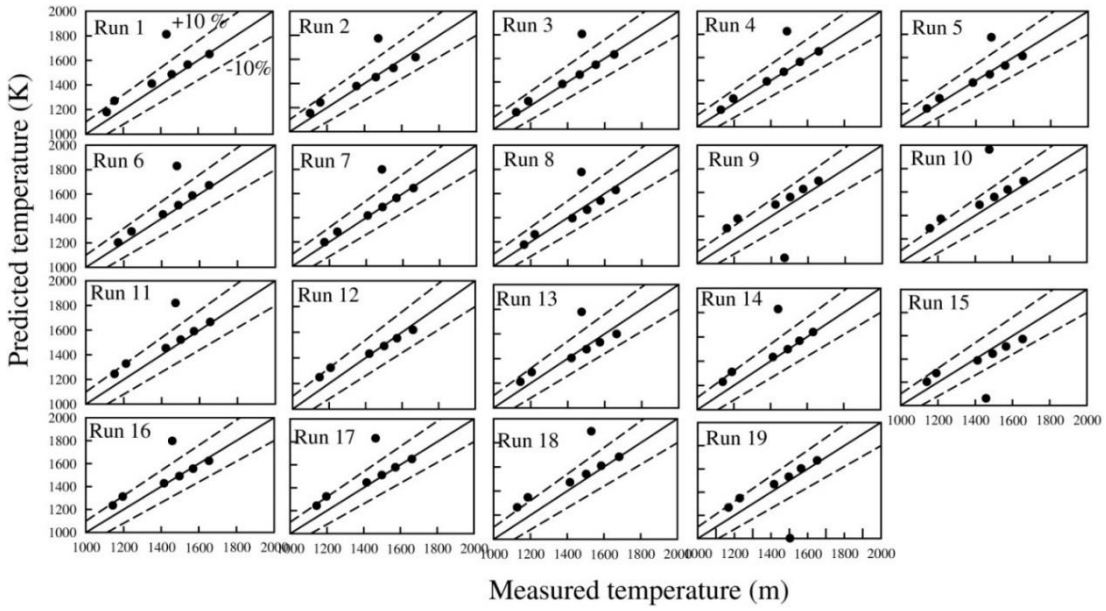

Fig. 3.5. Comparison between model predictions and measured temperatures along the axial position of the reformer. Dashed lines show the ±10 error in the model predictions.

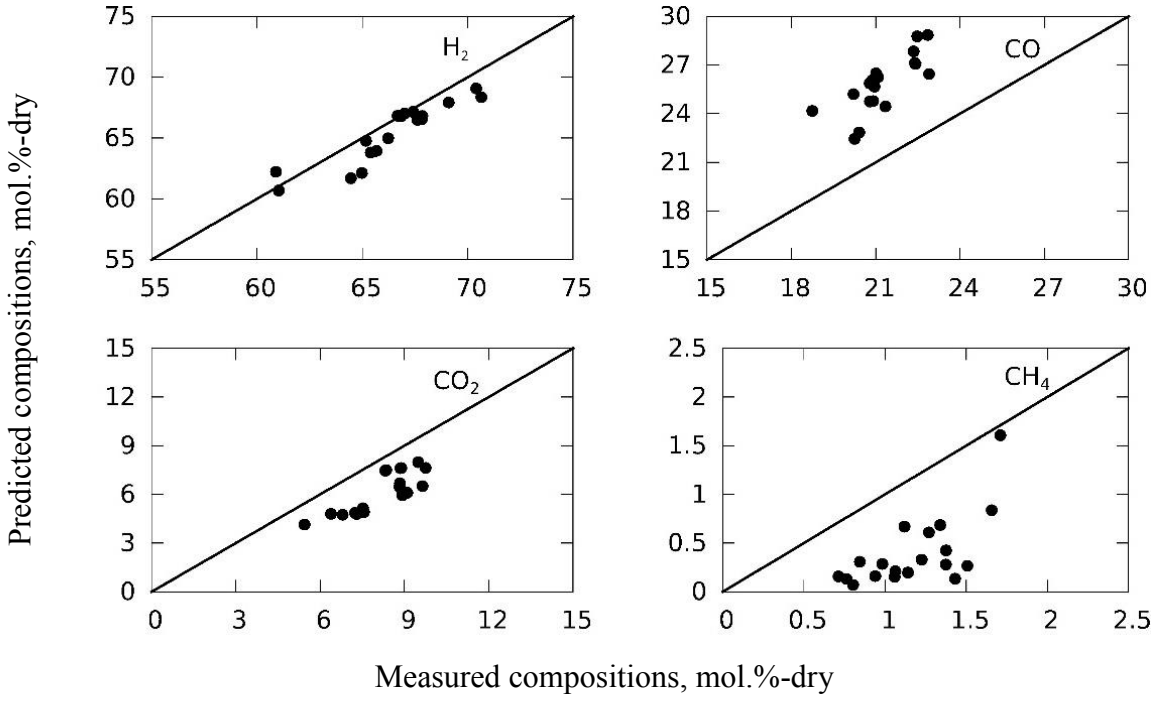

Fig. 3.6. Major gas compositions at the reformer outlet predicted by the plug flow numerical simulations versus those measured by the pilot-scale tests for HCOG reforming with non-catalytic oxidation.

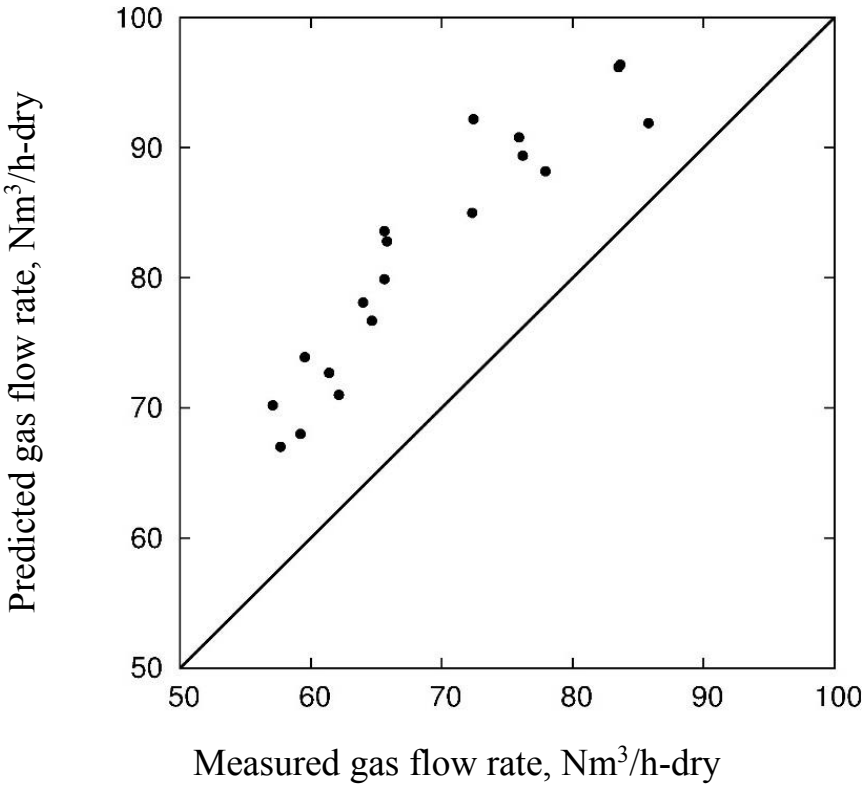

Fig. 3.7. Dry gas flow rates at the reformer outlet predicted by the plug flow numerical simulation versus those measured in the pilot-scale tests of HCOG reforming with non-catalytic partial oxidation.

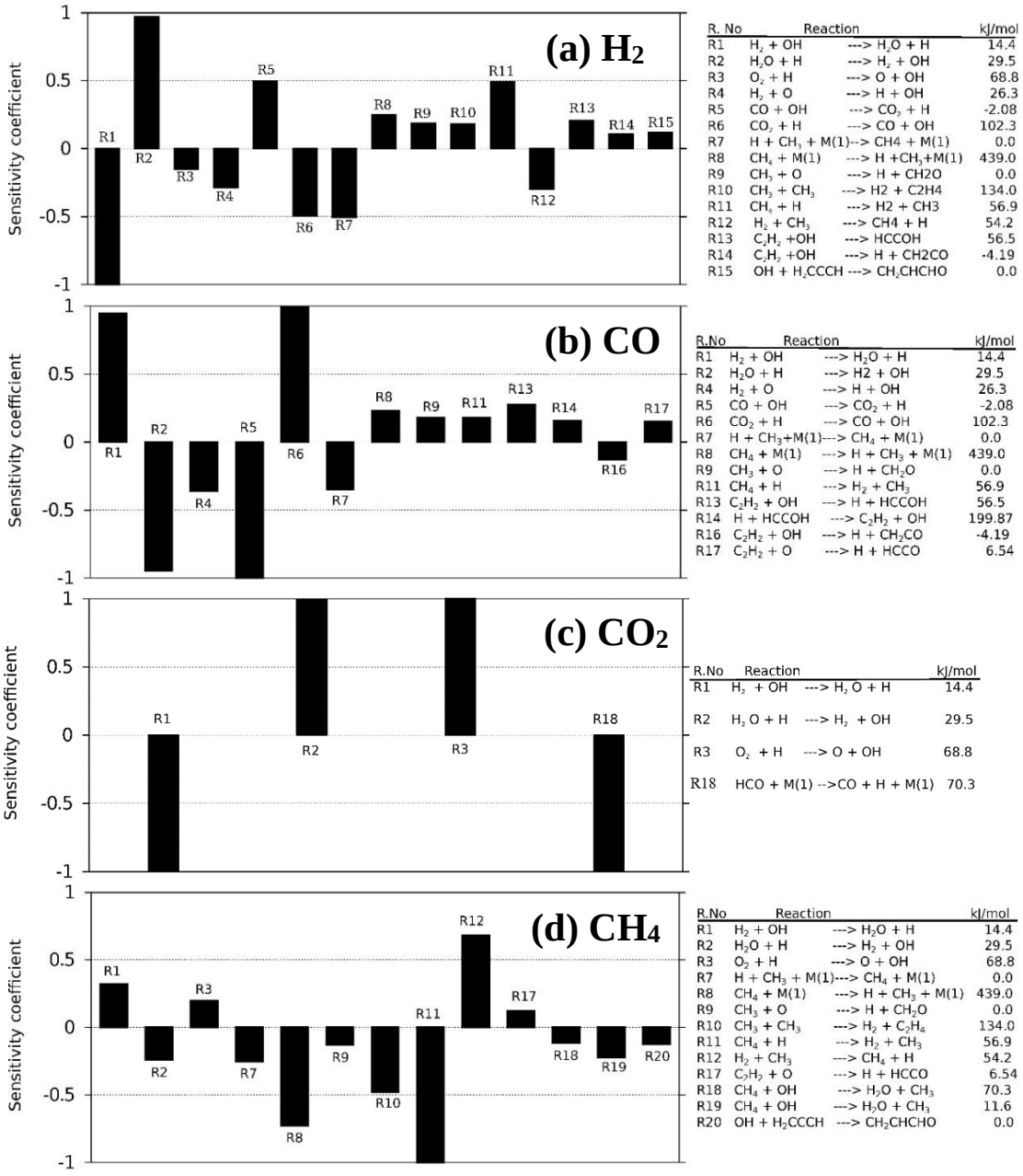

Fig. 3.8. Sensitivity analysis of the major gas phase species (a) H_2, (b) CO, (c) CO_2, and (d) CH_4.

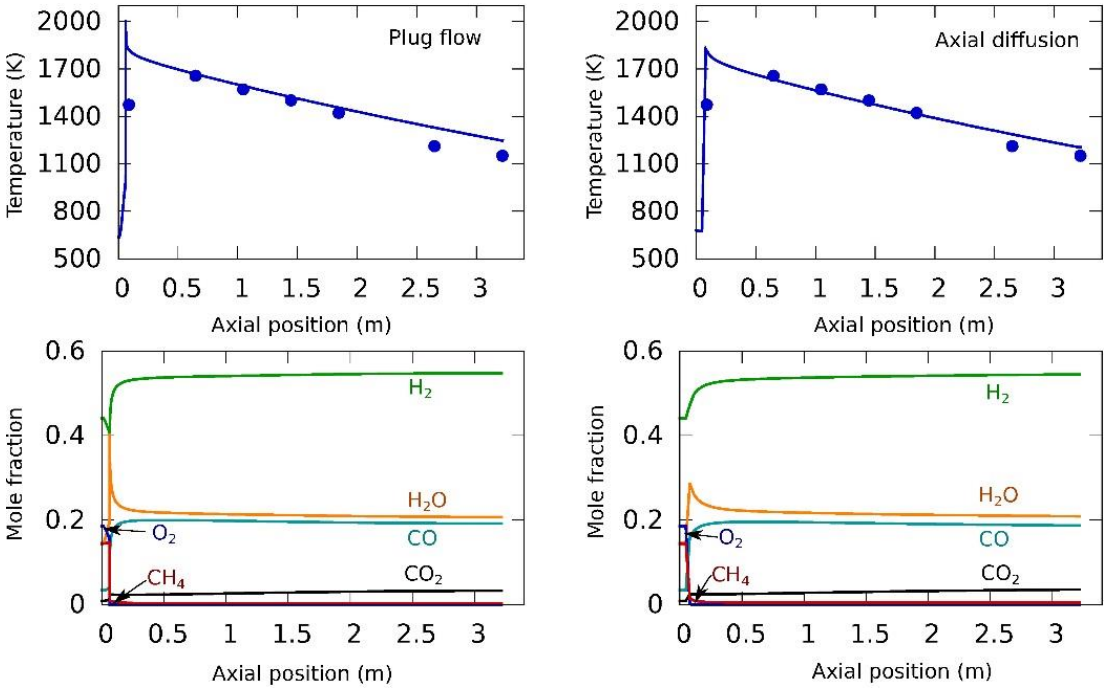

Fig. 3.9. Comparison of the temperature (top) and mole fraction (bottom) profiles without (left) and with (right) diffusional flow along the reactor axis during HCOG reforming with partial oxidation (run 11). The symbols indicate experimentally measured values, and the solid lines represent model predictions. The HCOG and O_2 flow rates are 62.9 Nm^3/h and 17.6 Nm^3/h, respectively.

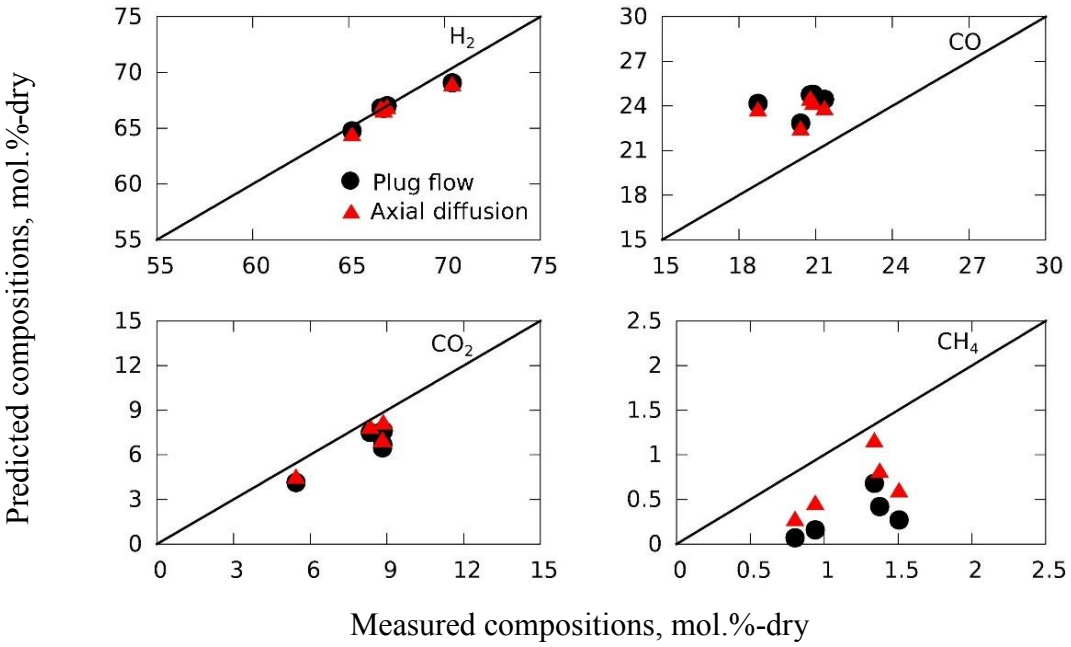

Fig. 3.10. Comparison of the reformed gas compositions predicted by the plug flow model and one dimensional flow with axial diffusion model with those measured by the pilot-scale tests for HCOG reforming with non-catalytic partial oxidation.

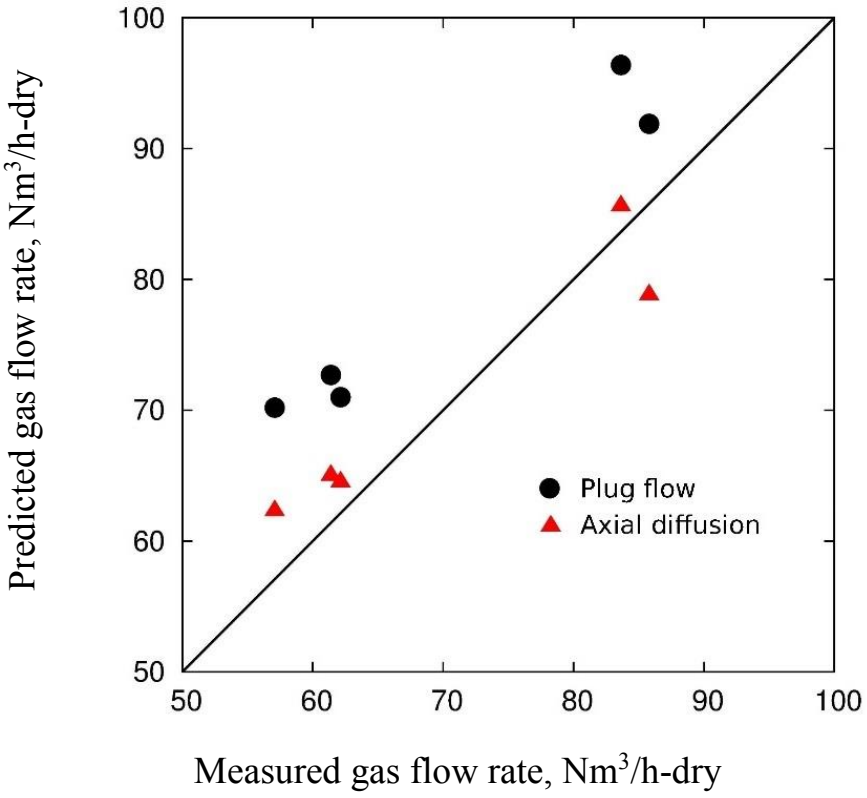

Fig. 3.11. Comparison of the reformed gas flow rates predicted by the plug flow model and one dimensional flow with axial diffusion model with those measured by the pilot-scale tests of HCOG reforming with non-catalytic partial oxidation.

Chapter 4

Non-catalytic reforming of coal gas containing tar using a CFD model coupled with reduced kinetic model

4.1. Introduction

Coke oven gas (COG) is a by-product in the metallurgical coke-making process and is emitted at 300–350 N m^3 per ton of coal [1]. The COG released from a coke oven is a multi-component gas mixture, containing primarily H_2 and methane and also carbon monoxide, carbon dioxide, and tarry compounds [2]. In a conventional coke-making process, the hot COG (HCOG) is quenched to recover the tar, which is distilled further to obtain marketable feedstocks for aromatic chemicals and pitch cokes. The tar-free COG is then also refined further through a desulphurisation facility and is used as a fuel for coke oven, town gas, and power stations [1,3].

The production of 'clean' gas, for example H_2 [4] and syngas [5], by reforming HCOG has been investigated to provide efficient use of the HCOG heat [4–18], which has been considered a promising alternative to the current established system of COG processing. HCOG reforming necessitates the conversion of the tarry compounds that comprise nearly 30 wt% of the crude COG and include aromatic compounds such as benzene, toluene, xylene, and polycyclic aromatic hydrocarbons (PAHs) [2,18].

Catalytic approaches to reforming HCOG using different oxidising agents such as steam, O_2, and CO_2 [6,11–14] have been reported. Deactivation of catalysts such as nickel [12,14,19] by sulphur poisoning due to H_2S included in the COG, as well as coking have been reported and are likely to be unavoidable to some degree [15,16].

Non-catalytic methods have also been studied, aiming at developing a more robust HCOG reforming technology [4,8–10]. Onozaki et al. [4] succeeded in reforming HCOG by a non-catalytic partial oxidation with a conversion rate of more than 98% on a carbon basis. Feasibility studies indicated that hydrogen can be produced at lower cost and higher efficiency by this technology than by the conventional methods, including the separation of tar and subsequent reforming of dry COG.

A deeper understanding of the chemistry and kinetics of HCOG reforming and fluid dynamics in the reformer is of great significance in designing reactors and optimising operations. A detailed chemical kinetic approach was thus used [17,18] to numerically simulate HCOG reforming experiments that were conducted with a bench-scale reformer installed on an operating coke oven. A kinetic model consisting of 2216 reactions with 257 species was used to predict the chemistries of HCOG reforming and was coupled with a plug-flow reactor model and a one-dimensional model based on flow with axial diffusion [20]. Although this approach showed satisfactory agreement between model predictions and measurements for the composition and flow rate of the HCOG reformation, the one-dimensional reactor model assumed premixing of HCOG with oxygen and neglected any effect of turbulence. In fact, the HCOG was reformed by mixing it with oxygen supplied from four nozzles near the reformer

inlet, and the Reynolds number of the fluid in the reforming tests, $Re = DU_g\rho_g / \mu_g$, was about 2940, where D is the diameter of the reactor near O_2 nozzle (0.196 m), U_g is the superficial gas velocity (2.4 m/s), ρ_g and μ_g are the density and viscosity of the gas (0.5 kg/m^3 and 8.0×10^{-5} Pa·s, respectively). Presently a demonstration scale reformer is being designed. In the reformer, around 2500 Nm^3/h of the HCOG released from 5 coke oven chambers will be reformed to produce syngas. In predicting the HCOG reforming at this scale, more realistic flow model considering turbulence is obviously required. This is our motivation to develop the CFD approach in the present study. The CFD model coupled with elementary reactions should have greater advantages for reactor design and scaling-up the process compared with one dimensional model.

The reacting flow, as observed in a non-premixed partial oxidation of HCOG, is more realistically modelled when a detailed chemical kinetic model is used in multi-dimensional computational fluid dynamics (CFD). There are several methods to couple the chemistry with the turbulence ('turbulence–chemistry interactions'), such as the eddy dissipation/finite rate (ED/FR) model and the eddy dissipation concept (EDC). Fast chemistry approaches are not considered because HCOG reforming is recognized to require finite-rate chemistry models.

In the ED/FR model, two rate terms are computed: an Arrhenius rate based on the global chemistry mechanism, and a turbulent mixing rate based on the Magnussen–Hjertager expression. The smaller of the two rates is then chosen as the chemical source term in the species transport equations. However, the ED/FR model can only handle global kinetic mechanisms according to Arrhenius parameters, the turbulent rate being the same for all the reactions [21,22].

Therefore, the eddy dissipation concept (EDC) of Magnussen [23–25] has been used to take into account detailed chemistry and has been applied successfully in practical-scale reaction processes such as combustion [22–28], steam cracking [29], gasification [30], and NO_x and soot formation [21,31,32]. Both physical and chemical processes play an important role in simulating the real reactor systems and these processes will not be decoupled [33]. EDC with detailed kinetic model is widely used to describe the performance of industrial reactors. The use of detailed kinetic models enables the deeper understanding of the complex chemical process systems. The EDC is used to treat the interactions between the turbulence and chemistry in flames. It is based on the reactor concept which identifies a reactor related to the fine structures in turbulence. The fine structures are responsible for the dissipation of turbulence energy into heat. Within these structures, the reactants are assumed to mix at molecular scale. Effects of finite-rate chemistry are taken into account by treating the fine structures as constant pressure and adiabatic homogeneous reactors described by a perfectly stirred reactor concept. The method of linkage of both the CFD and the reaction kinetics were described elsewhere [34,35]. Parente et al. [22] investigated and simulated a CH_4/CH_4–H_2 burner in a 'moderate or intense low-oxygen dilution' (MILD) combustion regime using EDC. The EDC with detailed chemistry provided results showing a more uniform distribution of temperature as well as the extension of the reaction zone to a large proportion of the available volume in the burner, as would be expected in a MILD combustion regime. Stefanidis et al. [29] also reported that EDC coupled with detailed reaction kinetics can successfully reproduce

flow, temperature, and concentration fields in the radiation sections of industrial-scale steam-cracking units. However, no reported study has examined reforming characteristics of multi-component fuels such as HCOG using EDC coupled with a detailed chemical kinetic model in CFD modelling.

In this study, a numerical simulation of bench-scale HCOG reforming by non-catalytic partial oxidation in a turbulent flow is presented. A reduced chemical kinetic model, developed from an existing detailed kinetic model [36], was used for the CFD modelling and was validated with the bench-scale HCOG reforming measurements. Turbulence–chemistry interactions were considered in the CFD modelling to reproduce and examine the profiles of major gas concentrations and temperatures in the HCOG reforming process using the EDC model. The *in situ* adaptive tabulation (ISAT) algorithm [37,38] was used to accelerate computations. Additionally, radiation heat transfer from the flame to the thermowell was examined to further correct some discrepancies relative to CFD modelling. Finally, the CFD model was evaluated critically by comparisons with measured results from the bench-scale HCOG reforming test, such as concentrations of H_2, CO, CO_2, and CH_4, and the total dry gas flow rate, as well as the axial temperature profile.

4.2. Bench Scale Test of HCOG Reforming

A bench-scale test plant for HCOG reforming by partial oxidation was installed on the platform of full-scale ovens at the Kitakyushu Coking Works of Nippon Coke & Engineering Co., Ltd., Japan [17,18]. The HCOG was collected from three coke chambers and introduced into the reformer at a flow rate 65 N m^3/h. Oxygen was also supplied from four nozzles. The total flow rate of oxygen was 18 N m^3/h. The reformer was operated at atmospheric pressure. Gas temperatures were measured with thermocouples inserted vertically at different positions in the reformer. The gas compositions at both the inlet and outlet of the reformer were measured using online gas chromatography, and condensing products such as water and tar were determined by offline sampling. Details of the bench-scale experiment procedures and results have been reported elsewhere [17,18,20].

4.3. Modelling Approach

An existing detailed chemical kinetic model was used to develop a reduced model. The detailed kinetic model was reduced with the help of batch-reactor mode [39]. Major gas species profiles in the detailed chemical kinetic model were used as a function of residence time for the development of a reduced kinetic model. The reduced kinetic model was then used in CFD modelling, and evaluated in comparison with data from the bench-scale HCOG reforming experiments. Additionally, a thermowell analysis was modelled to incorporate radiation effects on the measurement of gas phase temperature at near the entrance of the HCOG reformer.

4.3.1. Reduction of the Detailed Kinetic Model

A detailed kinetic model developed by Richer and Howard [36], which consisted of 2216 elementary irreversible reactions with 257 chemical species, from the smallest radicals (hydrogen radicals) to the largest molecule (coronene), was used to develop a reduced kinetic model with the HOMREA software [39]. HOMREA was designed for the computational

analysis of time-dependent homogeneous reaction systems. HCOG is a multi-component gaseous mixture including tarry components. The HCOG tar consists of a mixture of about 30 aromatic hydrocarbons, including benzene, toluene, and PAHs up to coronene; all of these components are considered inputs to the batch reactor simulations. The input composition for the batch reactor simulations with the detailed kinetic model is provided in **Table 4.1**. The numerical simulations were performed as a function of residence time at 1600 K and at 10^5 Pa. A reduced kinetic model was also developed step by step from the detailed kinetic mechanism, in which the major gas species profiles were considered and unimportant reactions were excluded from the reaction network based on sensitivity analysis. Finally, a greatly reduced mechanism was obtained, which showed similar characteristics to the detailed kinetic model. The input composition of the reduced kinetic model for the numerical simulations is provided in **Table 4.2**. The final reduced kinetic model has 410 elementary step-like reactions involving 47 chemical species. The reduced mechanism and thermodynamic polynomials for heats of formation, entropies, and heat capacities of chemical species are provided in the **Appendix A.II**.

4.3.2. Geometry of HCOG Reformer

The geometry of the HCOG reformer, along with the O_2 nozzles, is shown in **Fig. 4.1**, which was based on the actual experimental scale. The HCOG reformer was characterised by a cylindrical section with 0.6 m inner diameter (i.d.) and had two ends, with an inlet and outlet inner diameters of 0.152 m and 0.20 m, respectively, and a total length of ca. 4.1 m. Four O_2 nozzles were configured for HCOG reforming by partial oxidation. These nozzles (i.d. ca. 0.04 m) were installed radially for perfect mixing at the entrance of the reformer. To reduce the computational cost, only a quarter computational geometry was considered, and the grid number of the computational mesh was 6170, which was provided in **Fig. 4.2**. A thermowell was also modelled to incorporate the effect of the radiation on thermocouple measurements in CFD modelling, which can better capture the actual gas temperature at the entrance of the reformer.

4.3.3. Boundary Conditions

Boundary conditions for the CFD simulations are shown in **Table 4.3**. No heat losses for the reactor to the surrounding were considered and the wall of the reactor was assumed to an adiabatic wall in the CFD modelling.

4.3.4. CFD Modelling

Application of the detailed chemical kinetic model with turbulent chemistry is a challenging task for combustion systems [40] because the coupling is complex and computationally expensive. To understand the physical and chemical processes of HCOG reforming, the CFD model coupled with detailed chemistry was conducted. Additionally, it is capable of capturing the reforming features. In the CFD modelling, the reduced kinetic mechanism developed with a batch reactor model was imported into the model. The chemical species data, which were in the form of NASA polynomials for heats of formation, entropies, and heat capacities, were imported without modification [17,18,36,41]. Chemical reactions occur in small turbulent structures over the time scale and are governed by Arrhenius reaction rates; these were

considered perfectly stirred tank reactors at constant pressure [40]. A standard k-ε model was used in the CFD modelling to simulate the turbulent flow field due to its robustness and reasonable accuracy. The k-ε model is based on the assumptions that the flow is turbulent and that the effects of molecular viscosity are negligible [42]. Eddy dissipation concept models have been used successfully in various processes such as coal combustion and biomass pyrolysis [30,38,40], and have been integrated numerically using the ISAT algorithm. It is a powerful tool to reduce the computational time for detailed chemistry in CFD simulations. The EDC model is an extension of the eddy dissipation model to include detailed kinetic mechanisms in turbulent flows. ISAT is an *in situ*, unstructured, adaptive tabulation of the accessed region with control of retrieval errors [37]. To use the tabulation for a particular flow, it is sufficient to tabulate the accessed region that depends on many aspects of the flow including kinetics, transport process, and boundary conditions. Thus, the table is built up during the reactive flow calculation, and each entry in the table corresponds to a composition that occurs during the process calculation. This improves the chemistry calculations by two- or three-fold and also offers a significant reduction in run times. These methods have been used widely for gasification processes [30,38,40,43]. Additionally, the P-1 radiation model, widely used in the gasification process [40,44,45], was employed to calculate the flux of the radiation inside the reformer. The P-1 radiation model requires little CPU time and can be applied readily to various complex geometries.

The commercially available Computational Fluid Dynamics software ANSYS FLUENT 14.0 software package was employed in this study (ANSYS, Inc., USA). The SIMPLE algorithm was used for pressure–velocity coupling. Convective fluxes in all transport equations were discretised with a first-order upwind and momentum with a first-order scheme. A least-squares cell-based gradient method was used to evaluate the diffusive fluxes and velocity derivatives. The STANDARD interpolation scheme was used for calculating the cell-face pressures.

4.4. Results and Discussion

4.4.1. Reduction of the Detailed Kinetic Model

The major gas phase species composition as a function of residence time is shown in **Fig. 4.3**. The reduced kinetic model shows similar characteristics to the detailed kinetic model, and little disagreement is observed in the cases of the CO and CO_2 mole fractions. The mole fractions of CO and CO_2 predicted by the detailed kinetic model are slightly larger than those by reduced model. In the reduced model, we represented the tarry constituents not by a number of aromatic hydrocarbons but only by benzene. Benzene is more refractory than polycyclic aromatic hydrocarbons in terms of reactivity with oxygen and steam. This is likely to be the reason why the reduced model gave smaller CO and CO_2 production than the detailed model did. Even at a short residence time, O_2 is consumed completely by the hydrocarbons and hydrogen. The mole fractions of H_2, CO_2, and CO increase with residence time, whereas those of H_2O and CH_4 decrease. The decreasing trends of H_2O and CH_4 are due to the steam reforming [46]. The CO composition decreases initially and then increases. This may have been due to the reverse water gas shift reaction, which is favoured at higher temperatures. Overall, the reduced kinetic model shows quantitatively similar characteristics to the original detailed kinetic model.

4.4.2. CFD Model Predictions

The fluid streamlines and temperature contours predicted in the numerical simulation during the HCOG reforming by partial oxidation are shown in **Fig. 4.4**. To promote the proper mixing of HCOG with O_2, four O_2 inlet nozzles installed at an angle of 30 °at the entrance of the HCOG reformer are visualised by the swirling streamlines in the figure. The swirl number of gas flow near the ignition zone was estimated to be around 0.3. The HCOG entered into the reformer at a temperature of 639 K and a velocity of 2.32 m/s. After the HCOG mixing with O_2 at the entrance of the reactor, the exothermic partial oxidation reaction was initiated and induced a sudden rise in temperature throughout the whole reformer. Hot-spot formations were observed at the exits of the O_2 nozzles. These hot spots indicate that most of the O_2 was consumed almost completely by the hydrocarbons and H_2 near the nozzle outlet. The subsequent gradual decrease in temperature is mainly due to endothermic methane steam reforming. The reduction in temperature along with the length of reactor indicated that the endothermic steam reforming reaction dominated after the depletion of oxygen.

Model predictions with corresponding radial and axial temperature measurements in the bench-scale reformer test are shown in **Fig. 4.5**. The CFD model well captured the temperature profiles of the reformer; however, a large difference was observed at the first thermocouple location, which was placed at near the reactor inlet. The experimental observed temperature is 1426 K, whereas the model predicts a gas temperature of ~867 K. This large difference may be due to carbonaceous species deposited on the surface of the thermowell from the combustion of light hydrocarbons. The capability of the CFD approach solving RANS equations to handle the highly transient phenomena such as ignition and turbulent combustion is still not perfect, even though the reduced but elementary reaction based detailed chemical kinetic model was coupled. Therefore, the error of temperature measured by thermocouple should be explained by not only the effect of radiation from a hot flame but also by the limitation of the ability of the present approach. A study on a more sophisticated approach with large-eddy simulations (LES) and the flamelet model that permits a consideration of detailed chemical kinetic mechanisms and a state-of-the-art description of soot formation and oxidation processes is now in progress, and will support to identify a more realistic reason for the errors in estimating gas temperature near flame. The thermowell analysis of radiation heat transfer from flame to the thermowell was not included in the CFD model, which is discussed in further detail in the next section. Overall, the temperature predictions are in good agreement with the experimental observed temperatures.

Mole fraction contours of O_2, CH_4, C_6H_6, and H_2O in the CFD modelling are shown in **Fig. 4.6**. The O_2 concentration is highest at the nozzle location and the major portion is consumed at the mixing location of the HCOG and O_2. This indicates that exothermic partial oxidation and H_2 combustion reactions took place near the nozzle, inducing sudden increases in temperature, which are also evident in **Fig. 4.5**. The mole fraction of CH_4 decreases from the inlet to the exit of the reactor, thus indicating that CH_4 initially participated in the partial oxidation near the reactor inlet, and only later participated in the reforming process with steam. A similar type of behaviour is also observed for C_6H_6. The H_2O concentration is the highest at nozzle locations and then decreases along the length of the reactor. The decreasing trend in H_2O is due mainly

to the CH_4 reforming reaction. As a whole, the entire reaction zone of the reactor is divided into two zones. The first zone corresponds to the partial oxidation and the second indicates the reforming zone.

Mole fraction contours of H_2, CO, and CO_2 are shown in **Fig. 4.7**. The H_2 contours show zero mass fraction at the O_2 nozzle outlets, although it later increased gradually. The lowest concentration of H_2 at the nozzles is due to complete H_2 combustion, and the further gradual increase in the H_2 mole fraction is due mainly to the CH_4 and tar compounds being steam-reformed. The mole fraction contours of CO increases gradually from the reactor inlet towards the reactor exit. The increase in the CO mole fraction is due mainly to CH_4 steam reforming. The decrease in CO_2 mole fraction may have been due to the reverse water gas shift reaction, which is favoured at higher temperatures.

A comparison between the model predictions and experimental results of major gas phase species of HCOG reforming by partial oxidation is shown in **Fig. 4.8**. The CFD model excellently captured the exit mole fractions of the major gas phase species. For example, the measured mole fraction of H_2 is 66 and the numerically predicted value is 62. The mole fractions of CO and CH_4 are slightly overpredicted, whereas that of CO_2 is slightly underpredicted. Additionally, the model shows good agreement with the total dry gas flow rate. The CFD model predicts the total flow rate to be 68 N m^3 dry gas/h, whilst the experimentally observed value is 73 N m^3 dry gas/h. The slight difference may be due to the simplified reduced kinetic model and/or slightly underpredicted temperatures. Overall, the CFD model is in good agreement with the major gas phase species compositions and total dry gas flow rates in the bench-scale HCOG reforming process.

4.4.3. Radiative Heat Transfer Effect on the Thermocouple Heating

A large deviation was observed between the predicted and measured temperatures at the first thermocouple location (**Fig. 4.5**), which was at near the reactor inlet. To compensate for this effect, radiative heat transfer towards the thermowell was also included in the CFD model. During the HCOG reforming by partial oxidation, carbon species may be deposited on the surface of the thermowell [47,48]. This may lead to a difference in the predicted and measured temperatures due to radiation effects. An alumina thermowell material was considered in the model; the physical properties of alumina are provided in **Table 4.4**. The surface of the thermowell was assumed to be opaque to thermal radiation, so that emissivity was needed and fixed in the analysis. In the present model, the emissivity values of 0.21 and 0.96 were fixed for alumina and carbon, respectively. Thermowell geometry along with a small portion of the reactor is provided in **Fig. 4.9**. Because of the 'coupled' wall between gas-phase flow and the thermocouple, the convective heat transfer was calculated by the solver directly from the solution in the adjacent cells [35,49]. To reduce the computational load, only a small portion of the reformer with the thermowell was considered for the analysis, and it had a total grid number of 28973.

Fig. 4.10 shows the fluid streamlines and temperature contours in the case of considering the thermowell in the numerical analysis. A high-temperature field is observed in the thermocouple region, shown on the right side of the figure. The experimental temperature of the first

thermocouple location, which was placed at near the reactor inlet, is 1426 K (**Fig. 4.5**). The numerical analysis in **Fig. 4.10** indicates that the thermocouple temperatures are ~1150 K and ~1410 K for alumina and carbon, respectively. Thus, a thermowell that is assumed to be coated with carbon and to exhibit emissivity of 0.96 shows better agreement between the predicted and measured temperatures observed at near the reactor inlet. The predicted temperature is 1410 K, which is close to the measured temperature of 1426 K. The surrounding gas temperatures nearer to the thermocouple, however, are 860 K for alumina and 863 K for carbon material. These results indicate that radiation heat transfer was very significant for the temperature measurement near the inlet of the HCOG reformer, likely caused by deposition of carbon on the surface of the thermowell. The thermocouple likely measured not the gas temperature but the temperature of the thermowell, which was not shielded from incoming radiation.

4.5. Conclusions

In this paper, bench-scale hot coke oven gas reforming by partial oxidation was investigated numerically in a three-dimensional CFD model. Due to present software restrictions for handling detailed kinetic models, a reduced kinetic model developed from a detailed kinetic model was used in the CFD analysis of HCOG reforming. Unimportant radical reactions, which did not contribute much in calculating the major product gas phase species concentrations were identified based on a sensitivity analysis, and were excluded with the help of a batch reactor model. Finally, a greatly reduced model was obtained that showed similar characteristics to the detailed kinetic model. The reduced kinetic model had a total of 410 reactions with 47 chemical species. An eddy dissipation concept model integrated with the *in situ* adaptive tabulation (ISAT) algorithm was used in the CFD modelling to validate the data of the bench-scale HCOG reforming. The CFD model predictions were in good agreement with temperature profiles of the HCOG reformer and the major gas phase compositions. Additionally, the predicted total gas flow rate in the model was the same as the overall outlet gas flow rate of the bench-scale HCOG reforming test. Thermowell analysis was also considered in the CFD model to incorporate the radiation effect on thermocouple measurements. The predicted temperature of a carbon-coated thermowell with an emissivity of 0.96 was 1410 K, which is close to the measured temperature of 1426 K at the first thermocouple location, which was placed at near the reactor inlet. Overall, the CFD model, coupled with the reduced kinetic model, showed excellent agreement between the model predictions and experimental observations in the bench-scale reformer.

4.6. References

[1] Aramaki T. Status of the coke oven gas in Japan. J Japan Inst Energy 2006;85:342–7.

[2] Kirton PJ, Ellis J, Crisp PT. The analysis of organic matter in coke oven emissions. Fuel 1991;70:1383–9.

[3] Razzaq R, Li C, Zhang S. Coke oven gas: Availability, properties, purification, and utilization in China. Fuel 2013;113:287–99.

[4] Onozaki M, Watanabe K, Hashimoto T, Saegusa H, Katayama Y. Hydrogen production by the partial oxidation and steam reforming of tar from hot coke oven gas. Fuel 2006;85:143–9.

[5] Yang Z, Zhang Y, Wang X, Ding W. Design of two-stage membrane reactor for the conversion of coke-oven gas to H_2 and CO. J Energy Chem 2014;23:411–3.

[6] Jess A. Catalytic upgrading of tarry fuel gases: A kinetic study with model components. Chem Eng Process Process Intensif 1996;35:487–94.

[7] Jess A. Herstellung von reduktionsgas aus koksofenrohgas. Stahl Und Eisen 1995;115:115–21.

[8] Jess A. Mechanisms and kinetics of thermal reactions of aromatic hydrocarbons from pyrolysis of solid fuels. Fuel 1996;75:1441–8.

[9] Miura K, Kawase M, Nakagawa H, Ashida R, Nakai T, Ishikawa T. Conversion of tar in hot coke oven gas by pyrolysis and steam reforming. J Chem Eng Japan 2003;36:735–41.

[10] Hashimoto T, Onozaki M. Reforming of hot coke oven gas. J Japan Inst Energy 2006;85:364–70.

[11] Guo J, Hou Z, Gao J, Zheng X. Production of syngas via partial oxidation and CO_2 reforming of coke oven gas over a Ni catalyst. Energy & Fuels 2008;22:1444–8.

[12] Cheng H, Yue B, Wang X, Lu X, Ding W. Hydrogen production from simulated hot coke oven gas by catalytic reforming over Ni/Mg(Al)O catalysts. J Nat Gas Chem 2009;18:225–31.

[13] Cheng H, Lu X, Zhang Y, Ding W. Hydrogen production by reforming of simulated hot coke oven gas over nickel catalysts promoted with lanthanum and cerium in a membrane reactor. Energy & Fuels 2009;23:3119–25.

[14] Cheng H, Lu X, Liu X, Zhang Y, Ding W. Partial oxidation of simulated hot coke oven gas to syngas over Ru-Ni/Mg(Al)O catalyst in a ceramic membrane reactor. J Nat Gas Chem 2009;18:467–73.

[15] Hepola J, Simell P. Sulphur poisoning of nickel-based hot gas cleaning catalysts in synthetic gasification gas. II. Chemisorption of hydrogen sulphide. Appl Catal B Environ 1997;14:305–21.

[16] Depner H, Jess A. Kinetics of nickel-catalyzed purification of tarry fuel gases from gasification and pyrolysis of solid fuels. Fuel 1999;78:1369–77.

[17] Norinaga K, Hayashi J. Numerical simulation of the partial oxidation of hot coke oven gas with a detailed chemical kinetic model. Energy & Fuels 2010;24:165–72.

[18] Norinaga K, Yatabe H, Matsuoka M, Hayashi JI. Application of an existing detailed chemical kinetic model to a practical system of hot coke oven gas reforming by noncatalytic partial oxidation. Ind. Eng. Chem. Res., vol. 49, 2010, P.10565–71.

[19] Appari S, Janardhanan VM, Bauri R, Jayanti S. Deactivation and regeneration of Ni catalyst during steam reforming of model biogas: An experimental investigation. Int J Hydrogen Energy 2014;39:297–304.

[20] Appari S, Tanaka R, Li C, Kudo S, Hayashi J, Janardhanan VM, et al. Predicting the temperature and reactant concentration profiles of reacting flow in the partial oxidation of hot coke oven gas using detailed chemistry and a one-dimensional flow model. Chem Eng J 2015;266:82–90.

[21] Galletti C, Parente A, Derudi M, Rota R, Tognotti L. Numerical and experimental analysis of NO emissions from a lab-scale burner fed with hydrogen-enriched fuels and operating in MILD combustion. Int J Hydrogen Energy 2009;34:8339–51.

[22] Parente A, Galletti C, Tognotti L. Effect of the combustion model and kinetic mechanism on the MILD combustion in an industrial burner fed with hydrogen enriched fuels. Int J Hydrogen Energy 2008;33:7553–64.

[23] Magnussen BF. On the structure of turbulence and a generalized eddy dissipation concept for chemical reaction in turbulent flow. 19th Am. Inst. Aeronaut. Astronaut. Aerosp. Sci. Meet., St. Louis, Missouri, USA: 1981.

[24] Gran IR, Ertesvag IS, Magnussen BF. Influence of turbulence modeling on predictions of turbulent combustion. AIAA J 1997;35:106–10.

[25] Magnussen BF. The eddy dissipation concept: A bridge between science and technology. ECCOMAS Themat. Conf. Comput. Combust., Lisbon, Portugal: 2005.

[26] Bilger RW. Future progress in turbulent combustion research. Prog Energy Combust Sci 2000;26:367–80.

[27] Lilleberg B, Christ D, Ertesvåg IS, Rian KE, Kneer R. Numerical simulation with an extinction database for use with the eddy dissipation concept for turbulent combustion flow, Turbul Combust 2013;91:319–46.

[28] Magel HC, Schnell U, Hein KRG. Simulation of detailed chemistry in a turbulent combustor flow. Symp Combust 1996;26:67–74.

[29] Stefanidis GD, Merci B, Heynderickx GJ, Marin GB. CFD simulations of steam cracking furnaces using detailed combustion mechanisms. Comput Chem Eng 2006;30:635–49.

[30] Rehm M, Seifert P, Meyer B. Theoretical and numerical investigation on the EDC-model for turbulence–chemistry interaction at gasification conditions. Comput Chem Eng 2009;33:402–7.

[31] Scharler R, Widmann E, Obernberger I. CFD modelling of NOx formation in biomass grate furnaces with detailed chemistry. 6th Int. Conf. Sci. Therm. Chem. Biomass Convers., Victoria, Vancouver Island, BC, Canada: 2004.

[32] Magnussen BF. Modeling of pollutant formation in gas turbine combustors based on the eddy dissipation concept. 18th Int. Congr. Combust. Engines, Int. Counc. Combust. Engines, Tianjin, PRC: 1989.

[33] Warnatz J, Maas U, Dibble RW. Combustion: Physical and chemical fundamentals, modeling and simulation, experiments, pollutant formation. 3rd ed. Springer-Verlag, Berlin Heidelberg GmbH; 2001.

[34] Gran IR, Magnussen BF. A numerical study of a bluff-body stabilized diffusion flame. Part 2. Influence of combustion modeling and finite-rate chemistry. Combust Sci Technol 1996;119:191–217.

[35] ANSYS FLUENT theory guide. ANSYS, InC; 2011.

[36] Richter H, Howard JB. Formation and consumption of single-ring aromatic hydrocarbons and their precursors in premixed acetylene, ethylene and benzene flames electronic supplementary information (ESI) available: Thermodynamic and kinetic property data. Phys Chem Chem Phys 2002;4:2038–55.

[37] Pope SB. Computationally efficient implementation of combustion chemistry using in situ adaptive tabulation. Combust Theory Model 1997;1:41–63.

[38] Rashidi A, Hafner S, Riedel U. Gasification of ethylene glycol as model substance for biomass based pyrolysis oil : Detailed reaction mechanism development and CFD simulation. Proc Eur Combust Meet 2009.

[39] Warnatz J, Mass U. HOMREA V2.5 2002.

[40] Vascellari M, Cau G. Influence of turbulence–chemical interaction on CFD pulverized coal MILD combustion modeling. Fuel 2012;101:90–101.

[41] Norinaga K, Deutschmann O. Detailed kinetic modeling of gas-phase reactions in the chemical vapor deposition of carbon from light hydrocarbons. Ind Eng Chem Res 2007;46:3547–57.

[42] Rashidi A. Inaugural - Dissertation CFD simulation of biomass gasification using detailed chemistry 2011.

[43] Gräbner M, Ogriseck S, Meyer B. Numerical simulation of coal gasification at circulating fluidised bed conditions. Fuel Process Technol 2007;88:948–58.

[44] Tang Y, Liu D, Liu Y, Luo Q. 3D computational fluid dynamics simulation of natural coke steam gasification in general and improved fluidized beds. Energy & Fuels 2010;24:5602–10.

[45] Xuan J, Leung MKH, Leung DYC, Ni M. Integrating chemical kinetics with CFD modeling for autothermal reforming of biogas. Int J Hydrogen Energy 2009;34:9076–86.

[46] Behnam M, Dixon AG, Wright PM, Nijemeisland M, Stitt EH. Comparison of CFD simulations to experiment under methane steam reforming reacting conditions. Chem Eng J 2012;207-208:690–700.

[47] Haynes BS, Wagner HG. Soot formation. Prog Energy Combust Sci 1981;7:229–73.

[48] Yilmaz N. Detailed multiphysics modeling and validation of thermocouple readings in fires. J Fire Sci 2011;29:443–64.

[49] ANSYS FLUENT user's guide. Release 14. ANSYS, InC; 2011.

Table Captions

Figure Captions

Table. 4.1. Inlet gas compositions for the batch reactor simulations with the detailed kinetic model.

Compound	Mole fraction
H_2	3.67E-01
CH_4	1.50E-01
C_2H_4	1.50E-02
C_2H_6	5.50E-03
CO	3.39E-02
CO_2	1.40E-02
N_2	1.71E-02
O_2	2.13E-01
H_2O	1.73E-01
benzene	3.52E-03
toluene	8.02E-04
Xylene	6.17E-05
styrene	2.29E-04
phenol	5.01E-04
Indene	6.58E-04
naphthalene	3.66E-03
2-methylnaphthalene	3.20E-04
1-methylnaphthalene	1.43E-04
acenaphthylene	2.52E-04
acenaphthene	5.15E-05
fluorine	1.58E-04
phenanthrene	5.14E-04
anthracene	1.29E-04
cyclopenta[def]phenanthrene	2.02E-05
2-phenylnaphthalene	9.39E-06
fluoranthene	2.07E-04
acephnanthrylene	8.13E-06
aceanthrylene	6.77E-06
Pyrene	1.42E-04
benzo[a]fluorine	1.14E-05
cyclopenta[cd]pyrene	3.63E-06
benz[a]anthracene	5.64E-05
chrysene	6.00E-05
benzo[b]fluoranthene	4.56E-05
benzo[e]pyrene	3.48E-05
benzo[a]pyrene	3.69E-05
perylene	9.77E-06
benzo[ghi]perylene	1.49E-05
anthanthrene	5.95E-06
coronene	1.82E-06

Table. 4.2. Inlet gas compositions for the batch reactor simulations with the reduced kinetic model.

Compound	Mole fraction
H_2	3.669E-01
CH_4	1.503E-01
C_2H_4	1.495E-02
C_2H_6	5.499E-03
CO	3.393E-03
CO_2	1.400E-02
N_2	3.700E-02
O_2	2.126E-01
H_2O	1.729E-01
C_6H_6	2.200E-02
C_6H_5OH	5.007E-04

Table. 4.3. Boundary conditions for the three-dimensional CFD model.

	HCOG inlet	O_2 inlet (nozzle)
Temperature (K)	639	300
Pressure (Pa)	10^5	10^5
Velocity (m/s)	2.32	0.94
Turbulent internsity (%)	5	5
Turbulent length scale (m)	1	1
Compositions (mole fraction %)		
O_2	-	1.0
H_2	4.680E-01	
CO	4.330E-02	
CO_2	1.790E-02	
H_2O	2.205E-01	
CH_4	1.917E-01	
C_2H_4	1.910E-02	
C_2H_6	7.000E-03	
C_6H_6	1.040E-02	
C_6H_5OH	4.000E-04	
N_2	2.180E-02	

Table. 4.4. Physical properties of the thermowell.

Main component, %	Al_2O_3, 99.7
Bulk density, kg/ m^3	3800
Heat conductivity, w/ m·K	17.9
Specific heat, J/ kg·K	900
Emissivity for alumina	0.21
Emissivity for carbon	0.96

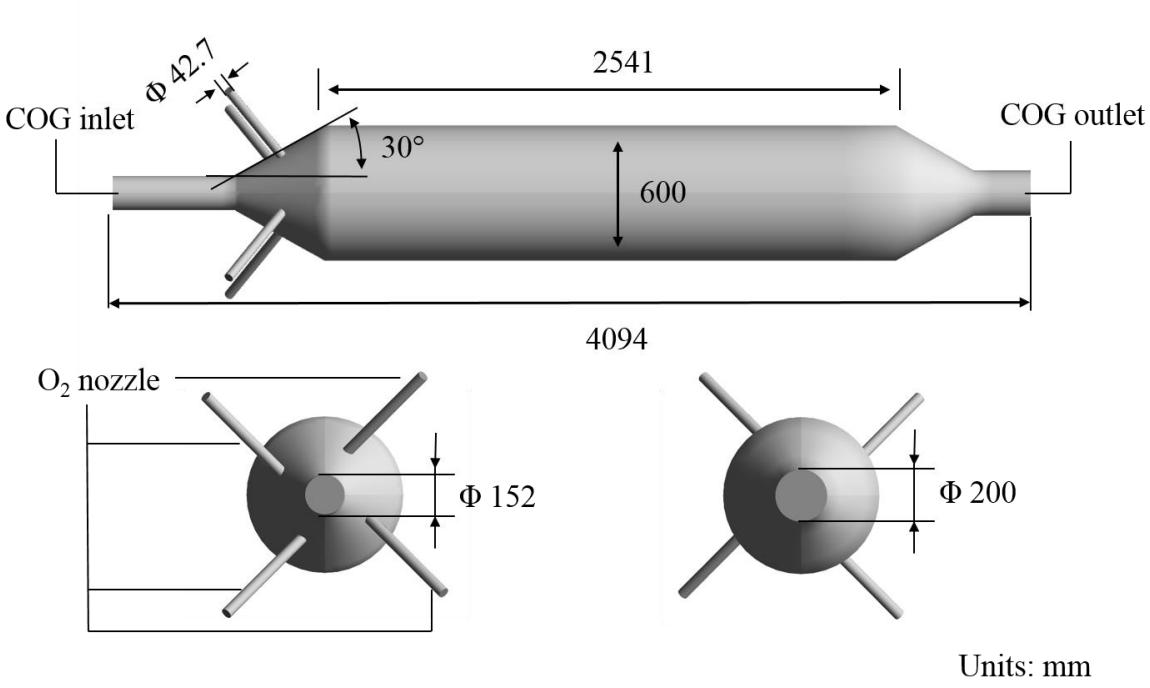

Fig. 4.1. Geometry of hot coke oven gas reformer along with O_2 nozzles.

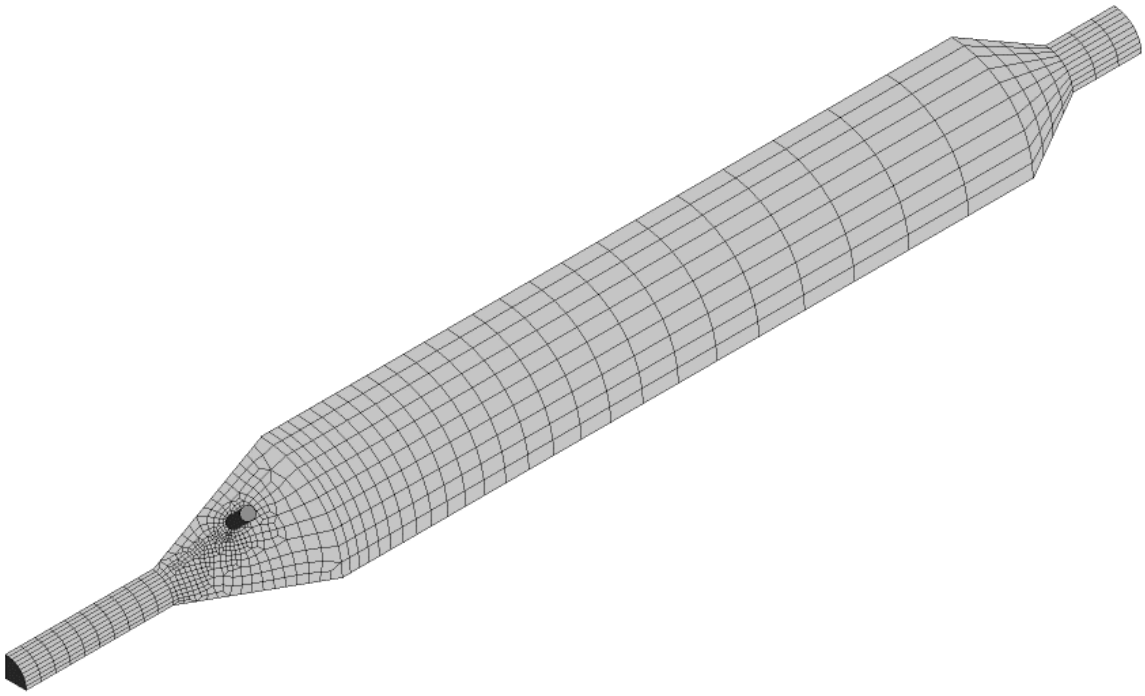

Fig. 4.2. One-fourth of computational grid for HCOG reformer.

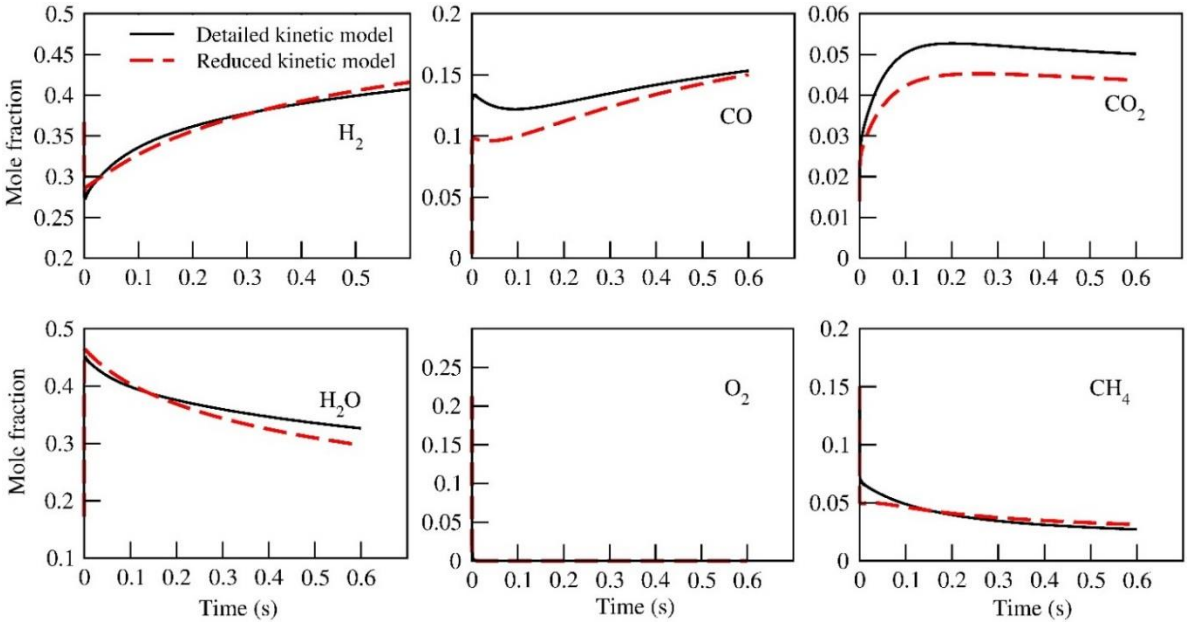

Fig. 4.3. Comparison between detailed and reduced kinetic model predictions for major species concentrations as a function of residence time. Solid and dashed lines represent the detailed and reduced kinetic models, respectively.

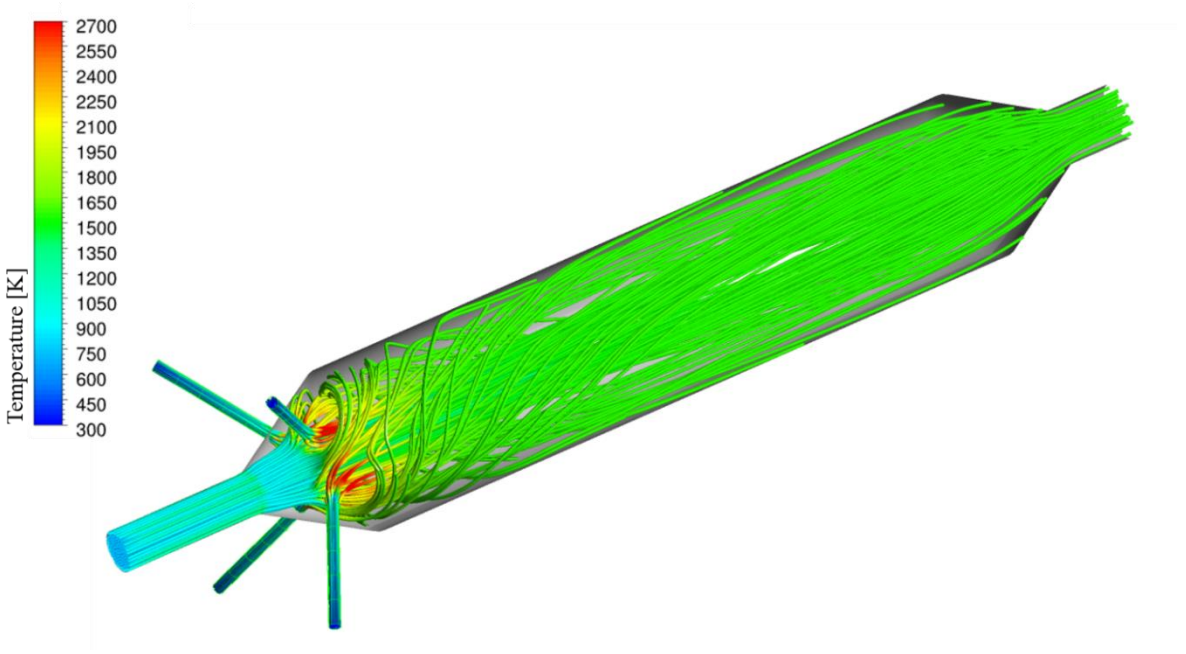

Fig. 4.4. Numerically simulated fluid streamlines and temperature contours inside the HCOG reformer.

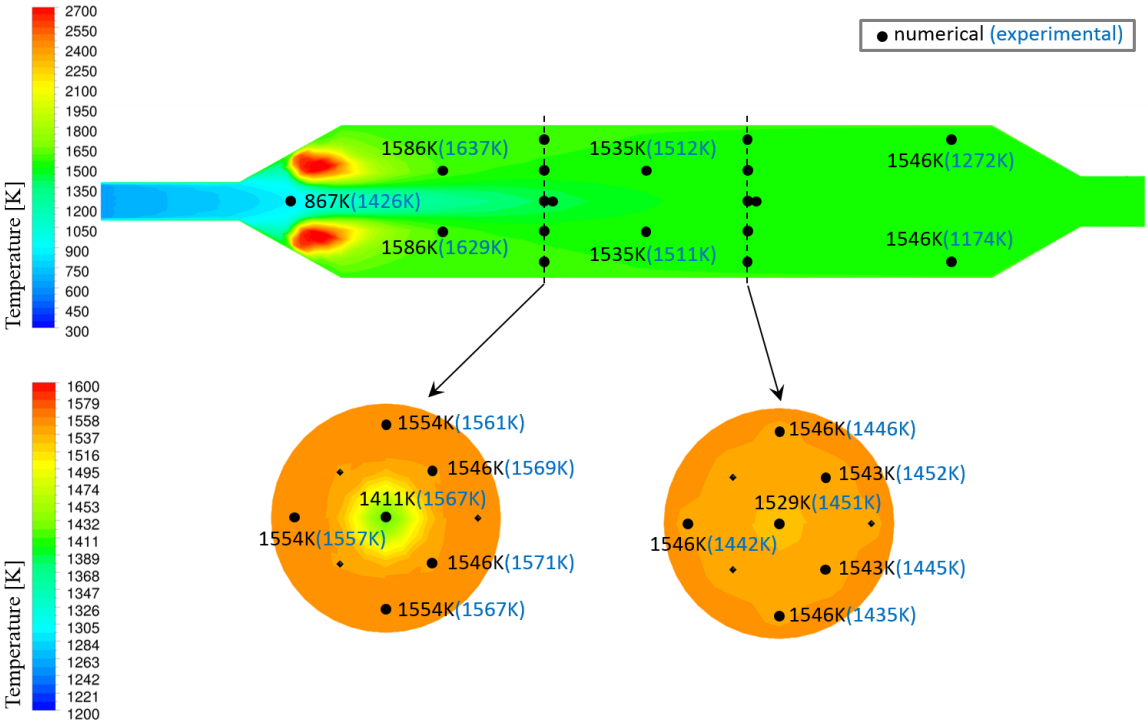

Fig. 4.5. Comparison between the numerical predictions and the corresponding radial and axial experimental temperature measurements in the HCOG reformer along with the position of thermocouples.

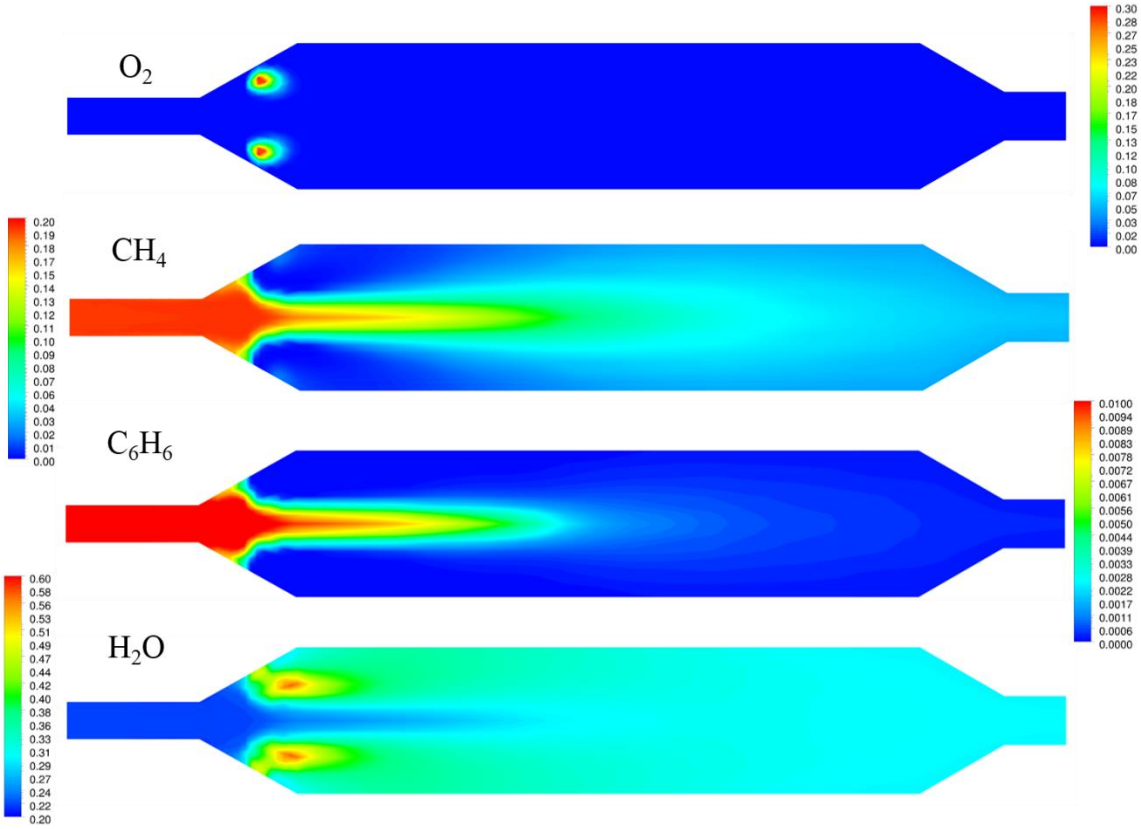

Fig. 4.6. Numerically simulated mole fraction contours for O_2, CH_4, C_6H_6, and H_2O inside the HCOG reformer.

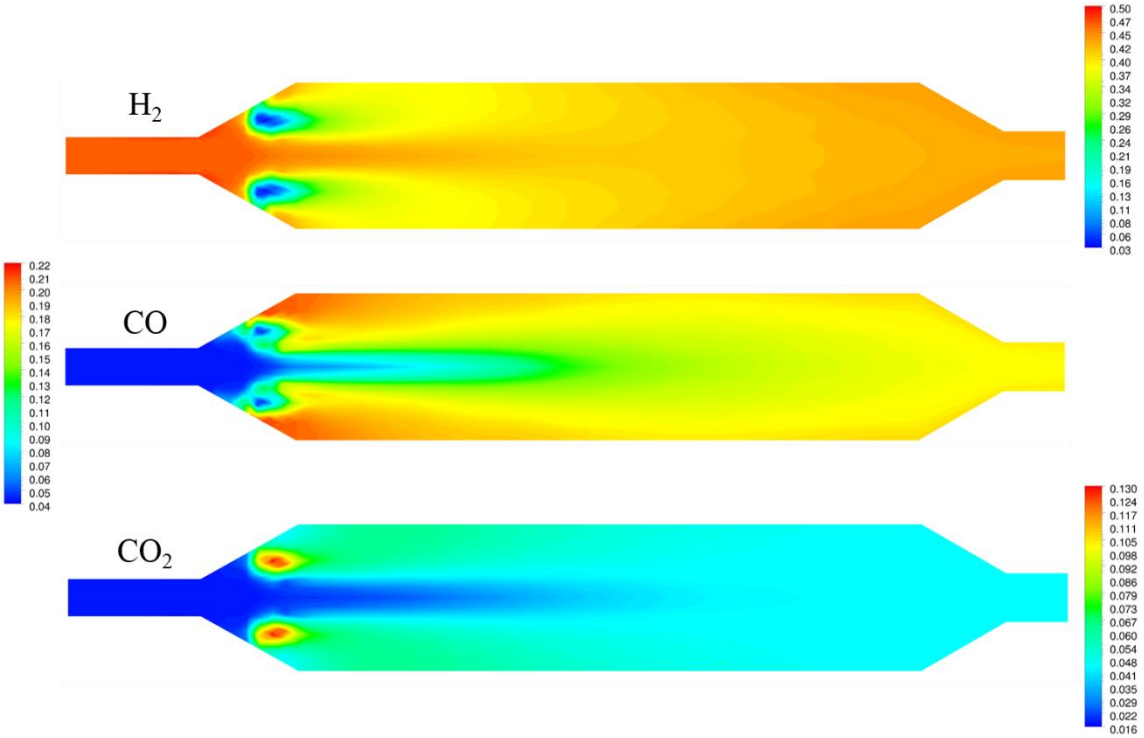

Fig. 4.7. Numerically simulated mole fraction contours for H_2, CO, and CO_2 inside the HCOG reformer.

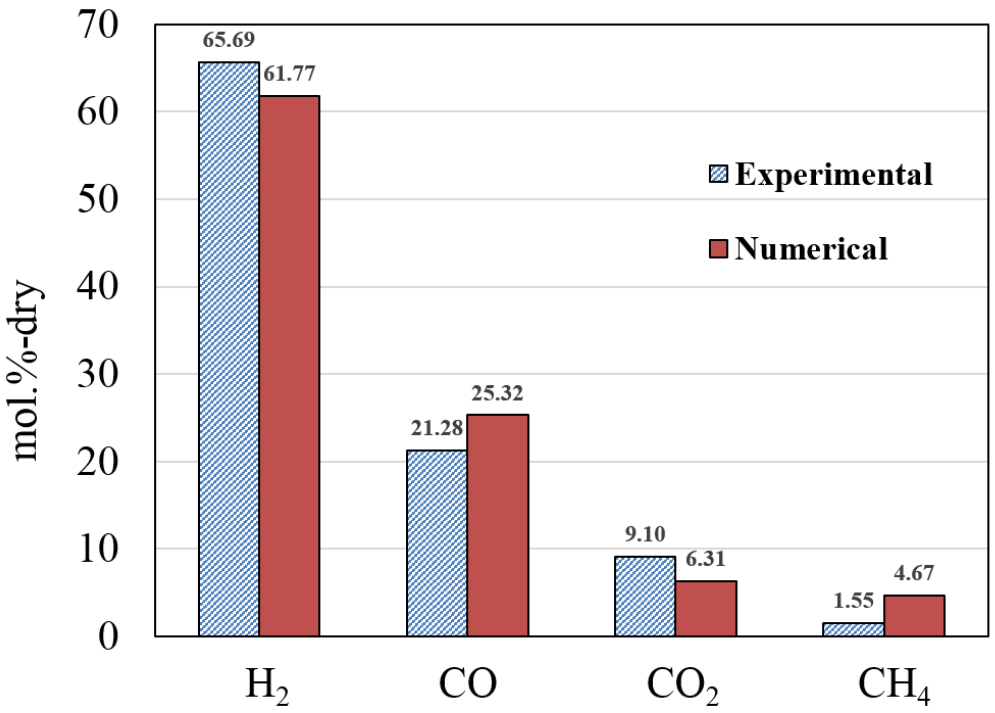

Fig. 4.8. Comparison between numerical predictions and experimental observations of major gas species compositions at exit of the HCOG reformer.

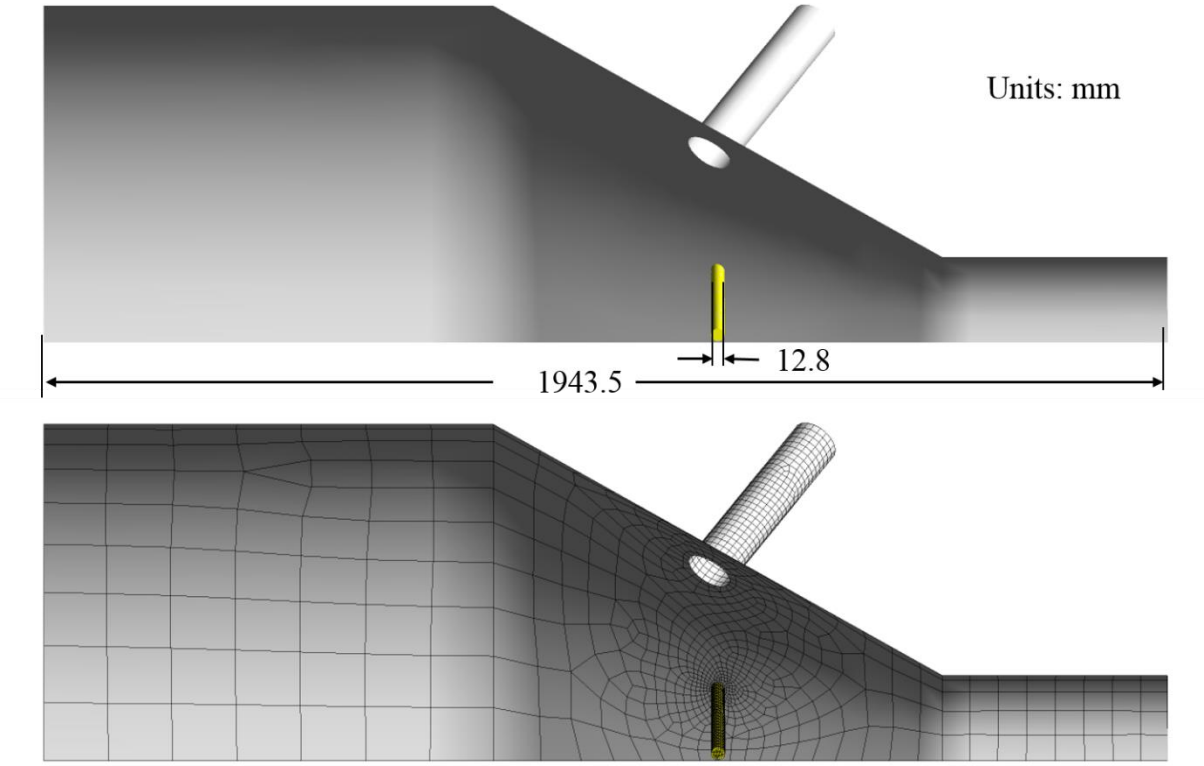

Fig. 4.9. One-fourth geometry and computational grid of thermocouple with the thermowell and O_2 nozzle.

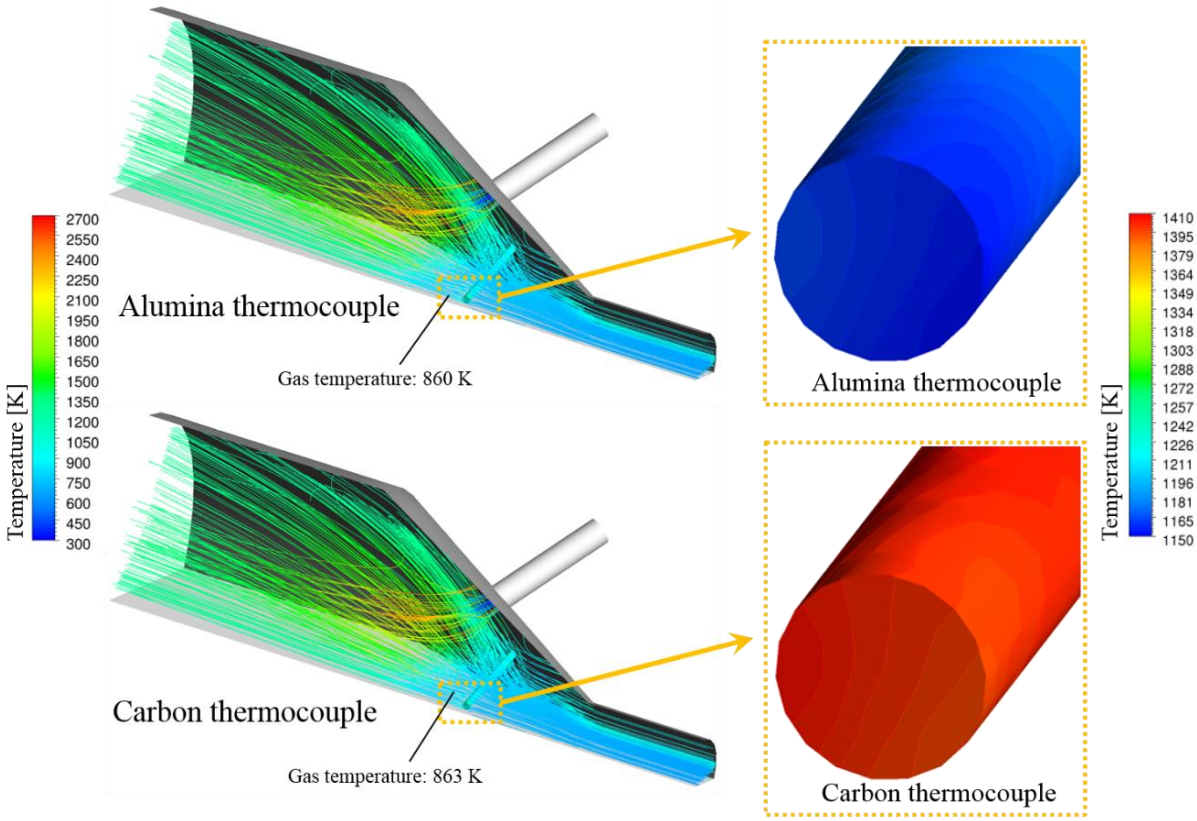

Fig. 4.10. The fluid streamlines and temperature contours inside the HCOG reformer after adding the thermowell.

Chapter 5

General conclusions

Coal is a major energy resource in the world. Coal conversion includes coal pyrolysis, char gasification and volatiles reforming. Chemical reactions in coal conversion are numerous and complex, including homogeneous and heterogeneous reactions. Kinetic models of reactions in coal conversion is of very significance to understand the chemistry and mechanism of coal conversion. CFD approach is a branch of fluid mechanics that using numerical methods and algorithms to solve and analyze problems that involve fluid flows, especially three dimensional (3D) numerical simulation. Therefore, CFD approach coupled with a kinetic model is a powerful tool that enables a better analysis and understanding of both fluid flow and reactions occurring in coal conversion process.

The conclusions achieved in this thesis are summarized as follow:

In **Chapter 2**, Victorian brown coal and char prepared from the same coal were co-fed into an atmospheric DTR. Loy Yang brown coal was converted in a DTR under conditions similar to those typically used in a downer reactor, where coal, char particles, and gas flow co-currently. The effects of reaction temperature (973–1173 K), solid hold-up (8.31×10^{-6}–2.50×10^{-4}), residence time (0–4.6 s for gas; 0–0.78 s for solid particles), and steam partial pressure (0–0.05 MPa) on the conversion characteristics were investigated. The temperature showed a significant influence on the rate of every process, and the product yields varied significantly with temperature. The solid hold-up mainly affected the tar-char interaction and tar was decomposed more extensively with increasing solid hold-up. The steam partial pressure only slightly affected the yields of tar, char, and carbon gases, but suppressed soot formation.

A 4-lump kinetic model consisting of tar, gases, char, and soot with 6 global reactions was developed based on the experimental results. The lumped kinetic model was integrated with a computational fluid dynamics (CFD) simulation using an Eulerian-Eulerian approach for mixed phase flow to simulate the coal conversion experiments in the DTR. The CFD results for product distribution during coal conversion in the DTR showed reasonable agreement with the experimental results. The CFD approach presented is suitable for use in designing and optimizing a pyrolyzer for a triple-bed combined circulating fluidized-bed coal gasifier, consisting of a downer (pyrolyzer), a bubbling fluidized bed (gasifier), and a riser (combustor).

In **Chapter 3**, a numerical approach is presented for predicting the species concentrations and temperature profiles of chemically reacting flow in the non-catalytic partial oxidation of hot coke oven gas (HCOG) in a pilot-scale reformer installed on an operating coke oven. A detailed chemical kinetic model consisting of 2216 reactions with 257 species ranging in size from the hydrogen radical to coronene was used to predict the chemistries of HCOG reforming. One-dimensional reactor models were developed that considered the heat loss from the reactor wall to the surroundings (plug flow) and axial diffusion, validated with pilot-scale HCOG reforming with partial oxidation measurements. In the plug flow simulations, an ignition temperature option was used initially to calculate the reaction rates, and then the reaction rates were

calculated using the gas-phase temperature. The overall heat transfer coefficient for heat losses from the reactor was optimised empirically at 4 $W/m^2 \cdot K$; with this value, the experimental axial temperature profiles of the HCOG pilot-scale runs were reproduced well. The HCOG was a multi-component gas mixture derived from coal dry distillation, and was approximated with more than 40 compounds: H_2, CO, CO_2, CH_4, C_2 hydrocarbons, H_2O, aromatic hydrocarbons such as benzene and toluene, and polycyclic aromatic hydrocarbons up to coronene. The measured gas temperature profiles were reproduced successfully by solving the energy balance equation accounting for the heat change induced by chemical reactions and heat losses to the surroundings. The approach was evaluated critically by comparing the computed results with experimental data for exit products such as H_2, CO, CO_2, and CH_4, in addition to the total exit gas flow rate. A global sensitivity analysis was used to identify the temperature-sensitive reactions. The axial diffusion model slightly improves the predictions of H_2, CO, and CO_2, but significantly improves those of CH_4 and total exit flow rate. The improvements in the model predictions were due primarily to the improved temperature predictions by accounting for axial diffusion in the flow model.

In **Chapter 4**, a computational fluid dynamics (CFD) approach to simulate reacting flow in a hot coke oven gas (HCOG) reformer is presented. The reforming of HCOG, a multi-component mixture, in a turbulent flow was simulated numerically by considering both chemical reactions and fluid dynamics. A reduced kinetic model developed from a detailed kinetic model, originally consisting of more than 2000 elementary reactions with 257 species, was reduced to 410 reactions with 47 species. Unimportant radical reactions, which did not contribute much in calculating the major product gas phase species concentrations were identified based on a sensitivity analysis, and were excluded with the help of a batch reactor model, because of present software restrictions for handling detailed kinetic models. The reduced kinetic model had a total of 410 reactions with 47 chemical species for realising a kinetic model of finite rate reactions with a k-ε turbulence model. Finally, a greatly reduced model was obtained that showed similar characteristics to the detailed kinetic model.

The calculation of a CFD approach was carried out using the eddy dissipation concept (EDC) coupled with the kinetic model, and accelerated using the *in situ* adaptive tabulation (ISAT) algorithm. A thermowell analysis was also considered in the CFD model to incorporate the radiation effect on thermocouple measurements. Overall, Numerical simulations could reproduce the reformed gas compositions fairly well, such as H_2, CO, CO_2, and CH_4, as well as the temperature profile in a HCOG reformer as measured by thermocouples.

Finally, here some perspectives are proposed for improving these studies as follow:

In **Chapter 2**, the effects of reaction temperature, solid hold-up, residence time and steam partial pressure on the conversion characteristics were investigated in the drop tube reactor, of which reaction environments are approximated in the industrial downer reactor. It shows that the solid hold-up, steam partial pressure, and reaction temperature affected the apparent rate constant, and the mathematical models between apparent rate constant and them were established. A gas/particle flow model with reactions in coal conversion was proposed in the presence of volatiles-char interaction by using a lumped kinetic model coupled with a CFD approach (Eulerian-Eulerian approach). To simplify the kinetic model, some necessary and

reasonable assumptions were made in the study. One important factor, the activity of catalyst, such as inherent AAEM species in the coal, was assumed to remain constant throughout the catalyst's life. That is, the total concentration of active sites on char surface accessible to the reactions in the presence of volatiles-char interaction does not change with time. Unfortunately, Mother Nature is not so kind as to allow behavior to be the case in the real and industrial coal gasification process. Therefore, the decay of catalyst due to coke or soot formation on its surface need be considered to further improve the modeling approach in the further study. What's more, in the real industrial downer reactor, the flow behaviors of the gas and solid phases are usually turbulence and the circulating mediums, such as silica sand, are used actually to heat the coal instead of the electric furnace. The gas-solid two-phase flow with turbulence-chemistry interaction and the mechanism of solid-to-solid phase heat transfer also need to be considered very carefully.

In **Chapter 3** and **Chapter 4**, hot coke oven gas (HCOG), as the representative multi-component coal-based fuels, was reformed by non-catalytic partial oxidation with oxygen in a tubular reactor, and its reforming process was simulated numerically by considering both chemical reactions and fluid dynamics. Advanced reacting flow models of HCOG reforming were proposed in the bench scale reformer by using 1D flow models (plug flow model and 1D axial diffusion model) and 3D flow model (k-ε turbulence model) coupled with detailed chemical kinetic model, respectively. One of important characteristics in HCOG steam reforming is a high complexity of reforming chemistry. In the study, the HCOG reforming was assumed as the gas phase homogeneous reaction in order to simplify the kinetic model. Some gas-solid reactions in the HCOG reforming were neglected, such as carbon deposition and soot formation mechanisms. If considering these reactions in the modeling, the predicted values will be more accurate, such as carbon species. What' more, the proposed modeling approaches for HCOG reforming need to be further verified at different experimental conditions.

Appendix

A.I Supplementary Information of Chapter 3

Composition of the feed HCOG for numerical simulations (all 19 runs).

Run No.	**1**	**2**	**3**	**4**	**5**	**6**	**7**
Inlet T, K	625.15	625.15	624.15	623.15	627.15	626.15	626.15
Velocity, m/s @inlet T	0.17439	0.17865	0.16738	0.16333	0.18022	0.18181	0.19243
Compounds	Mole fraction						
H2	3.99E-01	4.00E-01	3.98E-01	3.98E-01	3.51E-01	3.56E-01	3.44E-01
CH4	1.35E-01	1.40E-01	1.43E-01	1.48E-01	1.37E-01	1.32E-01	1.15E-01
C2H4	1.03E-02	1.04E-02	1.03E-02	1.04E-02	1.04E-02	9.93E-03	8.48E-03
C2H6	4.92E-03	5.03E-03	5.11E-03	5.17E-03	4.97E-03	4.75E-03	3.91E-03
CO	3.33E-02	3.38E-02	3.37E-02	3.37E-02	3.23E-02	3.17E-02	2.95E-02
CO2	1.20E-02	1.17E-02	1.15E-02	1.14E-02	1.26E-02	1.23E-02	1.09E-02
N2	1.75E-02	1.97E-02	2.07E-02	2.06E-02	1.36E-02	1.46E-02	1.97E-02
O2	1.94E-01	1.91E-01	1.97E-01	2.02E-01	1.84E-01	1.88E-01	1.72E-01
H2O	1.83E-01	1.77E-01	1.70E-01	1.61E-01	2.45E-01	2.43E-01	2.89E-01
benzene	3.26E-03	3.56E-03	3.70E-03	3.92E-03	3.18E-03	3.17E-03	2.95E-03
toluene	6.90E-04	6.99E-04	7.01E-04	7.06E-04	6.93E-04	6.90E-04	6.00E-04
xylene	6.27E-05	6.35E-05	6.38E-05	6.42E-05	5.77E-05	5.75E-05	5.46E-05
styrene	2.03E-04	2.00E-04	1.95E-04	1.84E-04	1.35E-04	1.35E-04	1.22E-04
phenol	4.44E-04	4.38E-04	4.26E-04	4.03E-04	2.95E-04	2.95E-04	2.67E-04
indene	5.84E-04	5.76E-04	5.61E-04	5.29E-04	3.88E-04	3.88E-04	3.51E-04
naphthalene	3.25E-03	3.20E-03	3.12E-03	2.94E-03	2.15E-03	2.16E-03	1.95E-03
2-methylnaphthalene	2.84E-04	2.80E-04	2.72E-04	2.57E-04	1.88E-04	1.89E-04	1.71E-04
1-methylnaphthalene	1.27E-04	1.25E-04	1.21E-04	1.15E-04	8.40E-05	8.41E-05	7.61E-05
acenaphthylene	2.24E-04	2.20E-04	2.15E-04	2.03E-04	1.48E-04	1.49E-04	1.35E-04
acenaphthene	4.57E-05	4.51E-05	4.39E-05	4.14E-05	3.03E-05	3.04E-05	2.75E-05
fluorine	1.40E-04	1.38E-04	1.35E-04	1.27E-04	9.32E-05	9.33E-05	8.44E-05
phenanthrene	4.56E-04	4.49E-04	4.37E-04	4.13E-04	3.02E-04	3.03E-04	2.74E-04
anthracene	1.15E-04	1.13E-04	1.10E-04	1.04E-04	7.60E-05	7.62E-05	6.89E-05
cyclopenta[def]phenanthrene	1.79E-05	1.76E-05	1.72E-05	1.62E-05	1.19E-05	1.19E-05	1.08E-05
2-phenylnaphthalene	8.33E-06	8.21E-06	8.00E-06	7.55E-06	5.53E-06	5.54E-06	5.01E-06
fluoranthene	1.84E-04	1.81E-04	1.77E-04	1.67E-04	1.22E-04	1.22E-04	1.11E-04
acephnanthrylene	7.21E-06	7.11E-06	6.92E-06	6.54E-06	4.79E-06	4.79E-06	4.34E-06
aceanthrylene	6.01E-06	5.92E-06	5.77E-06	5.45E-06	3.99E-06	3.99E-06	3.61E-06
pyrene	1.26E-04	1.24E-04	1.21E-04	1.14E-04	8.37E-05	8.39E-05	7.59E-05
benzo[a]fluorine	1.01E-05	9.97E-06	9.71E-06	9.17E-06	6.71E-06	6.72E-06	6.08E-06
cyclopenta[cd]pyrene	3.22E-06	3.18E-06	3.09E-06	2.92E-06	2.14E-06	2.14E-06	1.94E-06
benz[a]anthracene	5.01E-05	4.93E-05	4.80E-05	4.54E-05	3.32E-05	3.33E-05	3.01E-05
chrysene	5.33E-05	5.25E-05	5.11E-05	4.83E-05	3.53E-05	3.54E-05	3.20E-05
benzo[b]fluoranthene	4.05E-05	3.99E-05	3.88E-05	3.67E-05	2.69E-05	2.69E-05	2.43E-05
benzo[e]pyrene	3.08E-05	3.04E-05	2.96E-05	2.80E-05	2.05E-05	2.05E-05	1.85E-05
benzo[a]pyrene	3.28E-05	3.23E-05	3.14E-05	2.97E-05	2.17E-05	2.18E-05	1.97E-05
perylene	8.67E-06	8.55E-06	8.32E-06	7.86E-06	5.75E-06	5.76E-06	5.21E-06
benzo[ghi]perylene	1.32E-05	1.30E-05	1.27E-05	1.20E-05	8.76E-06	8.77E-06	7.93E-06
anthanthrene	5.28E-06	5.20E-06	5.07E-06	4.78E-06	3.50E-06	3.51E-06	3.17E-06
coronene	1.62E-06	1.60E-06	1.55E-06	1.47E-06	1.07E-06	1.08E-06	9.73E-07

Runs 8-14

Run No.	**8**	**9**	**10**	**11**	**12**	**13**	**14**
Inlet T, K	626.15	642.15	641.15	638.15	637.15	636.15	636.15
Velocity, m/s @inlet T	0.19088	0.23477	0.23054	0.21756	0.23205	0.20553	0.20121
Compounds	Mole fraction						
H2	3.45E-01	4.26E-01	4.19E-01	4.41E-01	3.16E-01	2.66E-01	2.53E-01
CH4	1.14E-01	1.30E-01	1.37E-01	1.44E-01	1.22E-01	1.57E-01	1.52E-01
C2H4	8.04E-03	7.99E-03	8.51E-03	7.26E-03	1.07E-02	1.29E-02	1.19E-02
C2H6	3.73E-03	2.67E-03	2.95E-03	2.60E-03	3.83E-03	4.12E-03	3.55E-03
CO	2.93E-02	3.34E-02	3.32E-02	3.37E-02	3.08E-02	3.46E-02	3.59E-02
CO2	1.06E-02	9.55E-03	1.13E-02	8.28E-03	1.16E-02	1.46E-02	1.48E-02
N2	2.08E-02	1.42E-02	1.45E-02	2.28E-02	2.08E-02	2.02E-02	3.56E-02
O2	1.68E-01	1.87E-01	1.92E-01	1.86E-01	1.74E-01	1.96E-01	1.99E-01
H2O	2.94E-01	1.78E-01	1.71E-01	1.46E-01	3.00E-01	2.83E-01	2.84E-01
benzene	2.95E-03	3.37E-03	3.52E-03	3.36E-03	3.01E-03	4.16E-03	4.18E-03
toluene	5.45E-04	5.09E-04	5.11E-04	4.03E-04	6.34E-04	7.28E-04	6.19E-04
xylene	5.45E-05	6.36E-05	6.39E-05	0.00E+00	5.28E-05	5.20E-05	5.16E-05
styrene	1.21E-04	2.01E-04	1.96E-04	1.47E-04	1.83E-04	1.79E-04	1.78E-04
phenol	2.65E-04	4.40E-04	4.30E-04	3.21E-04	4.01E-04	3.92E-04	3.89E-04
indene	3.49E-04	5.79E-04	5.65E-04	4.22E-04	5.27E-04	5.15E-04	5.11E-04
naphthalene	1.94E-03	3.22E-03	3.14E-03	2.35E-03	2.93E-03	2.86E-03	2.84E-03
2-methylnaphthalene	1.70E-04	2.81E-04	2.74E-04	2.05E-04	2.56E-04	2.50E-04	2.48E-04
1-methylnaphthalene	7.56E-05	1.25E-04	1.22E-04	9.15E-05	1.14E-04	1.12E-04	1.11E-04
acenaphthylene	1.34E-04	2.22E-04	2.16E-04	1.62E-04	2.02E-04	1.97E-04	1.96E-04
acenaphthene	2.73E-05	4.53E-05	4.42E-05	3.31E-05	4.12E-05	4.03E-05	4.00E-05
fluorine	8.39E-05	1.39E-04	1.36E-04	1.02E-04	1.27E-04	1.24E-04	1.23E-04
phenanthrene	2.72E-04	4.52E-04	4.40E-04	3.29E-04	4.11E-04	4.02E-04	3.99E-04
anthracene	6.84E-05	1.14E-04	1.11E-04	8.28E-05	1.03E-04	1.01E-04	1.00E-04
cyclopenta[def]phenanthrene	1.07E-05	1.77E-05	1.73E-05	1.29E-05	1.61E-05	1.58E-05	1.57E-05
2-phenylnaphthalene	4.98E-06	8.26E-06	8.05E-06	6.02E-06	7.51E-06	7.35E-06	7.29E-06
fluoranthene	1.10E-04	1.82E-04	1.78E-04	1.33E-04	1.66E-04	1.62E-04	1.61E-04
acephnanthrylene	4.31E-06	7.15E-06	6.97E-06	5.21E-06	6.50E-06	6.36E-06	6.31E-06
aceanthrylene	3.59E-06	5.96E-06	5.81E-06	4.34E-06	5.42E-06	5.30E-06	5.26E-06
pyrene	7.54E-05	1.25E-04	1.22E-04	9.12E-05	1.14E-04	1.11E-04	1.10E-04
benzo[a]fluorine	6.04E-06	1.00E-05	9.78E-06	7.31E-06	9.12E-06	8.92E-06	8.85E-06
cyclopenta[cd]pyrene	1.93E-06	3.20E-06	3.12E-06	2.33E-06	2.91E-06	2.84E-06	2.82E-06
benz[a]anthracene	2.99E-05	4.96E-05	4.84E-05	3.62E-05	4.51E-05	4.41E-05	4.38E-05
chrysene	3.18E-05	5.28E-05	5.15E-05	3.85E-05	4.80E-05	4.69E-05	4.66E-05
benzo[b]fluoranthene	2.42E-05	4.01E-05	3.91E-05	2.93E-05	3.65E-05	3.57E-05	3.54E-05
benzo[e]pyrene	1.84E-05	3.06E-05	2.98E-05	2.23E-05	2.78E-05	2.72E-05	2.70E-05
benzo[a]pyrene	1.96E-05	3.25E-05	3.17E-05	2.37E-05	2.95E-05	2.89E-05	2.87E-05
perylene	5.18E-06	8.60E-06	8.38E-06	6.27E-06	7.82E-06	7.65E-06	7.59E-06
benzo[ghi]perylene	7.88E-06	1.31E-05	1.28E-05	9.54E-06	1.19E-05	1.16E-05	1.16E-05
anthanthrene	3.15E-06	5.23E-06	5.10E-06	3.82E-06	4.76E-06	4.65E-06	4.62E-06
coronene	9.67E-07	1.60E-06	1.57E-06	1.17E-06	1.46E-06	1.43E-06	1.42E-06

Runs 15-19

Run No.	15	16	17	18	19
Inlet T, K	637.15	664.15	653.15	653.15	651.15
Velocity, m/s @inlet T	0.20985	0.21051	0.20735	0.20707	0.21747
Compounds	Mole fraction				
H2	2.70E-01	2.63E-01	3.05E-01	3.15E-01	3.42E-01
CH4	1.60E-01	1.74E-01	1.70E-01	1.62E-01	1.49E-01
C2H4	1.26E-02	1.27E-02	1.06E-02	1.12E-02	9.94E-03
C2H6	4.21E-03	4.01E-03	3.26E-03	3.41E-03	3.15E-03
CO	3.48E-02	3.12E-02	3.29E-02	3.30E-02	3.26E-02
CO2	1.40E-02	1.24E-02	1.21E-02	1.23E-02	1.13E-02
N2	1.90E-02	9.45E-03	9.37E-03	1.02E-02	9.99E-03
O2	1.91E-01	2.21E-01	2.14E-01	2.15E-01	2.04E-01
H2O	2.84E-01	2.55E-01	2.29E-01	2.25E-01	2.26E-01
benzene	4.34E-03	4.85E-03	4.51E-03	4.14E-03	3.76E-03
toluene	5.76E-04	7.30E-04	6.68E-04	5.60E-04	5.70E-04
xylene	5.23E-05	5.21E-05	5.57E-05	5.60E-05	5.70E-05
styrene	1.80E-04	3.24E-04	2.52E-04	2.56E-04	2.64E-04
phenol	3.95E-04	7.09E-04	5.52E-04	5.60E-04	5.77E-04
indene	5.19E-04	9.33E-04	7.25E-04	7.36E-04	7.58E-04
naphthalene	2.88E-03	5.18E-03	4.03E-03	4.09E-03	4.21E-03
2-methylnaphthalene	2.52E-04	4.53E-04	3.53E-04	3.58E-04	3.68E-04
1-methylnaphthalene	1.12E-04	2.02E-04	1.57E-04	1.60E-04	1.64E-04
acenaphthylene	1.99E-04	3.57E-04	2.78E-04	2.82E-04	2.90E-04
acenaphthene	4.06E-05	7.30E-05	5.68E-05	5.76E-05	5.94E-05
fluorine	1.25E-04	2.24E-04	1.74E-04	1.77E-04	1.82E-04
phenanthrene	4.05E-04	7.28E-04	5.66E-04	5.74E-04	5.91E-04
anthracene	1.02E-04	1.83E-04	1.42E-04	1.44E-04	1.49E-04
cyclopenta[def]phenanthrene	1.59E-05	2.86E-05	2.22E-05	2.26E-05	2.32E-05
2-phenylnaphthalene	7.40E-06	1.33E-05	1.04E-05	1.05E-05	1.08E-05
fluoranthene	1.63E-04	2.94E-04	2.28E-04	2.32E-04	2.39E-04
acephnanthrylene	6.41E-06	1.15E-05	8.96E-06	9.09E-06	9.36E-06
aceanthrylene	5.34E-06	9.60E-06	7.47E-06	7.57E-06	7.80E-06
pyrene	1.12E-04	2.02E-04	1.57E-04	1.59E-04	1.64E-04
benzo[a]fluorine	8.99E-06	1.62E-05	1.26E-05	1.28E-05	1.31E-05
cyclopenta[cd]pyrene	2.86E-06	5.15E-06	4.00E-06	4.06E-06	4.18E-06
benz[a]anthracene	4.45E-05	7.99E-05	6.22E-05	6.31E-05	6.50E-05
chrysene	4.73E-05	8.50E-05	6.61E-05	6.71E-05	6.91E-05
benzo[b]fluoranthene	3.59E-05	6.46E-05	5.03E-05	5.10E-05	5.25E-05
benzo[e]pyrene	2.74E-05	4.92E-05	3.83E-05	3.89E-05	4.00E-05
benzo[a]pyrene	2.91E-05	5.23E-05	4.07E-05	4.13E-05	4.25E-05
perylene	7.70E-06	1.39E-05	1.08E-05	1.09E-05	1.13E-05
benzo[ghi]perylene	1.17E-05	2.11E-05	1.64E-05	1.66E-05	1.71E-05
anthanthrene	4.69E-06	8.43E-06	6.56E-06	6.65E-06	6.85E-06
coronene	1.44E-06	2.59E-06	2.01E-06	2.04E-06	2.10E-06

A.II Supplementary Information of Chapter 4

The following data is in CHEMKIN format

Reduced kinetic model

(Elements; Species; Reactions; Thermodata; Moledata)

```
ELEMENTS H C O N END

SPECIES
  H2 CO CO2 H2O O2 CH4 C2H2 C2H4 C2H6 C6H6 C6H5OH C3H6 CH3OH C3H4 C3H4P C3H8 C4H6-
1 C4H612 C4H613
  C5H6 H CH CH2 HCH CH3 O OH C2H C2H3 HCO C2H5 CH2O CH3O CH2OH HO2 C3H2 C3H5
HCCO CH2CO HCCOH
  NC3H7 CH2CHO CH3CO CH3CHO CH2CHCHO H2CCCH N2
END

REACTIONS JOULES/MOLE
OH + H2 <=> H + H2O 2.14E+8 1.5 14361.
H + O2 <=> OH + O 1.91E+14 0. 68831.
H + O2 <=> HO2 +M 1.4100000000000003E+18 -0.8 0.
OH + OH <=> O + H2O 12300. 2.6 -7863.
HO2 + O <=> OH + O2 1.74E+13 0. -1675.
O + H2 <=> OH + H 51300. 2.7 26335.
OH + O <=> HO2 +M 1.0000000000000003E+17 0. 0.
HO2 + H <=> O + H2O 3.E+13 0. 4480.
HO2 + H <=> O2 + H2 6.61E+13 0. 8918.
HO2 + H <=> OH + OH 1.4E+14 0. 4492.
HO2 + OH <=> O2 + H2O 7.5E+12 0. 0.
HCO + O2 <=> OH + CO2 3.31E+12 -0.4 0.
HO2 + HCO <=> OH + H + CO2 3.E+13 0. 0.
HCO + O2 <=> HO2 + CO 3.3E+13 -0.4 0.
HCO <=> H + CO +M 2.5E+14 0. 70347.
HCO + H <=> CO + H2 9.04E+13 0. 0.
OH + CO <=> H + CO2 6320000. 1.5 -2081.
HO2 + CO <=> OH + CO2 6.03E+13 0. 96087.
CH + H2 <=> HCH + H 2.48E+15 -0.4 12142.
CH + O2 <=> OH + CO 3.3E+13 0. 0.
CH + O2 <=> HCO + O 3.3E+13 0. 0.
CH + H2O <=> CH2O + H 1.17E+15 -0.8 0.
CH + H2O <=> CH2OH 5.71E+12 0. -3161.
CH2O + OH <=> HCO + H2O 3.43E+9 1.2 -1871.
CH2O + H <=> HCO + H2 2.19E+8 1.8 12560.
CH2O + O <=> HCO + OH 1.8E+13 0. 12895.
CH2 + CH4 <=> CH3 + CH3 4.E+13 0. 0.
CH2 + H2 <=> CH3 + H 7.E+13 0. 0.
CH2 + H2O <=> HCH + H2O 3.E+13 0. 0.
CH2 + O2 <=> H + H + CO2 7.83E+12 0. 0.
CH2 + O2 <=> CH2O + O 7.83E+12 0. 0.
CH2 + O2 <=> CO2 + H2 7.83E+12 0. 0.
```

CH2 + O2 <=> OH + H + CO 7.83E+12 0. 0.
CH2 + CO2 <=> CH2O + CO 3.E+12 0. 0.
HCH + O2 <=> H + H + CO2 1.6E+12 0. 4187.
HCH + O2 <=> CH2O + O 5.E+13 0. 37681.
HCH + O2 <=> CO2 + H2 6.9E+11 0. 2093.
HCH + O2 <=> OH + H + CO 8.6E+10 0. -2093.
OH + HCH <=> CH + H2O 1.13E+7 2. 12560.
HCH + CO2 <=> CH2O + CO 1.1E+11 0. 4187.
CH3 + H <=> CH4 +M 6.190000000000002E+23 -1.8 0.
CH3 + H <=> HCH + H2 6.03E+13 0. 63233.
O + CH3 <=> CH2O + H 7.17E+13 0. 0.
O + CH3 <=> HCO + H2 1.26E+13 0. 0.
CH3 + O2 <=> CH3O + O 7.29E+11 0.4 114572.
OH + CH3 <=> CH3OH 2.24E+40 -8.2 48873.
OH + CH3 <=> CH2OH + H 1.09E+11 0.4 -2964.
OH + CH3 <=> CH3O + H 5.74E+12 -0.2 58326.
OH + CH3 <=> HCH + H2O 7500000. 2. 20934.
HO2 + CH3 <=> CH3O + OH 1.81E+13 0. 0.
HCO + CH3 <=> CH4 + CO 2.65E+13 0. 0.
CH3O + CH3 <=> CH2O + CH4 2.41E+13 0. 0.
CH2O + CH3 <=> HCO + CH4 7.77E-8 6.1 8248.
CH3 + CH3 <=> C2H5 + H 1.67E+13 -0.3 54805.
CH3 + CH3 <=> C2H4 + H2 1.E+16 0. 134103.
CH3 + CH3 <=> C2H6 3.62E+57 -13.4 86918.
CH2OH <=> CH2O + H +M 1.67E+24 -2.5 143147.
CH2OH + O2 <=> HO2 + CH2O 2.41E+14 0. 20934.
CH2OH + H <=> CH2O + H2 2.E+13 0. 0.
CH3O <=> CH2O + H +M 5.42E+13 0. 56480.
CH3O + H <=> CH2O + H2 2.E+13 0. 0.
CH3O + CO <=> CH3 + CO2 1.57E+13 0. 49392.
CH3OH <=> OH + CH3 +M 3.5E+16 0. 278188.
CH3OH <=> CH2 + H2O +M 7.E+15 0. 278188.
CH3 + CH3OH <=> CH2OH + CH4 31.9 3.2 30028.
CH3 + CH3OH <=> CH3O + CH4 14.5 3.1 29035.
O + CH3OH <=> CH2OH + OH 380000. 2.5 12895.
O + CH3OH <=> CH3O + OH 1.E+13 0. 19611.
OH + CH3OH <=> CH2OH + H2O 1.E+13 0. 7105.
OH + CH3OH <=> CH3O + H2O 1.E+13 0. 7105.
H + CH3OH <=> CH2OH + H2 3.98E+13 0. 25519.
H + CH3OH <=> CH3O + H2 3.98E+13 0. 25519.
CH4 + O2 <=> HO2 + CH3 7.94E+13 0. 234461.
H + CH4 <=> CH3 + H2 1.48E+14 0. 56878.
OH + CH4 <=> CH3 + H2O 1.57E+7 1.8 11639.
O + CH4 <=> OH + CH3 6.92E+8 1.6 35546.
C2H + O2 <=> HCO + CO 2.41E+12 0. 0.
C2H + O2 <=> H + CO + CO 3.52E+13 0. 0.
HCCO + H <=> CH2 + CO 1.E+14 0. 0.
HCCO + O <=> H + CO + CO 1.E+14 0. 0.
HCCO + H <=> HCCOH 1.81E+39 -8. 34960.
HCCO + O2 <=> OH + CO + CO 1.46E+12 0. 10467.

C2H + O2 <=> HCCO + O 5.E+13 0. 6280.
CH2CO <=> HCH + CO +M 3.6E+15 0. 248005.
CH2CO + O <=> HCO + HCO 2.E+13 0. 9600.
CH2CO + O <=> CH2 + CO2 1.75E+12 0. 5652.
CH2CO + H <=> HCCO + H2 5.E+13 0. 33494.
CH2CO + OH <=> HCCO + H2O 7.5E+12 0. 8374.
CH2CO + OH <=> CH2O + HCO 2.8E+13 0. 0.
CH2CO + OH <=> CH3O + CO 2.8E+13 0. 0.
HCCOH + H <=> CH2CO + H 1.E+13 0. 0.
H + C2H2 <=> C2H + H2 6.03E+13 0. 116477.
C2H2 + H2 <=> C2H4 1.2E+28 -5. 194309.
OH + C2H2 <=> C2H + H2O 3.37E+7 2. 58615.
OH + C2H2 <=> HCCOH + H 504000.00000000006 2.3 56522.
OH + C2H2 <=> CH2CO + H 0.000218 4.5 -4187.
OH + C2H2 <=> CH3 + CO 0.00048300000000000003 4. -8374.
C2H + CH4 <=> CH3 + C2H2 1.81E+12 0. 2081.
CH2 + C2H2 <=> HCH + C2H2 4.E+13 0. 0.
O + C2H2 <=> C2H + OH 3.16E+15 -0.6 62802.
O + C2H2 <=> HCH + CO 1400000. 2.1 6540.
O + C2H2 <=> HCCO + H 5800000. 2.1 6540.
C2H3 <=> H + C2H2 3.93E+33 -6.7 188867.
C2H3 + H <=> C2H2 + H2 1.21E+13 0. 0.
C2H3 + O <=> HCO + CH2 3.E+13 0. 0.
C2H3 + O2 <=> CH2O + HCO 4.58E+16 -1.4 4250.
C2H3 + O2 <=> HO2 + C2H2 1340000. 1.6 -1604.
C2H3 + CH3 <=> C2H2 + CH4 1.99E+13 0. 0.
H + C2H4 <=> C2H3 + H2 5.07E+7 1.9 54223.
H + C2H4 <=> C2H5 8.42E+8 1.5 4145.
CH3 + HCH <=> H + C2H4 4.2E+13 0. 0.
CH2CO + CH2 <=> C2H4 + CO 1.6E+14 0. 0.
C2H3 + H <=> C2H4 2.4800000000000002E+33 -6.2 23739.
CH3 + CH2 <=> H + C2H4 4.94E+13 -0.1 394.
CH + CH4 <=> H + C2H4 6.E+13 0. 0.
O + C2H4 <=> HCO + CH3 1.6E+9 1.2 3123.
OH + C2H4 <=> C2H3 + H2O 2.02E+13 0. 24932.
OH + C2H4 <=> CH2O + CH3 1.05E+12 0. -3835.
CH3 + C2H4 <=> C2H3 + CH4 4.16E+12 0. 46591.
CH3 + C2H6 <=> C2H5 + CH4 0.55 4. 34750.
H + C2H6 <=> C2H5 + H2 540. 3.5 21813.
O + C2H6 <=> C2H5 + OH 3.E+7 2. 21415.
OH + C2H6 <=> C2H5 + H2O 8.7E+9 1.1 7578.
CH2 + C2H6 <=> C2H5 + CH3 1.2E+14 0. 0.
O + C2H4 <=> CH2CHO + H 1210000. 2.1 0.
O + C3H6 <=> CH2CHO + CH3 1080000. 2.1 -3329.
CH2CHO <=> CH2CO + H 1.58E+13 0. 146412.
CH2CHO <=> CH3CO 1.E+13 0. 197198.
CH3CO <=> CH3 + CO 8.74E+42 -8.6 93885.
CH3CO + H <=> HCO + CH3 3.3E+13 0. 0.
C2H5 + O <=> CH3CHO + H 6.62E+13 0. 0.
C2H3 + OH <=> CH3CHO 3.01E+13 0. 0.

CH3CHO <=> HCO + CH3 7.E+15 0. 341953.
CH3CHO + H <=> CH3CO + H2 4.E+13 0. 17614.
CH3CHO + OH <=> CH3CO + H2O 1.E+13 0. 0.
CH3CHO + O <=> CH3CO + OH 5.E+12 0. 7503.
CH3CHO + CH3 <=> CH3CO + CH4 0.00000199 5.6 10316.
C3H2 + O <=> HCO + C2H 6.8E+13 0. 0.
C3H2 + O <=> C2H2 + CO 1.E+14 0. 0.
C3H2 + OH <=> HCO + C2H2 5.E+13 0. 0.
H2CCCH <=> C3H2 + H 5.2E+12 0. 328442.
H2CCCH + H <=> C3H2 + H2 5.E+13 0. 4187.
H2CCCH + OH <=> C3H2 + H2O 2.E+13 0. 0.
H2CCCH + O <=> C3H2 + OH 3.2E+12 0. 0.
HCCO + C2H2 <=> H2CCCH + CO 1.1E+11 0. 12560.
H2CCCH + O2 <=> CH2CO + HCO 3.E+10 0. 12008.
CH2 + C2H2 <=> H2CCCH + H 1.E+22 -2.5 18564.
HCH + C2H2 <=> H2CCCH + H 1.2E+13 0. 27633.
H2CCCH + O <=> CH2O + C2H 7.17E+13 0. 0.
H2CCCH + OH <=> CH2CHCHO 3.01E+13 0. 0.
HCO + C2H3 <=> CH2CHCHO 1.81E+13 0. 0.
C3H5 + O <=> CH2CHCHO + H 6.03E+13 0. 0.
C3H4 <=> H2CCCH + H 2.3E+12 0. 291753.
C3H4P <=> H2CCCH + H 1.34E+12 0. 292833.
CH + C2H4 <=> H + C3H4 7.17E+16 -0.8 5275.
CH2 + C2H2 <=> C3H4P 3.71E+37 -7.5 28680.
O + C3H4 <=> C2H4 + CO 1.5E+13 0. 8805.
OH + C3H4 <=> HCO + C2H4 1.E+12 0. 0.
CH3 + C3H4 <=> H2CCCH + CH4 2.E+12 0. 32238.
CH3 + C3H4P <=> H2CCCH + CH4 2.E+12 0. 32238.
H + C3H4 <=> CH3 + C2H2 2.E+13 0. 10048.
OH + C3H4 <=> CH2CO + CH3 3.37E+12 0. -1273.
OH + C3H4P <=> CH2CO + CH3 4.28E+11 0. -3529.
H + C3H4 <=> H2CCCH + H2 3.E+7 2. 20934.
OH + C3H4 <=> H2CCCH + H2O 2.E+7 2. 4187.
H + C3H4P <=> H2CCCH + H2 3.E+7 2. 20934.
OH + C3H4P <=> H2CCCH + H2O 2.E+7 2. 4187.
CH3 + C2H2 <=> H + C3H4P 19200. 2.4 53976.
H + C3H4 <=> C3H5 1.2E+11 0.7 12590.
C3H5 + OH <=> C3H4 + H2O 6.03E+12 0. 0.
CH2OH + C2H3 <=> C3H5 + OH 1.21E+13 0. 0.
HCH + C2H4 <=> C3H5 + H 3.19E+12 0. 22129.
CH3 + C2H2 <=> C3H5 14000. 2.2 69082.
C2H3 + CH3 <=> C3H5 + H 7.2E+13 0. 0.
C3H5 + H <=> C3H6 5.8E+11 0.2 -214.
CH3 + C3H6 <=> C3H5 + CH4 2.21 3.5 23760.
O + C3H6 <=> C3H5 + OH 6.03E+10 0.7 31958.
C3H5 + HCO <=> C3H6 + CO 6.03E+13 0. 0.
C3H5 + CH3O <=> CH2O + C3H6 3.01E+13 0. 0.
C3H5 + C2H3 <=> C3H6 + C2H2 4.82E+12 0. 0.
CH2 + C2H4 <=> C3H6 9.03E+13 0. 0.
NC3H7 <=> CH3 + C2H4 1.2E+13 0. 126873.

```
H + C3H6 <=> NC3H7 1.3E+13 0. 13653.
H + C3H8 <=> NC3H7 + H2 1330000. 2.5 28286.
OH + C3H8 <=> NC3H7 + H2O 3.16E+7 1.8 3910.
O + C3H8 <=> NC3H7 + OH 193000. 2.7 15558.
CH3 + C3H8 <=> NC3H7 + CH4 0.904 3.6 29952.
C2H5 + CH3 <=> C3H8 3.37E+13 0. 0.
C2H3 + C2H4 <=> H + C4H613 2.63E+15 -1. 24911.
C2H3 + C2H3 <=> C4H613 2.E+13 0. 0.
OH + C4H613 <=> C3H5 + CH2O 1.E+12 0. 0.
OH + C4H613 <=> CH2CO + C2H5 1.E+12 0. 0.
H2CCCH + CH3 <=> C4H6-1 5.42E+13 0. 0.
C2H + C3H6 <=> CH + C4H6-1 1.21E+13 0. 0.
C4H6-1 <=> C4H612 2.5E+13 0. 272142.
O + C4H6-1 <=> C3H6 + CO 2.E+13 0. 6946.
H2CCCH + CH3 <=> C4H612 3.61E+13 0. 0.
C4H612 <=> C4H613 2.5E+13 0. 263768.
H + C4H612 <=> CH3 + C3H4 6.E+12 0. 8792.
H + C4H612 <=> CH3 + C3H4P 6.E+12 0. 8792.
H + C5H6 <=> C3H5 + C2H2 6.6E+14 0. 51686.
H2CCCH + H2CCCH <=> C6H6 3.E+12 0. 0.
H2CCCH + C3H4 <=> H + C6H6 2.2E+11 0. 8374.
OH + C6H6 <=> H + C6H5OH 1.56E+24 -3.2 70757.
C6H5OH <=> C5H6 + CO 1.E+12 0. 254566.
END
```

Thermodata

```
THERMO
   300.000   1000.00    5000.00
!
H2                H   2    0    0    0      300.00   5000.00 1000.00
 0.29914230E+01 0.70006440E-03-0.56338280E-07-0.92315780E-11 0.15827519E-14
-0.83503400E+03-0.13551101E+01 0.32981240E+01 0.82494410E-03-0.81430150E-06
-0.94754340E-10 0.41348720E-12-0.10125209E+04-0.32940940E+01
CO                C   1O   1    0    0      300.00   5000.00 1000.00
 0.30250780E+01 0.14426885E-02-0.56308270E-06 0.10185813E-09-0.69109510E-14
-0.14268350E+05 0.61082170E+01 0.32624510E+01 0.15119409E-02-0.38817550E-05
 0.55819440E-08-0.24749510E-11-0.14310539E+05 0.48488970E+01
CO2               C   1O   2    0    0      300.00   5000.00 1000.00
 0.44536230E+01 0.31401680E-02-0.12784105E-05 0.23939960E-09-0.16690333E-13
-0.48966960E+05-0.95539590E+00 0.22757240E+01 0.99220720E-02-0.10409113E-04
 0.68666860E-08-0.21172800E-11-0.48373140E+05 0.10188488E+02
H2O               H   2O   1    0    0      300.00   5000.00 1000.00
 0.26721450E+01 0.30562930E-02-0.87302600E-06 0.12009964E-09-0.63916180E-14
-0.29899210E+05 0.68628170E+01 0.33868420E+01 0.34749820E-02-0.63546960E-05
 0.69685810E-08-0.25065880E-11-0.30208110E+05 0.25902320E+01
O2                O   2    0    0    0      300.00   5000.00 1000.00
 0.36975780E+01 0.61351970E-03-0.12588420E-06 0.17752810E-10-0.11364354E-14
-0.12339301E+04 0.31891650E+01 0.32129360E+01 0.11274864E-02-0.57561500E-06
 0.13138773E-08-0.87685540E-12-0.10052490E+04 0.60347370E+01
CH4               H   4C   1    0    0      300.00   5000.00 1000.00
 0.16834780E+01 0.10237236E-01-0.38751280E-05 0.67855850E-09-0.45034230E-13
```

-0.10080787E+05 0.96233950E+01 0.77874150E+00 0.17476680E-01-0.27834090E-04
0.30497080E-07-0.12239307E-10-0.98252290E+04 0.13722195E+02
C2H2 H 2C 2 0 0 300.00 5000.00 1405.00
0.52551833E+01 0.41126832E-02-0.13421064E-05 0.20144682E-09-0.11401724E-13
0.25376844E+05-0.69583043E+01 0.30445275E+01 0.11802996E-01-0.11599793E-04
0.62058671E-08-0.12941556E-11 0.25930768E+05 0.40821994E+01
C2H4 H 4C 2 0 0 300.00 5000.00 1000.00
0.35284180E+01 0.11485185E-01-0.44183850E-05 0.78446000E-09-0.52668480E-13
0.44282880E+04 0.22303890E+01-0.86148800E+00 0.27961620E-01-0.33886770E-04
0.27851520E-07-0.97378790E-11 0.55730460E+04 0.24211480E+02
C2H6 H 6C 2 0 0 300.00 4000.00 1000.00
0.48259380E+01 0.13840429E-01-0.45572580E-05 0.67249670E-09-0.35981610E-13
-0.12717793E+05-0.52395060E+01 0.14625388E+01 0.15494667E-01 0.57805070E-05
-0.12578319E-07 0.45862670E-11-0.11239176E+05 0.14432295E+02
C6H6 H 6C 6 0 0 300.00 5000.00 1401.00
0.14068855E+02 0.16785207E-01-0.57642744E-05 0.89755385E-09-0.52187523E-13
0.28007846E+04-0.57257448E+02-0.57879113E+01 0.68544313E-01-0.58249917E-04
0.25305399E-07-0.44018625E-11 0.91206264E+04 0.47415051E+02
C6H5OH H 6C 6O 1 0 300.00 5000.00 1391.00
0.16869380E+02 0.17083843E-01-0.59894684E-05 0.94539842E-09-0.55485920E-13
-0.19729443E+05-0.68788356E+02-0.49290027E+01 0.77603683E-01-0.72920815E-04
0.35183114E-07-0.67407997E-11-0.12992091E+05 0.45093539E+02
C3H6 H 6C 3 0 0 300.00 5000.00 1387.00
0.77378590E+01 0.13959687E-01-0.47554593E-05 0.73616508E-09-0.42620234E-13
-0.14036133E+04-0.18588834E+02 0.50437818E+00 0.27764217E-01-0.13792831E-04
0.29322250E-08-0.14725770E-12 0.14644844E+04 0.21434278E+02
CH3OH H 4C 1O 1 0 300.00 5000.00 1000.00
0.40290610E+01 0.93765930E-02-0.30502540E-05 0.43587930E-09-0.22247230E-13
-0.26157910E+05 0.23781950E+01 0.26601150E+01 0.73415080E-02 0.71700500E-05
-0.87931940E-08 0.23905700E-11-0.25353480E+05 0.11232631E+02
C3H4 H 4C 3 0 0 300.00 5000.00 1396.00
0.73652725E+01 0.96256533E-02-0.32646767E-05 0.50387464E-09-0.29110277E-13
0.18598207E+05-0.17428834E+02 0.69581263E+00 0.25791342E-01-0.18703919E-04
0.74019820E-08-0.12340417E-11 0.20885978E+05 0.18232493E+02
C3H4P H 4C 3 0 0 300.00 5000.00 1392.00
0.71149140E+01 0.98264574E-02-0.33307731E-05 0.51381742E-09-0.29672667E-13
0.18617844E+05-0.15385817E+02 0.16053406E+01 0.22337655E-01-0.14510555E-04
0.52366558E-08-0.82390900E-12 0.20614560E+05 0.14410263E+02
C3H8 H 8C 3 0 0 300.00 5000.00 1000.00
0.75252170E+01 0.18890340E-01-0.62839240E-05 0.91793730E-09-0.48124100E-13
-0.16464548E+05-0.17843900E+02 0.89692080E+00 0.26689860E-01 0.54314250E-05
-0.21260000E-07 0.92433300E-11-0.13954918E+05 0.19355330E+02
C4H6-1 H 6C 4 0 0 300.00 5000.00 1380.00
0.10283206E+02 0.14842817E-01-0.51707167E-05 0.81255583E-09-0.47538012E-13
0.14855527E+05-0.30809982E+02 0.14507530E+01 0.33625829E-01-0.21183759E-04
0.75439559E-08-0.12285561E-11 0.18265856E+05 0.17548237E+02
C4H612 H 6C 4 0 0 300.00 3000.00 1000.00
0.17815570E+02-0.42575020E-02 0.10511850E-04-0.44738440E-08 0.58481380E-12
0.12673420E+05-0.69826620E+02 0.10234670E+01 0.34959190E-01-0.22009050E-04
0.69422720E-08-0.78791870E-12 0.18117990E+05 0.19750660E+02
C4H613 H 6C 4 0 0 300.00 3000.00 1000.00
0.71309430E+01 0.20640080E-01-0.93239060E-05 0.21473070E-08-0.20613610E-12

0.96126540E+04-0.14172220E+02-0.25309000E+01 0.53879690E-01-0.51739330E-04
0.25107200E-07-0.43247260E-11 0.11876910E+05 0.33913880E+02
C5H6 H 6C 5 0 0 300.00 5000.00 1402.00
0.12657500E+02 0.15330120E-01-0.52382136E-05 0.81286709E-09-0.47150482E-13
0.10308345E+05-0.47538606E+02-0.47825904E+01 0.60987303E-01-0.51736393E-04
0.22517354E-07-0.39262111E-11 0.15838284E+05 0.44322620E+02
H H 1 0 0 0 300.00 5000.00 1000.00
0.25000000E+01 0.00000000E+00 0.00000000E+00 0.00000000E+00 0.00000000E+00
0.25471620E+05-0.46011760E+00 0.25000000E+01 0.00000000E+00 0.00000000E+00
0.00000000E+00 0.00000000E+00 0.25471620E+05-0.46011760E+00
CH H 1C 1 0 0 300.00 5000.00 1000.00
0.21962230E+01 0.23403810E-02-0.70582010E-06 0.90075820E-10-0.38550400E-14
0.70867230E+05 0.91783730E+01 0.32002020E+01 0.20728750E-02-0.51344310E-05
0.57338900E-08-0.19555330E-11 0.70452590E+05 0.33315870E+01
CH2 H 2C 1 0 0 300.00 5000.00 1372.00
0.27923276E+01 0.31287995E-02-0.81094355E-06 0.95595675E-10-0.42869914E-14
0.50808597E+05 0.61111714E+01 0.34838743E+01 0.16129581E-02 0.44065603E-06
-0.37108570E-09 0.62731340E-13 0.50557264E+05 0.23595477E+01
HCH H 2C 1 0 0 300.00 5000.00 1382.00
0.32586924E+01 0.24949906E-02-0.57083657E-06 0.59165176E-10-0.23100011E-14
0.46574490E+05 0.40319785E+01 0.35946997E+01 0.17811574E-02 0.52155119E-09
-0.14816465E-09 0.26886911E-13 0.46448745E+05 0.21988956E+01
CH3 H 3C 1 0 0 300.00 5000.00 1386.00
0.34694774E+01 0.52184201E-02-0.17264628E-05 0.26173882E-09-0.14924054E-13
0.16422949E+05 0.18468402E+01 0.35591455E+01 0.34995297E-02 0.11718796E-05
-0.14250870E-08 0.31464380E-12 0.16596448E+05 0.19897086E+01
O O 1 0 0 0 300.00 5000.00 1000.00
0.25420590E+01-0.27550610E-04-0.31028030E-08 0.45510670E-11-0.43680510E-15
0.29230800E+05 0.49203080E+01 0.29464280E+01-0.16381665E-02 0.24210310E-05
-0.16028431E-08 0.38906960E-12 0.29147640E+05 0.29639950E+01
OH H 1O 1 0 0 300.00 5000.00 1000.00
0.28827300E+01 0.10139743E-02-0.22768770E-06 0.21746830E-10-0.51263050E-15
0.38868880E+04 0.55957120E+01 0.36372660E+01 0.18509100E-03-0.16761646E-05
0.23872020E-08-0.84314420E-12 0.36067810E+04 0.13588605E+01
C2H H 1C 2 0 0 300.00 5000.00 1362.00
0.48754659E+01 0.18781770E-02-0.66508771E-06 0.10567989E-09-0.62311140E-14
0.66670198E+05-0.35767333E+01 0.35739268E+01 0.39893253E-02-0.15358980E-05
-0.34918695E-11 0.85995602E-13 0.67225614E+05 0.37610088E+01
C2H3 H 3C 2 0 0 300.00 5000.00 1400.00
0.53428229E+01 0.62790981E-02-0.21163834E-05 0.32519504E-09-0.18726656E-13
0.33659063E+05-0.51633995E+01 0.12956980E+01 0.16538091E-01-0.12473789E-04
0.52234681E-08-0.91830615E-12 0.35008128E+05 0.16326230E+02
HCO H 1C 1O 1 0 300.00 5000.00 1000.00
0.35572710E+01 0.33455720E-02-0.13350060E-05 0.24705720E-09-0.17138500E-13
0.39163240E+04 0.55522990E+01 0.28983290E+01 0.61991460E-02-0.96230840E-05
0.10898249E-07-0.45748850E-11 0.41599220E+04 0.89836140E+01
C2H5 H 5C 2 0 0 300.00 5000.00 1382.00
0.57030513E+01 0.10567765E-01-0.35795298E-05 0.55195147E-09-0.31865871E-13
0.11789009E+05-0.72481654E+01 0.17640433E+01 0.16467138E-01-0.52991745E-05
-0.36026590E-09 0.37339795E-12 0.13535340E+05 0.15158216E+02
CH2O H 2C 1O 1 0 300.00 5000.00 1000.00
0.29956060E+01 0.66813210E-02-0.26289540E-05 0.47371530E-09-0.32125170E-13

-0.15320369E+05 0.69125720E+01 0.16527311E+01 0.12631439E-01-0.18881680E-04
0.20500310E-07-0.84132370E-11-0.14865404E+05 0.13784820E+02
CH3O H 3C 1O 1 0 300.00 3000.00 1000.00
0.37707990E+01 0.78714970E-02-0.26563840E-05 0.39444310E-09-0.21126160E-13
0.12783252E+03 0.29295750E+01 0.21062040E+01 0.72165950E-02 0.53384720E-05
-0.73776360E-08 0.20756100E-11 0.97860110E+03 0.13152177E+02
CH2OH H 3C 1O 1 0 250.00 4000.00 1000.00
0.63275200E+01 0.36082700E-02-0.32015470E-06-0.19387500E-09 0.35097040E-13
-0.44745090E+04-0.83293650E+01 0.28626280E+01 0.10015273E-01-0.52854350E-06
-0.51385390E-08 0.22460410E-11-0.33496780E+04 0.10397938E+02
HO2 H 1O 2 0 0 300.00 5000.00 1000.00
0.40721910E+01 0.21312960E-02-0.53081450E-06 0.61122690E-10-0.28411640E-14
-0.15797270E+03 0.34760290E+01 0.29799630E+01 0.49966970E-02-0.37909970E-05
0.23541920E-08-0.80890240E-12 0.17622730E+03 0.92227240E+01
C3H2 H 2C 3 0 0 300.00 5000.00 1419.00
0.78914079E+01 0.39425250E-02-0.11850322E-05 0.16725611E-09-0.90368274E-14
0.62537411E+05-0.14769157E+02 0.45282403E+01 0.15930343E-01-0.16843493E-04
0.90046332E-08-0.18265016E-11 0.63287621E+05 0.18190004E+01
C3H5 H 5C 3 0 0 300.00 5000.00 1390.00
0.90485611E+01 0.10653245E-01-0.36935719E-05 0.57861787E-09-0.33779180E-13
0.16221203E+05-0.25828271E+02-0.12747136E+00 0.33680596E-01-0.26823817E-04
0.11536915E-07-0.20621554E-11 0.19314801E+05 0.22999225E+02
HCCO H 1C 2O 1 0 300.00 4000.00 1000.00
0.67580730E+01 0.20004000E-02-0.20276070E-06-0.10411318E-09 0.19651640E-13
0.19015130E+05-0.90712620E+01 0.50479650E+01 0.44534780E-02 0.22682820E-06
-0.14820945E-08 0.22507410E-12 0.19658910E+05 0.48184390E+00
CH2CO H 2C 2O 1 0 300.00 5000.00 1000.00
0.60388170E+01 0.58048400E-02-0.19209530E-05 0.27944840E-09-0.14588676E-13
-0.85834020E+04-0.76575810E+01 0.29749700E+01 0.12118712E-01-0.23450450E-05
-0.64666850E-08 0.39056490E-11-0.76326360E+04 0.86735530E+01
HCCOH H 2C 2O 1 0 300.00 4000.00 1000.00
0.73283240E+01 0.33364160E-02-0.30247050E-06-0.17811060E-09 0.32451680E-13
0.75982580E+04-0.14012140E+02 0.38994650E+01 0.97010750E-02-0.31193090E-06
-0.55377320E-08 0.24657320E-11 0.87011900E+04 0.44918740E+01
NC3H7 H 7C 3 0 0 300.00 5000.00 1390.00
0.88095198E+01 0.15116147E-01-0.51413977E-05 0.79502069E-09-0.45990023E-13
0.78293667E+04-0.22264586E+02 0.60551327E+00 0.32279746E-01-0.18621137E-04
0.55708181E-08-0.69835638E-12 0.10939174E+05 0.22606492E+02
CH2CHO H 3C 2O 1 0 300.00 5000.00 1000.00
0.59756700E+01 0.81305910E-02-0.27436240E-05 0.40703040E-09-0.21760170E-13
0.49032180E+03-0.50452510E+01 0.34090620E+01 0.10738574E-01 0.18914920E-05
-0.71585830E-08 0.28673850E-11 0.15214766E+04 0.95582900E+01
CH3CO H 3C 2O 1 0 300.00 5000.00 1000.00
0.56122790E+01 0.84498860E-02-0.28541470E-05 0.42383760E-09-0.22684030E-13
-0.51878630E+04-0.32749490E+01 0.31252780E+01 0.97782200E-02 0.45214480E-05
-0.90094620E-08 0.31937170E-11-0.41085070E+04 0.11228854E+02
CH3CHO H 4C 2O 1 0 300.00 5000.00 1000.00
0.58686500E+01 0.10794241E-01-0.36455300E-05 0.54129120E-09-0.28968440E-13
-0.22645680E+05-0.60129460E+01 0.25056950E+01 0.13369907E-01 0.46719530E-05
-0.11281401E-07 0.42635660E-11-0.21245880E+05 0.13350887E+02
CH2CHCHO H 4C 3O 1 0 200.00 6000.00 1000.00
0.76558575E+01 0.12913863E-01-0.46751031E-05 0.75862334E-09-0.45576178E-13

-0.12500713E+05-0.16446334E+02 0.35151329E+01 0.87649733E-02 0.35636110E-04
-0.53312383E-07 0.22003832E-10-0.10614745E+05 0.86613787E+01
H2CCCH H 3C 3 0 0 300.00 5000.00 1399.00
0.79417793E+01 0.65643120E-02-0.22021643E-05 0.33724460E-09-0.19373159E-13
0.38180435E+05-0.17160875E+02 0.31223355E+01 0.20558534E-01-0.18409793E-04
0.89518486E-08-0.17488153E-11 0.39624702E+05 0.78253019E+01
N2 N 2 0 0 0 300.00 5000.00 1000.00
0.29266400E+01 0.14879768E-02-0.56847600E-06 0.10097038E-09-0.67533510E-14
-0.92279770E+03 0.59805280E+01 0.32986770E+01 0.14082404E-02-0.39632220E-05
0.56415150E-08-0.24448540E-11-0.10208999E+04 0.39503720E+01

Moledata

H2 1 2.016 38.000 2.920 0.000 0.790 280.000
CO 1 28.010 98.100 3.650 0.000 1.950 1.800
CO2 1 44.010 244.000 3.763 0.000 2.650 2.100
H2O 2 18.015 572.400 2.605 1.844 0.000 4.000
O2 1 31.999 107.400 3.458 0.000 1.600 3.800
CH4 2 16.043 141.400 3.746 0.000 2.600 13.000
C2H2 1 26.038 209.000 4.100 0.000 0.000 2.500
C2H4 2 28.054 243.000 4.050 0.000 0.000 2.000
C2H6 2 30.070 246.000 4.320 0.000 0.000 2.000
C6H6 2 78.114 412.300 5.349 0.000 0.000 1.000
C6H5OH 2 94.113 450.000 5.549 0.000 0.000 1.000
C3H6 2 42.081 373.300 4.424 0.000 0.000 1.000
CH3OH 2 32.042 417.000 3.690 1.700 0.000 2.000
C3H4 1 40.065 373.300 4.424 0.000 0.000 1.000
C3H4P 1 40.065 252.000 4.760 0.000 0.000 1.000
C3H8 2 44.097 266.800 4.982 0.000 0.000 1.000
C4H6-1 2 54.092 357.000 5.176 0.000 0.000 1.000
C4H612 2 54.092 357.000 5.176 0.000 0.000 1.000
C4H613 2 54.092 357.000 5.176 0.000 0.000 1.000
C5H6 1 66.103 357.000 5.176 0.000 0.000 1.000
H 0 1.008 145.000 2.050 0.000 0.000 0.000
CH 1 13.019 80.000 2.750 0.000 0.000 0.000
CH2 1 14.027 141.400 3.746 0.000 0.000 13.000
HCH 1 14.027 144.000 3.800 0.000 0.000 0.000
CH3 2 15.035 141.400 3.746 0.000 0.000 13.000
O 0 15.999 80.000 2.750 0.000 0.000 0.000
OH 1 17.007 80.000 2.750 0.000 0.000 0.000
C2H 1 25.030 209.000 4.100 0.000 0.000 2.500
C2H3 1 27.046 209.000 4.100 0.000 0.000 2.500
HCO 2 29.018 498.000 3.590 0.000 0.000 0.000
C2H5 2 29.062 246.000 4.320 0.000 0.000 2.000
CH2O 2 30.026 498.000 3.590 0.000 0.000 2.000
CH3O 2 31.034 417.000 3.690 1.700 0.000 2.000
CH2OH 2 31.034 417.000 3.690 1.700 0.000 2.000
HO2 2 33.007 107.400 3.458 0.000 0.000 1.000
C3H2 1 38.049 373.300 4.424 0.000 0.000 1.000
C3H5 1 41.073 373.300 4.424 0.000 0.000 1.000
HCCO 2 41.029 436.000 3.970 0.000 0.000 2.000
CH2CO 2 42.037 436.000 3.970 0.000 0.000 2.000
HCCOH 2 42.037 436.000 3.970 0.000 0.000 2.000

NC3H7 2 43.089 266.800 4.982 0.000 0.000 1.000
CH2CHO 2 43.045 436.000 3.970 0.000 0.000 2.000
CH3CO 2 43.045 436.000 3.970 0.000 0.000 2.000
CH3CHO 2 44.053 436.000 3.970 0.000 0.000 2.000
CH2CHCHO 2 56.064 436.000 3.970 0.000 0.000 2.000
H2CCCH 2 39.057 252.000 4.760 0.000 0.000 1.000
N2 1 28.013 100.000 2.790 0.000 0.000 0.000

A.III Japanese Abstract

論文提出者　　李　成義（リ チョンイ）

論文題名　　A study on modelling and simulation on reacting flow included in thermochemical conversion process of coal（石炭熱化学転換プロセスにおける反応性流体のモデリングと数値解析に関する研究

論文調査委員　　主査　九州大学　准教授　則永　行庸
副査　〃　教　授　林　潤一郎
〃　〃　〃　尹　聖昊
〃　〃　准教授　渡邉　裕章

博士論文の要旨

エネルギー資源の殆どを海外に依存する我が国にとって、埋蔵量が豊富で地域偏在性が低く、原油、天然ガスに比べて発熱量当たりの価格が安い、という特長を持つ石炭は、最も重要なエネルギー資源の一つである。石炭の高効率利用技術開発は、地球温暖化や資源枯渇問題の観点から意義があるが、なかでも、石炭をガス化して得られる可燃性ガスを燃料としてガスタービンを駆動し、さらに蒸気タービンと複合する石炭ガス化複合発電が注目されている。

石炭ガス化においては、ガス化に必要な熱を石炭の部分燃焼で賄うが、この燃焼による化学エネルギー損失を最小化するには、より低温でガス化を操作する必要がある。しかし、低温での反応操作は、初期反応である熱分解において不可避的に生成するタール（多環芳香族化合物を主成分とする重質油成分）の残留を招き、これによるプロセス連続運転の障害が生じる。したがって、低温ガス化プロセスにおいては、生成ガス中に含まれるタールを非凝縮性成分へと転換する改質工程を設ける必要がある。

そこで本研究では、石炭から生成するタール含有ガスを、共存チャーによる不均一反応、および気相部分酸化により改質することを想定し、これらの過程を考慮した反応速度モデルを実験結果や素反応データベースに基づいて構築するとともに、反応速度モデルと流体モデルを連結した数値解析による反応器設計法を新たに提案している。本研究において得られた知見は以下のように纏められる。

（１）石炭の熱分解で生成するタールの共存チャーによる改質特性を検討している。石炭および石炭熱分解により得たチャーを粒子落下式管状反応器に同時供給し、反応器出口の生成物を分析することにより得た実験結果の反応速度解析を行い、ガス、タール、スス、チャーといった擬似成分およびこれらの成分間の反応を考慮した速度モデルを構築するとともに、各速度定数と温度（973－1173 K）、水蒸気分圧（0－0.05 MPa）、粒子ホールドアップ（8.3×10-6－2.5×10-4）との関係を明らかにしている。加えて、速度モデルとオイラー・オイラー気固混相流モデルを連結した三次元熱流体シミュレーションを実施し、実験結果の再現に成功している。

（２）気相部分酸化によるタール蒸気含有ガス改質特性の机上予測を可能とする数値解析手法を開発している。全長約 3 m、内径 0.6 m のベンチスケール改質炉におけ

る、石炭乾留ガス（コークス炉ガス）の気相部分酸化試験を解析対象としている。コークス炉ガスの組成を分子量 2 の水素から 300 のコロネンに至る 40 種以上の化合物で近似し、これらの化合物および化合物間の反応を網羅する約 2,000 の素反応から成る詳細反応速度モデルを採用、詳細反応速度モデルと一次元流体モデルを連結する手法を検討している。反応熱と改質炉壁からの放熱を考慮した熱収支式を解くことにより、改質炉内ガス温度分布を予測する手法を新たに提案し、改質特性の再現に成功している。さらに、流れ方向の拡散を考慮することによる予測精度の向上を明らかにしている。

（３）詳細反応速度モデルに感度解析を施し、コークス炉ガスの改質特性を記述する主要な因子であるガス温度、主要ガス（水素、一酸化炭素、二酸化炭素、メタン）濃度の計算結果に与える影響が小さな反応を取り除き、47 化学種と 410 素反応で構成される簡略化モデルを構築している。さらに、乱流－化学反応相互作用モデルに EDC（Eddy Dissipation Concept）を採用し、簡略化モデルと三次元乱流モデルを連成することで、改質炉内の温度、濃度および速度場の三次元空間分布の可視化と試験結果の再現にも成功している。

以上要するに、本論文は、石炭タール蒸気を含む多成分混合ガスの改質反応特性を予測する数値解析手法を開発したもので、経験的気固反応速度モデルと混相流モデルを連結した手法により、粒子落下型管状反応器における石炭転換特性を再現している。さらに、タール蒸気含有ガス気相部分酸化反応の予測に、約 2,000 の素反応から成る詳細モデルと一次元流体モデル、および簡略化素反応速度モデルと三次元乱流モデルを連結した手法を適用し、ベンチスケール改質炉における実測結果の再現にも成功したものであり、得られた新知見は、石炭熱化学転換プロセス開発に有用で、化学反応工学へ寄与する。

A.IV Journal Paper & Conference Publication

Journal Paper

- Srinivas Appari, Ryota Tanaka, **Chengyi Li**, Shiji Kudo, Jun-ichiro Hayashi, Vinod M. Janardhanan, Hiroaki Watanabe, Koyo Norinaga. Predicting the temperature and reactant concentration profiles of reacting flow in the partial oxidation of hot coke oven gas using detailed chemistry and a one-dimensional flow model. *Chemical Engineering Journal* 2015; 266:82-90.

- **Chengyi Li**, Srinivas Appari, Ryota Tanaka, Kyoko Hanao, Yeonkyung Lee, Shinji Kudo, Jun-ichiro Hayashi, Vinod M Janardhanan, Hiroaki Watanabe, and Koyo Norinaga. A CFD study on the reacting flow of partially combusting hot coke oven gas in a bench-scale reformer. *Fuel*. 2015; 159:590-598.

- **Cheng-Yi Li**, Srinivas Appari, Li-Xin Zhang, An-Ni Huang, Hsiu-Po Kuo, Shinji Kudo, Jun-ichiro Hayashi, Koyo Norinaga. Modeling of gas/particle flow in coal conversion with a drop tube reactor using a lumped kinetic model accounting volatiles−char interaction. *Fuel Processing Technology*. Available online 21 July 2015.

Conference Publication

- **Chengyi Li**, Shinji Kudo, Jun-ichiro Hayashi, Koyo Norinaga. Effect of pressure and gaseous atmosphere on primary pyrolysis of Loy Yang brown coal. *The 10th International Symposium on Novel Carbon Resource Sciences*. (Poster) 2013 年 11 月 2 日 (福岡)

- **Chengyi Li**, Shinji Kudo, Jun-ichiro Hayashi, Koyo Norinaga. A numerical study on coal conversion in a drop tube reactor using CFD coupled with lumped kinetic model. *The 23rd Symposium of Japan Institute of Energy*. (Oral presentation) 2014 年 7 月 19 日 (福岡)

- **Chengyi Li**, Shinji Kudo, Jun-ichiro Hayashi, Koyo Norinaga. Effect of particle size and $H_2O/CO_2/O_2$ partial pressures on gasification rate of nascent char in an atmospheric drop tube reactor. *The 51st Conference of Coal Science*. (Oral presentation) 2014 年 10 月 22 日 (仙台)

- **Chengyi Li**, Srinivas Appari, Shinji Kudo, Jun-ichiro Hayashi, Hiroaki Watanabe, Koyo Norinaga. A CFD simulation on the reacting flow of partially combusting hot coke oven gas in a bench-scale reformer. *The 13th China-Japan Symposium on Coal and C1 Chemistry*. (Poster) 2015 年 8 月 31 日 (中国敦煌)